Physics Division is developing an intense ultracold neutron (UCN) source that will make it possible to study the fundamental properties of the neutron with unprecedented sensitivity. To produce the UCN source, fast neutrons from the LANSCE accelerator will be moderated into cold neutrons and made to strike a volume of frozen deuterium at the base of the cylindrical cryostat in our apparatus (right). The frozen deuterium cools and slows the neutrons into UCN, which can then be used for experiments. Currently, we are exploring how the purity and crystal structure of the deuterium affect UCN production and collection efficiency. The image at left shows a sample of frozen deuterium with visible impurities.
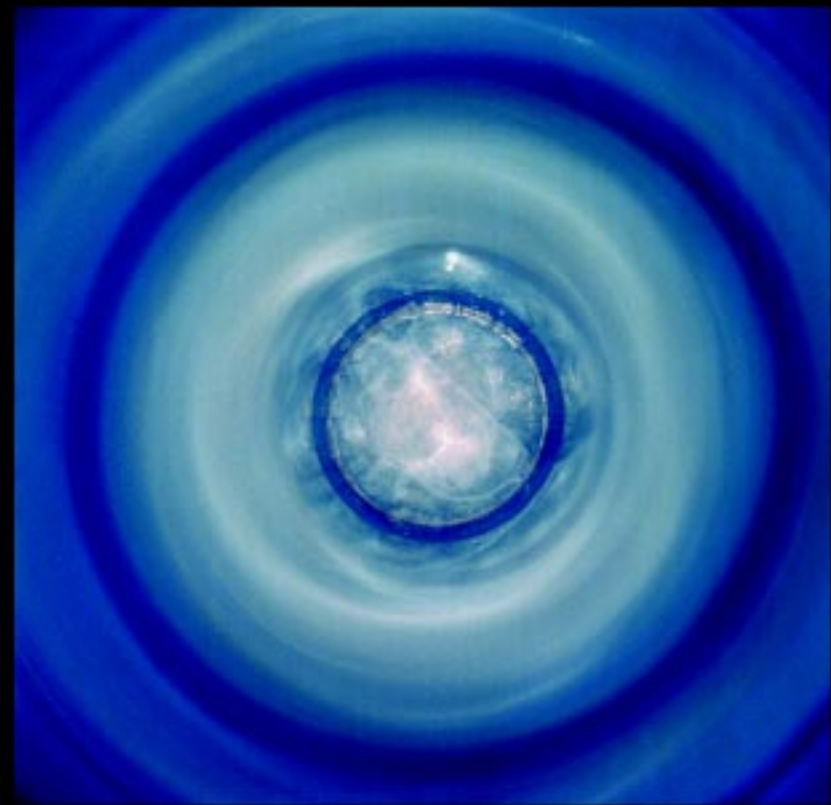
The Birth of Structural Genomics

*J. Berendzen and L. Flaks (P-21);
and J. Newman, M. Park, T. Peat,
G. Waldo, and T. C. Terwilliger
(LS-8)*
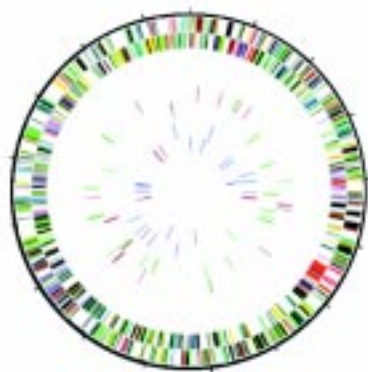
Introduction

Profound scientific discoveries can change not only the direction and scope of research, but also the way people look at their place in the universe. Consider geography in the time of Magellan, or physics in the early 20th century. Researchers in those times must have viewed the data being produced by new instruments with surprise, wonder, confusion, and elation, for they were the first ones to see the world in a new way. At the end of the 20th century, the streams of data from biology and affiliated disciplines are eliciting a similar mixture of emotions. The discoveries being made in these fields may well mark this page of history as the era in which a comprehensive understanding of the machinery of life finally became possible. This new understanding will become the basis for new technologies and industries and will likely change the way we view ourselves.

Modern molecular biology has developed tools for rapidly determining the complete sequence of DNA bases of an organism, known as its genome (Fig. 1). The revolution in biology is being driven by genomics, and at the moment the exemplary technology of the revolution is the automated DNA sequencer. In 1998, sequencing was completed for genomes of six different microbial organisms, typically pathogenic organisms or ones from exotic environments, each a few megabases in length. By the time you read this, it is likely that the aggregate output of genome sequencing projects worldwide will be greater than one megabase per day and that sequencing a microbial genome will be more routine than a space shuttle flight. In a spectacular accomplishment, the first genomic sequence of an animal—a tiny roundworm called *C. elegans*— was completed in December 1998. Four years from now, it is expected that sequencing of the three gigabase human genome will be complete. With the revolution firmly launched in DNA sequencing, it became clear over the last year to many researchers that it is time to move beyond linear DNA sequences to the three-dimensional (3-D) structures and the functions of the proteins that the DNA encodes.

Protein Structures

Our research centers on the determination and analysis of protein structures. The predominant technology for determining these structures is x-ray crystallography, although multidimensional nuclear magnetic resonance spectrocopy of isotopically-labelled proteins is making an increasing contribution in this area. A structure consists of the 3-D coordinates of the atoms in the molecule (typically several thousand). This information can be abstracted as "cartoons" that show the overall arrangement of the

*Fig. 1   A microbial genome in map form.
Each colored bar represents a different
protein.*

backbone of the peptide chain into elements of secondary structure such as alpha helices or beta sheets (Fig. 2). As beautiful and informative as protein structures are, it is important to be humble about their usefulness. Even in a favorable case where one knows the positions of all the atoms in a protein with high precision (a few hundredths of an Ångstrøm), the structure by itself is only the beginning of an understanding of how the protein works. Yet having a structure, even a low-resolution one, provides a basis for understanding data that would otherwise be difficult to interpret. Using such structures, one can perhaps visualize such phenomena as how substrates dock into the active site of an enzyme, which parts of the protein interact with each other or with other proteins, and which parts of the protein are likely to be floppy.

Proteins are linear polymers of amino acids. There are 20 different kinds of amino acids specified in the genetic code, and the DNA sequence (as determined by genomic projects) specifies the sequence of amino acids that will make up the protein. In turn, the sequence of amino acids determines the 3-D structure of the protein, and the 3-D structure determines the function. Genomic projects are delivering the sequences of a few hundred new proteins every day. One can project that four years from now, we will know the sequences of perhaps 100,000 novel proteins. Determination of the 3-D structures of these proteins is painfully slow by comparison, requiring on average about one man-year of effort by a highly trained scientist at a cost of about $200,000. Tens of thousands of newly-sequenced proteins will nonetheless be attractive targets for pharmaceuticals, agriculture, and chemical manufacturing in the near future. Timely access to their 3-D structures is needed.
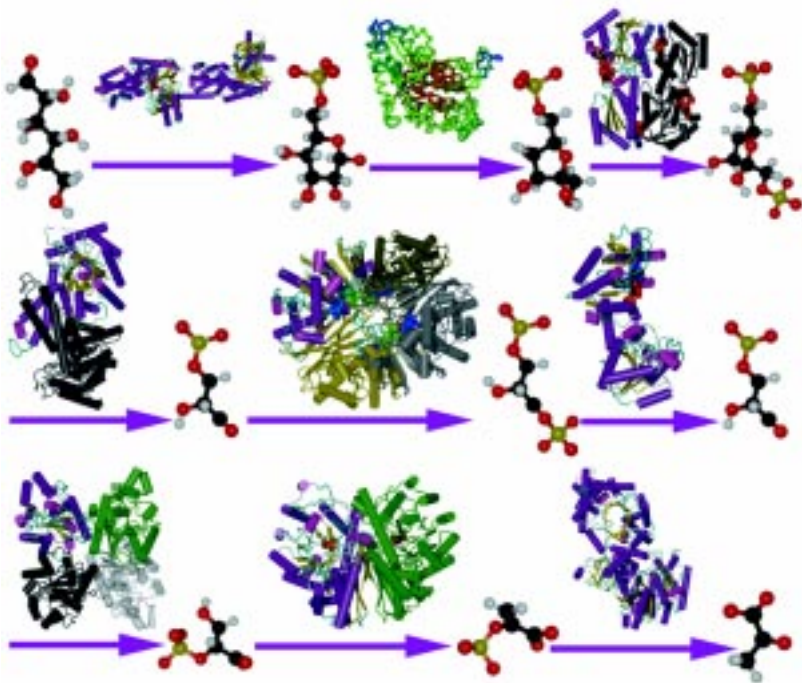
Fig. 2 Structures enable detailed models of the machinery of life. This figure shows the mechanism of central metabolism, which converts a molecule of glucose into two molecules of pyruvate and stores the energy released as ATP. The cartoons between the molecular models represent the enzymes that carry out the reactions.

Thus far, researchers have generally appreciated each protein one by one as each structure has been determined, and our understanding of living systems has been crude and incomplete. Currently, however, for well-studied parts of biological systems (such as central metabolism) it is possible to begin building a global and detailed view. If only every pathway in living systems were so well-characterized, how much we might be able to do! After genomic studies pinpointed a protein of interest for medical, chemical, or agricultural applications, then one could use the structural and functional information to move quickly towards a new drug, synthetic process, or disease-resistant plant. It is impossible to conceive of all the uses for such information. Such questions as how genetic variability among patients will affect drug interactions, which at present can only be answered in an approximate way at great expense, might be addressed quickly and accurately through computer simulation if the database that the simulation draws upon is of high enough quality.

Structural Genomics

For the past few years, our team has been working with other structural biologists, genomicists, theorists, and bioinformaticians to determine how best to meet this challenge. A broad consensus has emerged that the structural biology community should mount a large-scale response through an approach called structural genomics. We are encouraged by advances in DNA-sequencing technology developed as part of large-scale genome sequencing projects, and we estimate that a similar large-scale project in structural biology would drive down the time and cost of determining protein structures by an order of magnitude. We believe we should set as our goal the eventual determination of all of the structures of proteins found in nature to an accuracy that is modest at first and improves with time.

The idea behind structural genomics is not simply that the genomes are now available to play with. Nor is it just that there is great potential for improvements in the technology of structure determination and in economies of scale, although those are crucial. Equally important is the idea that through clustering of DNA sequences and 3-D structures, the problem can be divided in a logical way into pieces that research groups can attack and make progress on individually.

Because protein structures fall into families, a structure of one member of the family gives some idea of the structure of the others. How similar the 3-D structures of two proteins will be can be estimated from the similarity of their DNA sequences. At a DNA sequence identity of 25%, for example, the differences in their 3-D sequences can be expected to be about 1 Å rms (root mean square) and the structures will look very similar overall (at the cartoon level). At this level, one could reasonably launch computer modelling efforts to enable drug design, for example. Thus, the structures of the 100,000 proteins thought to be in the human genome could be represented to 1 Å rms by a database of 25,000

structures chosen to give complete coverage at the 25% DNA identity level. If one is willing to start at a much more modest accuracy of 2.5 Å rms (which is accurate enough to assign overall protein fold but not much more), then the number of structures required falls to about 5,000.

To put a scale on the problem, some 500 protein structures have been determined at this level of difference in 40 years of structural biology. Although there has been near-exponential growth in the rate of determination of protein structures, it is clear that to make a serious impact on this problem even at the "fold" level (2.5 Å rms) there will have to be improvements not only in the rate and cost of doing structures, but also in the coordination among research groups in structural biology, bioinformatics, and genomics. At the same time, the traditional focus of structural biology groups on one particular structure determination at a time for a protein of high functional importance will need to be broadened. Any approach that relies heavily on determining one particular protein structure will be prone to getting stuck because that protein may be quite hard to purify or crystallize, while a closely-related structure may be much simpler to determine. Reducing the emphasis on functional importance should permit much faster determination of the structures of one or more members of a broad class of structures.
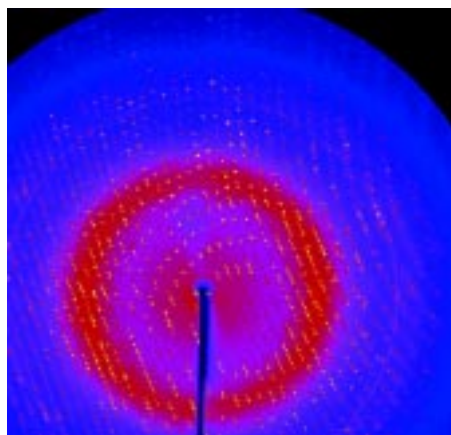
A Pilot Project

In January 1998, we set out to explore what would be feasible in a structural genomics project given the current level of technology. We wanted to determine the fraction of the proteins in a particular genome that could be rapidly determined using existing methods, identify the bottlenecks in the process, and develop new technology to overcome the bottlenecks. We began by selecting a model organism, *Pyrobaculum aerophilum* (PA), which is a microbe found in undersea vents at temperatures near 100°C. PA has a significant advantage for our studies because it is a hyperthermophile and a member of the ancient *Thermoprotoreales* order of the *Archaea* branch of the tree of life. Because the hyperthermophile proteins are stable at elevated temperatures and those from *E. coli* (a workhorse organism engineered to produce proteins) are not, one step of purifying our proteins could be a simple heat treatment (see Fig. 3). Proteins from hyperthermophiles are also thought to be more stable even at moderate temperatures, and they may crystallize more readily than proteins from a mesophile. PA's membership in the *Thermoprotoreales* order was an advantage because some classes of proteins (such as DNA-processing proteins) from organisms in this branch of the tree of life have a surprising similarity to proteins from humans. PA was also a good choice because its genomic sequence was already being determined by Jeffrey Miller and his team at the University of California at Los Angeles (UCLA), who were eager to collaborate with us on this project.
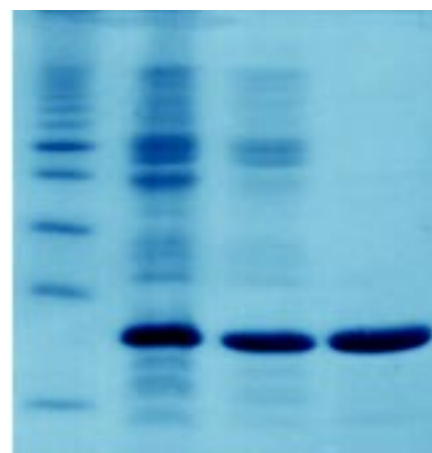
Fig. 3 Purification of a protein as seen by gel chromatography. The "lanes" of this gel go from low molecular weights (bottom) to high molecular weights (top), with a range of about 40 kDaltons. The lanes from left to right are (1) size standards, (2) crude cell extract from the E. coli expression host showing a dark band from high expression of the hyperthermophilic target protein, (3) the same extract after centrifugation, and (4) the same extract after heat treatment at 70°C. Most of the host proteins denature and precipitate after heat treatment, but the hyperthermophilic target protein remains.
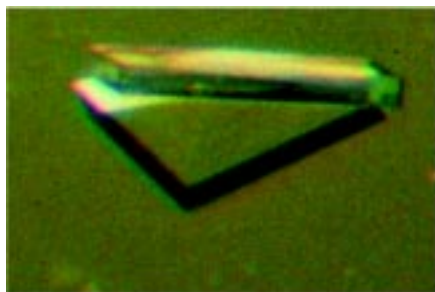
Fig. 4   A protein crystal from Pyrobaculum aerophilum. *Protein crystals are typically 30 to 70% water, but nonetheless can diffract to atomic resolution. A single protein crystal will often provide enough x-ray diffraction data to solve the structure and determine the positions of each of thousands of atoms in the asymmetric unit of the unit cell.*

Our first step in answering the feasibility question posed above was to eliminate from consideration any proteins that could be anticipated, based on sequence, to be very difficult to solve. This includes proteins that are too big (800 amino acids), proteins that are associated with membranes, or proteins that lack sufficient methionine residues to apply the crystallographic technique of multiwavelength anomalous dispersion (MAD) on selenium-substituted methionines to solve the crystallographic phase problem.

Based on these criteria, we eliminated 60% of the roughly 2,200 genes in the PA genome from consideration. Then, from the remaining genes, we randomly selected a group of 40 proteins and determined how many could be easily expressed (grown) in a production organisim (*E. coli*). Of the 70% of the proteins that could be easily expressed, 40% of these could be easily purified by the conventional techniques of heat-treatment and His-tag affinity chromatography. These purified proteins were subjected to a conventional crystallization screening procedure, in which 30% formed well-diffracting crystals.

SOLVEing the Structure at X8-C

Once we had a protein crystal (Fig. 4), we determined the structure through data collection at a synchrotron facility (Fig. 5). We shipped pre-frozen crystals to the X8-C x-ray crystallography beamline at the National Synchrotron Light Source (NSLS) at Brookhaven National Laboratory. The NSLS is a facility run by the Los Alamos National Laboratory Biophysics Group (P-21) in collaboration with the Canadian National Research Council, Hoffman-LaRoche Pharmaceuticals, the Brookhaven Biology Department, and the Department of Energy (DOE)-UCLA Laboratory of Structural Biology. Typical data collection times at X8-C, which runs 24 hours per day for roughly 210 days per year, are are a few hours per data set.

Using the data collected at the NSLS, we solved the protein structure using MAD phasing and SOLVE, a software package we developed to increase the rate of structure determination (Fig. 6). SOLVE automates the solution of the "phase problem" of crystallography using MAD or multiple isomorphous replacement data. SOLVE is an expert system that uses advanced statistical methods to automatically solve in a few hours a problem that formerly took days or weeks of a trained crystallographer's time. SOLVE was recognized as one of the 100 most significant inventions of 1998 by *R&D Magazine*, earning the prestigious R&D100 Award (Fig. 8). Once the complete structure of the protein was determined using SOLVE, we refined the atomic positions to produce a final 3-D model of the protein (Fig. 8). Such models allow us to visualize the overall architecture of the protein, and they are the basis for classifying protein structures into families.

Fig. 5   In a synchrotron x-ray source, electrons are accelerated to energies of several GeV in a polygonal ring with a circumference of about 1 mile. Radiation at the ring's bends (produced by strong magnets) provides an intense x-ray source that is monochromatized and focused on a protein crystal. The crystal is then rotated over 1° in the x-ray beam to produce a diffraction pattern such as this. The intensities of the spots in this pattern are used in calculating an electron density map. Between 60° and 180° of data like this are typically required for a complete data set.

Summary and Outlook

The answer to the question posed by our pilot project is that the cumulative percentage of the proteins in the PA genome that could be rapidly determined using existing methods is roughly 10%. At current productivity levels, we estimate that determining the easiest structures would require one to two man-months of effort per structure.

During the past year, we have played a part in the birth of a new field, structural genomics. As with any infant, it is full of potential but most of the development is still ahead. We anticipate that major national and international projects in structural genomics will be launched by the the DOE, the National Institute of Health, and other agencies, and we expect to form a Joint Proteome Institute with our colleagues at the other national laboratories to coordinate our efforts. New technology will have to be developed if the promise of a comprehensive view of protein structures is to be achieved within the next 15 years. Perhaps most importantly, we will have to make models that reach beyond our immediate findings to more and more distantly related proteins. Filling in the gaps in our knowledge will require experimental, theoretical, and computation efforts that are likely to keep the field in a state of excitement for a long time to come.
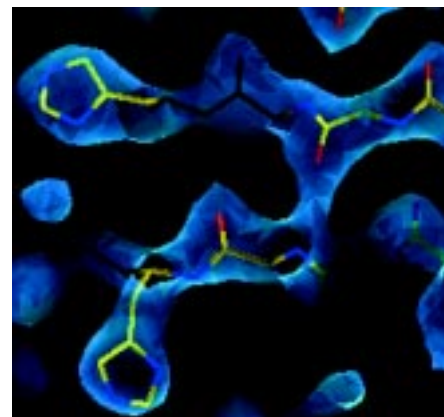
Fig. 6   An electron density contour map (blue) and an atomic model of that density (yellow, blue, and red sticks). The process of solving the phase problem in producing the electron density map has been automated by SOLVE.

Fig. 8   The members of the SOLVE R&D 100 award team, Tom Terwilliger and Joel Berendzen.
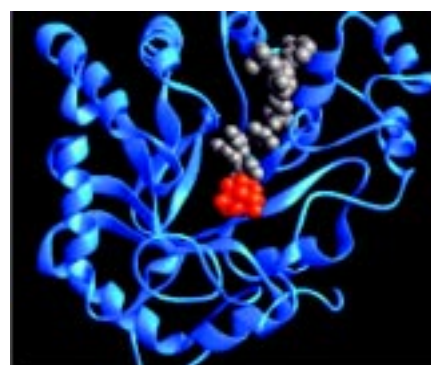
Fig. 9   Cartoon of a protein structure showing alternating helical and sheet regions and a space-filling representation of an enzymatic substrate at the active site. Such cartoons illustrate the overall architecture of the protein and are the basis for classifying protein structures into families.

Bayesian Inference Applied to the Electromagnetic Inverse Problem

D. M. Schmidt, J. S. George, and C. C. Wood (P-21)

Introduction

Under suitable conditions of spatial and temporal synchronization, neuronal currents are accompanied by electric potentials and magnetic fields that are sufficiently large to be recorded noninvasively from the surface of the head. Such recordings are known as electroencephalograms (EEGs) and magnetoencephalograms (MEGs), respectively. In contrast to positron emission tomography (PET) and functional magnetic resonance imaging (fMRI), which measure cerebral vascular changes secondary to changes in neuronal activity, EEG and MEG are direct physical measurements of neuronal currents and are capable of resolving temporal patterns of neural activity in the millisecond range.[1,2,3] However, unlike PET and fMRI, the problem of estimating current distribution in the brain from surface EEG and MEG measurements (the so-called electromagnetic inverse problem) is mathematically ill-posed; that is, it has no unique solution in the most general, unconstrained case.[4,5]

To address this difficulty of EEG and MEG, we have developed a new probabilistic approach to the electromagnetic inverse problem[6] based on Bayesian inference (see, *e.g.*, Bernardo and Smith[7] and Gelman, *et al.*[8]). Unlike other approaches to this problem, including other recent applications of Bayesian methods[9,10], our approach does not result in a single "best" solution. Rather, we estimate a probability distribution of solutions upon which all subsequent inferences are based. This distribution provides a means of identifying and estimating the likelihood of current-source features using surface measurements that explicitly emphasize the multiple solutions that can account for any set of surface EEG/MEG measurements.

In addition to emphasizing the inherent probabilistic character of the electromagnetic inverse problem, Bayesian methods provide a formal, quantitative means of incorporating additional relevant information, independent of the EEG/MEG measurements themselves, into the resulting probability distribution of inverse solutions. Such information can include constraints derived from anatomy on the likely location and orientation of current[9,11,12,13], maximum current strength, spatial and temporal smoothness of current, *etc.*

Bayesian Inference

Bayesian inference (BI) is a general procedure for constructing a posterior probability distribution for quantities of interest from the measurements, given prior probability distributions for all of the uncertain parameters—both those that relate the quantities of interest to the measurements and the quantities of interest themselves. The method is conceptually simple, using basic laws of probability. This makes its application even to complicated problems relatively straightforward. The posterior probability distribution is often too complicated to be calculated analytically, but can usually be adequately sampled using modern computer

techniques, even in problems with many parameters. More detailed discussions of Bayesian inference can be found elsewhere (*e.g.*, Gelman, *et al.*[8]).

Activity Model

The methods of BI applied to the EEG/MEG inverse problem are demonstrated within the context of a model for the regions of activation. This model is intended to be applicable in evoked-response experiments. There is both theoretical and experimental evidence that EEG and MEG recorded outside the head arise primarily from neocortex, in particular from apical dendrites of pyramidal cells (see, for example, Hämäläinen, *et al.*[1]; Allison, *et al.*[14]; and Dale and Sereno[15]). We therefore construct a model that assumes a variable number of variable-size cortical regions of stimulus-correlated activity in which current may be present. Specifically, an active region is assumed to consist of those locations which are identified as being part of cortex and are located within a sphere of some radius, r, centered on some location, w, also in cortex. There can be any number, n, of these active regions up to some maximum, n_{max}, and the radius can have any value up to some maximum, r_{max}. The goal is to determine the posterior probability values for the set of activity parameters, $\alpha = \{n,w,r\}$, which govern the number, location, and extent of active regions.
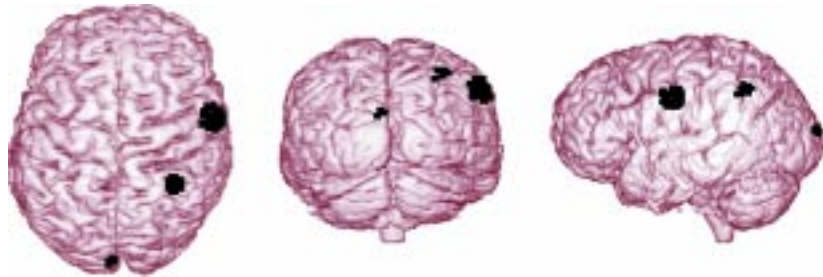
Examples

While the methods described apply to models for both EEG and MEG data, the remainder of this research highlight will use MEG data to illustrate the properties of the approach. Both simulated and empirical MEG data for a Neuromag-122 whole-head system were used.[16] The physical setup of the actual MEG experiment was used to determine the location of the subject's head relative to the sensors in the simulated data examples. In addition, an anatomical MRI data set acquired from the subject in the MEG experiment was used to determine the location of cortex (actually gray matter) using MRIVIEW (see Fig. 1), a software tool developed in our laboratory.[17] About 50,000 voxels were tagged, and the normal directions for each of these voxels was then determined by examining the curvature of the local tagged region.

Fig. 1 Gray matter regions are tagged (in red) from anatomical MRI data. These tagged voxels constitute the anatomical model used to implement the cortical location and orientation prior information.
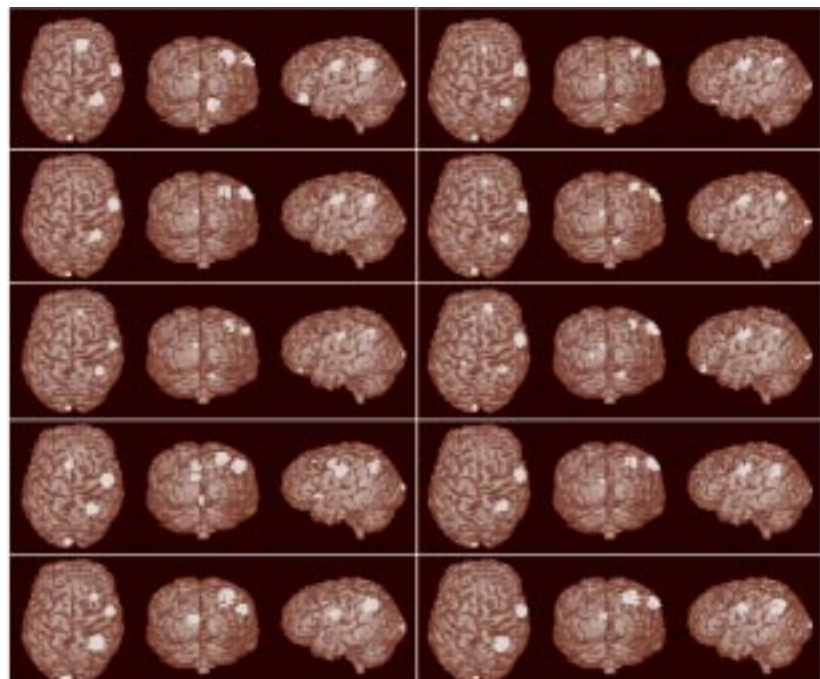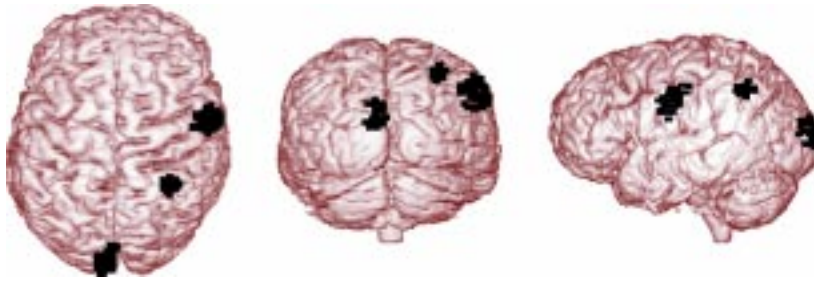
In the first example, a simulated data set was generated using the three active regions of different sizes shown in Fig. 2. Normally distributed noise was added to the simulated data at a level typical of empirical experiments. Our Bayesian inference analysis was applied to this data, and ten thousand samples of the posterior probability were generated. A few of these samples are shown in

Fig. 2   Maximum intensity projections of the location and extent of the active regions used to generate the simulated MEG data from the first example.

Fig. 3. All of the samples shown in Fig. 3 are among the 95% most probable and therefore fit both the data and the prior expectations quite well. Any of these could have produced the given simulated MEG data, yet there are clearly vast differences among the samples. The number of active regions ranges from 3 to 6, the sizes of the regions vary greatly, and the locations of the active regions vary across nearly the entire tagged region of the brain (when considering all samples). This variability is a representation of the degree of the ambiguity of the inverse problem for these MEG data, even with the prior information present.

Despite the degree of variability among the samples in Fig. 3, features common to all are apparent; namely active regions within the three general areas used to generate the simulated data (see Fig. 2). Features such as these, common to all or most of the samples, are associated with a high degree of probability. This

Fig. 3   A few of the samples drawn from the posterior probability distribution for the simulated data in the first example. Each panel shows three views of the maximum intensity projection of all of the active regions from a single sample. Any of these samples could have produced the given MEG data set.

probability can be quantified because the samples are distributed according to the posterior probability distribution. The smallest sets of voxels that contained the center of the active regions in these three areas across 95% of the samples were identified and are shown in Fig. 4. While these regions are consistent with the locations of the active regions used to generate the simulated data, what is more important is that these regions are consistent with at least 95% of the likely sets of active regions that could also have been generated with this data. This is true even when allowing a variable number of active regions of variable extent. This is a very important feature of BI which is necessarily missing from any other analysis method that only considers one possible result, even if it happens to be the most likely result within a given model.

To learn about the extent and size of each of the active regions localized in Fig. 4, we generated a histogram of the radius of the active regions in each of the areas shown in Fig. 4 across the samples (see Fig. 5). This represents the posterior probability for the size of active regions, assuming there was an active region in each of these areas. The radii of the actual regions used to generate the data were 8, 5, and 3 mm in anterior to posterior order. The agreement between actual radii and posterior probabilities is especially remarkable given the variation in the current strengths of the regions used to generate the data. Such information on extent can be very useful, is not present in most other current methods for analyzing MEG data, and is affirmation of the likely utility of anatomical and physiological prior information.

In our second example, we compared Bayesian analyses of MEG responses to visual stimuli in the left and right visual fields to examine the sensitivity of the Bayesian approach in detecting known features of human visual cortex organization.[18] Based on the crossed anatomical projections of the visual fields to the brain and on previous lesion, MEG, and fMRI studies in humans (see, for example, Horton and Hoyt[19]; Sereno, *et al.*[20]; and Aine, *et al.*[21]), initial cortical activation for stimuli in the left and right visual fields should occur near the calcarine fissure in the occipital region of the contralateral hemispheres.

Fig. 5 The posterior probability distributions for the size of the three active regions whose centers are shown in Fig. 4 in anterior to posterior order. The true sizes of the regions used to generate the simulated data were 8 mm (a), 5 mm (b), and 3 mm (c).


(a)

(b)

(c)
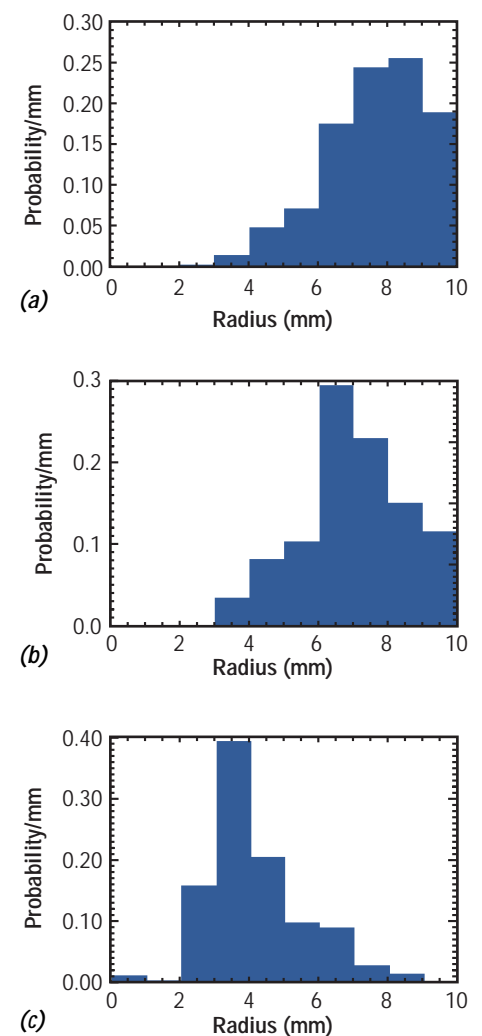
Our Bayesian inference analysis was applied separately to the data for each visual field stimulus at 110-ms post-stimulus latency, a latency that should include robust activation of the calcarine region.[21] Regions that contained activity at a probability of 95% were identified and are shown in Fig. 6. This figure depicts relative probability of activation within these regions on a color scale in three orthogonal slices through the calcarine region and a three-dimensional (3-D) rendering of the occipital region. For the left visual field stimulus, maximal probability of activation at 110 ms was located in the right (contralateral) hemisphere, centered on the calcarine region. This pattern was reversed for the right visual field stimulus at 110 ms, consistent with the predictions from anatomy and from the lesion, fMRI, and previous MEG studies cited above.

Two additional features of the results in this second example should be noted. First, although maximal probability of activation at 110-ms latency was indeed located in the opposite hemisphere, there exists sizable probability for activity in the ipsilateral hemisphere near the mid-line. The extent of the 95% probability regions shown in Fig. 6 is indicative of both the extent of estimated activation and the degree of error or uncertainty in that estimate, even allowing for the possibility of different numbers of active regions of variable extent. Second, although not shown in detail here, analyses at other latencies suggest a progressively increasing number of probable regions of activation in both the ipsilateral and contralateral hemispheres over the latency region from 110 to 160 ms following stimulus onset. It will be of considerable interest to explore the time dependence of the Bayesian inference analyses in relation to evidence for multiple, functionally organized areas of striate and extra-striate visual cortex and to examine the value of temporal prior information (not included in the current activation model) in the form of, for example, temporal covariance constraints.

Fig. 6   Four views of a region found to contain activity at a 95% probability level in the second example for both left and right visual field stimuli at 110-ms latency. The two-dimensional views show the regions within the anatomical MRI data using a temperature-like color scale (bright yellow represents the highest probability). The 3-D views show the locations of the regions relative to other brain structures. These results indicate that the highest probability of activity is in the calcarine region of the hemisphere contralateral to the visual field stimulated.
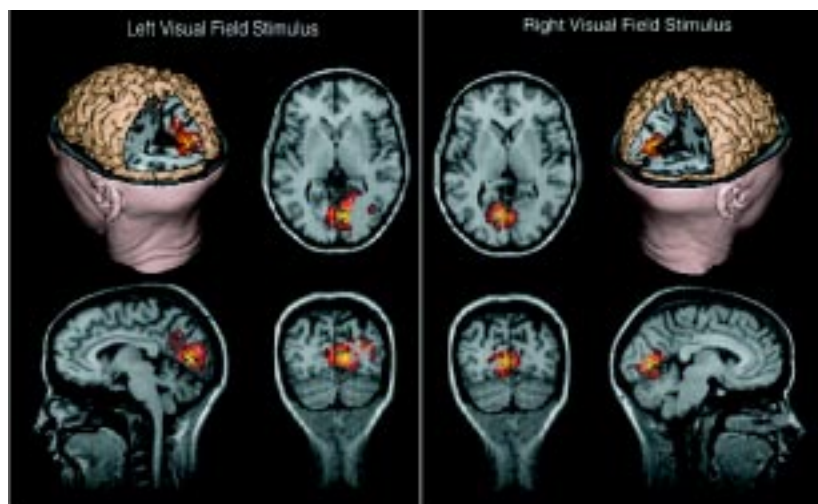
In addition, the Bayesian approach provides a natural means for incorporating information from other functional imaging modalities such as PET or fMRI.[12,13,22] The latter can be readily achieved with the Bayesian framework and with this activity model by assigning prior probabilities to possible locations of active regions based on results from the other modality or modalities. Such a Bayesian formulation of multimodality integration would yield an inherently probabilistic result in which the quantity estimated would be the probability of activation as a function of both space and time.

References

[1] M. Hämäläinen, R. Hari, R. J. Ilmoniemi, J. Knuutila, and O. V. Lounasmaa, "Magnetoencephalography—Theory, Instrumentation, and Applications to Noninvasive Studies of the Working Human Brain," *Review of Modern Physics* 65, 413 (1993).

[2] C. J. Aine, "A Conceptual Overview and Critique of Functional Neuroimaging Techniques in Humans: MRI/fMRI and PET," *Critical Reviews in Neurobiology* **9**, 229 (1995).

[3] A. W. Toga and J. C. Mazziotta, *Brain Mapping: The Methods* (Academic Press, New York, 1996).

[4] H. von Helmholtz, "Ueber einige gesetze der vertheilung elektrischer strome in korperlichen leitern, mit anwendung auf die thierisch-elektrischen versuche," *Annalen der Physik und Chemie* 89, 211 and 353 (1853).

[5] P. Nunez, *Electrical Fields of the Brain: Neurophysics of the EEG* (Oxford University Press, Oxford, 1981).

[6] D. M. Schmidt, J. S. George, and C. C. Wood, "Bayesian Inference Applied to the Electromagnetic Inverse Problem," Los Alamos National Laboratory report LA-UR-97-4813 (1997). To be published in *Human Brain Mapping*.

[7] J. M. Bernardo and A. F. M. Smith, *Bayesian Theory* (Wiley, New York, 1994).

[8] A. Gelman, J. B. Carlin, H. S. Stern, and D. B. Rubin, *Bayesian Data Analysis* (Chapman & Hall, London, 1995).

[9] S. Baillet and L. Garnero, "A Bayesian Approach to Introducing Anatomo-Functional Priors in the EEG/MEG Inverse Problem," *IEEE Transactions on Biomedical Engineering* 44, 374 (1997).

[10] J. W. Phillips, R. M. Leahy, and J. C. Mosher, "MEG-Based Imaging of Focal Neuronal Current Sources," *IEEE Transactions on Medical Imaging* 16, 338 (1997).

[11] J. Z. Wang, S. J. Williamson, and L. Kaufman, "Magnetic Source Images Determined by a Lead-Field Analysis: the Unique Minimum-Norm," *IEEE Transactions on Biomedical Engineering* 39, 665 (1992).

[12] J. S. George, C. J. Aine, J. C. Mosher, D. M. Schmidt, D. M. Ranken, H. A. Schlitt, C. C. Wood, J. D. Lewine, J. A. Sanders, and J. W. Belliveau, "Mapping Function in the Human Brain with MEG, Anatomical MRI, and Functional MRI," *Journal of Clinical Neurophysics* 12, 406 (1995).

[13] A. M. Dale, "Strategies and Limitations in Integrating Brain Imaging and Electromagnetic Recording" *Society for Neuroscience Abstracts* 23, 1 (1997).

[14] T. Allison, C. C. Wood, and G. McCarthy, "The Central Nervous System," in *Psychophysiology: Systems, Processes and Applications: A Handbook*, E. Donchin, S. Porges, and M. Coles, Eds. (Guilford Press, New York, 1986), pp. 5–25.

[15] A. M. Dale and M. I. Sereno, "Improved Localization of Cortical Activity by Combining EEG and MEG with MRI Cortical Surface Reconstruction: a Linear Approach," *Journal of Cognitive Neuroscience* 5, 162 (1993).

[16] A. I. Ahonen, M. S. Hämäläinen, M. J. Kajola, J. E. T. Knuutila, P. P. Laine, O. V. Lounasmaa, L. T. Parkkonen, J. T. Simola, and C. D. Tesche, "122-Channel SQUID Instrument for Investigating the Magnetic Signals from the Human Brain," *Physica Scripta* T49A, 198 (1993).

[17] D. M. Ranken and J. S. George, "MRIVIEW: An Interactive Computational Tool for Investigation of Brain Structure and Function," in *Visualization '93* (IEEE Computer Society, 1993), pp. 324–331.

[18] C. Aine, H. W. Chen, D. Ranken, J. Mosher, E. Best, J. George, J. Lewine, and K. Paulson, "An Examination of Chromatic/Achromatic Stimuli Presented to Central/Peripheral Visual Fields: An MEG Study," *Neuroimage* 5, 153 (1997).

[19] J. C. Horton and W. F. Hoyt, "The Representation of the Visual Field in Human Striate Cortex," *Proceedings of the Royal Society of London* 132, 348 (1991).

[20] M. I. Sereno, A. M. Dale, J. B. Reppas, K. K. Kwong, J. W. Belliveau, T. J. Brady, B. R. Rosen, and R. B. H. Tootell, "Borders of Multiple Visual Areas in Human Revealed by Functional Magnetic Resonance Imaging," *Science* 268, 889 (1995).

[21] C. Aine, S. Supek, J. George, D. Ranken, J. Lewine, J. Sanders, E. Best, W. Tiee, E. Flynn, and C. C. Wood, "Retinotopic Organization of Human Visual Cortex: Departures from the Classical Model," *Cerebral Cortex* 6, 354 (1996).

[22] J. Belliveau, "Dynamic Human Brain Mapping using Combined fMRI, EEG and MEG," Symposium on Approaches to Cognitive Neuroscience by Means of Functional Brain Imaging (Caen, France, 1997).

Design and Preliminary Results from a High-Temperature SQUID Microscope for Nondestructive Evaluation

M. A. Espy, L. Atencio,
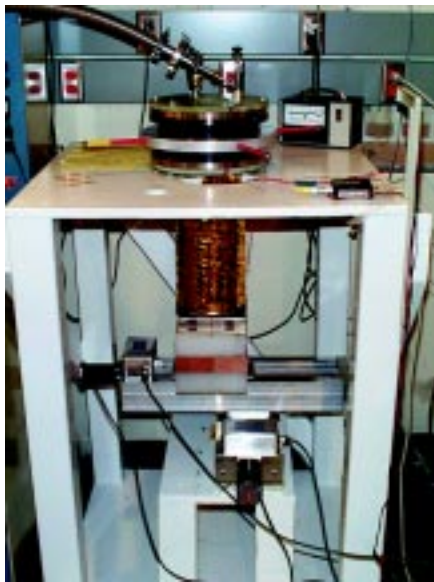*A. Matlashov, and R. H. Kraus, Jr.*
(P-21)

Fig. 1 Photograph of the SQUID microscope dewar operating in our laboratory.

The superconducting quantum interference device (SQUID) is the most sensitive detector of magnetic fields known. SQUIDs are so sensitive that they are able to detect magnetic fields ten billion times smaller than Earth's. Because of their incredible sensitivity, SQUIDs can be used to detect the minute magnetic fields associated with biological function, such as the magnetic fields present outside the head due to neuronal activity in the brain. The primary objective of our work has been developing biological applications for SQUID measurements, such as magnetic mapping of brain function. In addition, we have applied SQUID sensor measurement and analytic approaches to the problem of nondestructive evaluation of stockpile weapons components as part of Los Alamos National Laboratory's Enhanced Surveillance Program, a component of the Department of Energy's (DOE's) science-based stockpile stewardship (SBSS) program.

We have designed a SQUID "microscope" that uses a liquid-nitrogen-cooled SQUID sensor to map magnetic fields induced in a sample (Fig. 1). Similar instruments are described by Black[1]; Kirtley, *et al.*[2]; and Cochran, *et al.*[3]. Our microscope characterizes the features of interest in the sample (*e.g.*, defects due to aging) by detecting anomalies in the induced magnetic field. To address the needs of SBSS, we designed an instrument that is sensitive to small features buried under several intervening layers (~1–20 mm) of conducting and/or nonconducting materials, and that is robust enough to operate even in magnetically noisy, unshielded environments. Our microscope, which has been operational since September 1997, has primarily been applied to specific nondestructive evaluation problems such as detecting and determining the width of buried "seams" inside nuclear components without having to take the components apart. This research highlight describes how the microscope works, and it presents the results of several tests that demonstrate the usefulness of this technology.

Compared with other technologies, SQUIDs are well suited to many problems of buried features such as cracks, pits, or other structural abnormalities. A technique such as complex impedance measurement has to go to lower drive frequencies, ω, to get the required skin depth, δ (the distance that the eddy currents penetrate into the material before falling to ~37% of their magnitude at the surface). As shown in the equations below, the lower the frequency the greater the skin depth (and the more deeply one can probe for a defect). However, lower frequencies also result in a corresponding decrease in signal strength, *V*, as shown:

$$\delta = \sqrt{\frac{2\rho}{\omega\mu_0}} \ \ and \ \ V \propto \omega,$$

where ρ is the resistivity of the material. Ultrasound, on the other hand, has difficulties with signal reflection at the boundaries of material layers that are sonic absorbers (most plastics and electrical insulators), reducing the sensitivity to features below such layers. Finally, radiographic techniques can be expensive, nonportable, and insensitive to small one-dimensional features. SQUIDs are not limited by these shortcomings. SQUID sensitivity does not depend on frequency, enabling these sensors to be used for detecting features and defects over

a broad range of material depths. The induction signal at a given frequency depends only on ρ, not on gaps or intervening layers. Also, a SQUID system can be portable and relatively inexpensive.

Figure 2 is a schematic diagram of the SQUID microscope and the data acquisition system. The main component of the microscope is the dewar, which is shown mounted in a wooden stand in Fig. 1. The inner chamber of the dewar is filled with liquid nitrogen. The high-temperature superconducting SQUID, a bare Conductus "Mr. SQUID"™ chip with an area of 30×30 μm and a sensitivity of 700 nT/Φ_0, is located in vacuum on the tip of a sapphire cold-finger, which is in contact with the liquid nitrogen reservoir. A 1-cm-diameter, 0.25-mm-thin quartz window is mounted on the bottom of the dewar immediately below the SQUID. During operation, the SQUID is located ~0.13 mm from the window. The cold-finger keeps the SQUID at ~78°K despite its proximity to the outside world (~300°K). The small area of the SQUID allows the instrument to operate without shielding in the magnetically noisy environment of our laboratory. Eventually, a second SQUID will be installed at the base of the sapphire cold-finger to construct a first-order gradiometer.[4,5]

The eddy-current induction coils, used to induce a magnetic field in the sample, are located on the outside of the dewar just beneath the window. The induction coils were designed to produce a "null" in the magnetic field at the location of the SQUID, thus using little or no sensor dynamic range for the induction signal. Two designs have been used thus far. The first consisted of two pairs of "double-D" coils rotated by 90°. In this design, the large size of the double-D coils relative to the sample sizes produced asymmetric eddy-currents at the sample edges resulting in large anomalous signals. We were able to avoid most of these edge effects by using the second design, a circle-within-rectangle coil, which is shown in Fig. 2. Two adjustable current generators with 150-mA maximum output current, driven by a common function generator, provide current to the two induction coils. The function generator also provides a reference signal to the lock-in amplifier.

Prior to data acquisition, the sample is centered on the two-axis scanning stage located below the dewar. The distance between the SQUID and the top of the sample is typically 1 mm. The current in the induction coils is adjusted until the SQUID measures a minimum magnetic field. During data acquisition, a personal computer controls the SQUID electronics (Conductus pcSQUID™ electronics) and the motion control system. Low-magnetic-noise stepper motors move the sample, and the SQUID electronics provide the SQUID's response amplitude and phase to the lock-in amplifier. At each point, the personal computer reads the lock-in amplifier, which provides data based on the amplitude and phase of the SQUID responses relative to the reference signal.

Initial data were taken using 150-$\times$ 150-$\times$ 1.5-mm-thick aluminum plates. Blank plates (unperturbed rolled-stock) and flawed plates (with induced cracks and holes) were examined both individually and
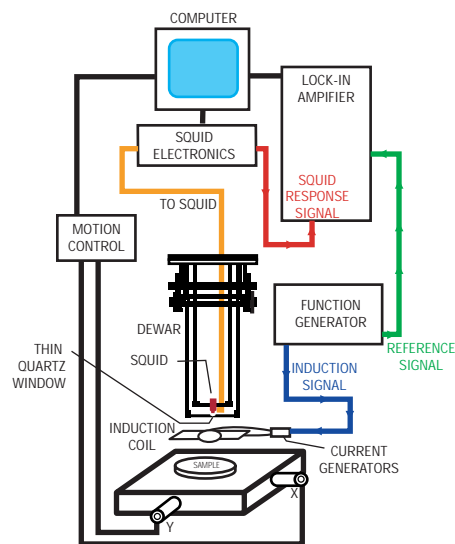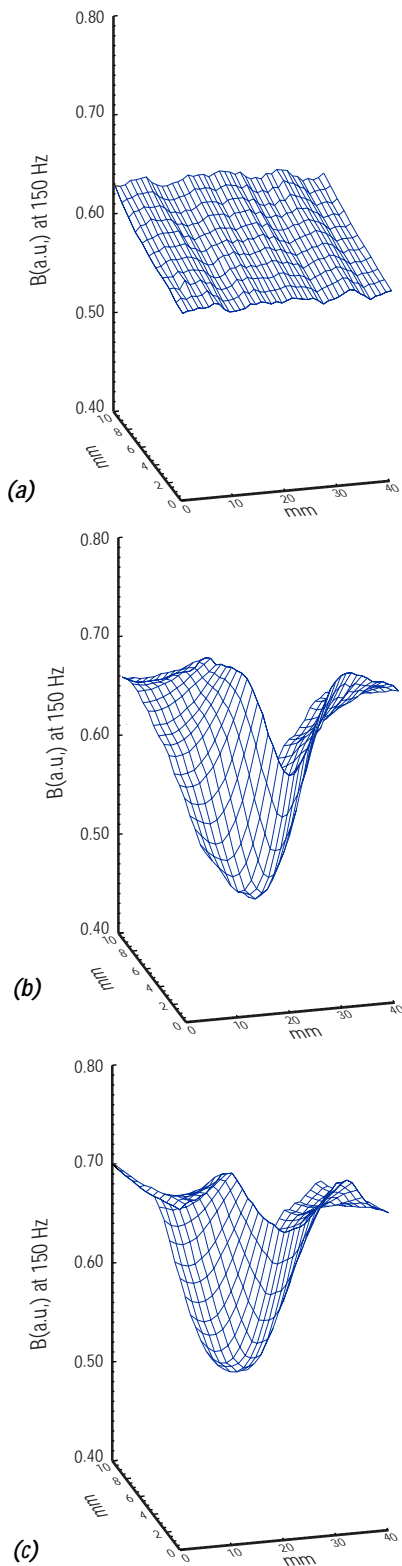

Fig. 2   Schematic drawing of the SQUID microscope and data acquisition system.

(a)

(b)

Fig. 3   Scan of a blank aluminum plate (a), cracked aluminum plate (b), and cracked aluminum plate covered by an unflawed plate (c). Induction frequency was 150 Hz.

stacked. Figure 3 plots the raw amplitude from the lock-in amplifier as a function of position for an unflawed aluminum plate (a), a plate with a crack (b), and a plate with a crack all the way through the 1.5-mm plate material covered by an unflawed plate (c). The presence of the crack is indicated by a valley in which the width of the valley is proportional to the width of the crack. Figure 4 presents raw data for an aluminum plate with holes of various diameters. The presence of a hole is indicated by a two-lobed signal in which the spacing between the lobes is proportional to the diameter of the hole. (The spikes in the data occur where the SQUID electronics momentarily unlocked.) Even 1-mm-diameter holes are visible. Data were also collected for this same plate covered by an unflawed plate (not shown), and all of the holes were still visible (background subtraction was applied to resolve the smallest two holes).

Following these initial data, we analyzed a titanium-tungsten sample that had a stress fracture. A photograph of this sample is shown in Fig. 5a. The results of a single-pass scan lengthwise over the sample are shown in Figure 5b. This sample was slightly ferromagnetic, which poses a challenge to an instrument as sensitive as a SQUID. Simply moving a slightly magnetic object beneath a SQUID can be enough to overwhelm the instrument. However, because of the small SQUID pick-up coil on this device, we were still able to make the scan. This suggests that the instrument should be flexible enough to handle "real-world" objects that might also be slightly magnetized. The stress fracture was clearly observed, demonstrating sensitivity to severe lattice defects that do not necessarily evidence a physical separation. This data set illustrates that while the instrument can localize defects on the submillimeter scale, it is sensitive to defects that are orders of magnitude smaller. It is also interesting to note that the chamfer at the left edge of the sample shown in Fig. 5a is visible in the scan at 633 Hz.

To further test the capabilities of our microscope, we analyzed flaws in fiberglass plates coated with 100 μm of copper. For one of these plates, we carved the initials "P-21" through the copper to expose the fiberglass beneath. This sample is shown in Fig. 6a. Figure 6b shows the raw data from a scan of this plate. The letters are clearly visible.

In another set of these plates (not shown), we carved closely spaced pairs of scratches. The scratches were ~100-μm wide, 75-mm long, and penetrated the 100-μm copper layer. The scratch pairs were separated by different distances. The scratches that were 5 mm apart were resolved. The scratch-pairs that were 3-mm and 1-mm apart each appeared as one scratch, although the 3-mm scratch-pair was wider. These data indicate the need to design induction coils tailored to the specific type of defect being sought. Improved induction coil design and the use of a SQUID array will ultimately provide the highest resolution.

To specifically address the SBSS problem of quantitatively monitoring the evolution of known seams in nuclear components over time, we designed a simple test sample using two 150-×150-×10-mm-thick titanium plates. Titanium was chosen because it has conductivity similar to the specific materials of interest.
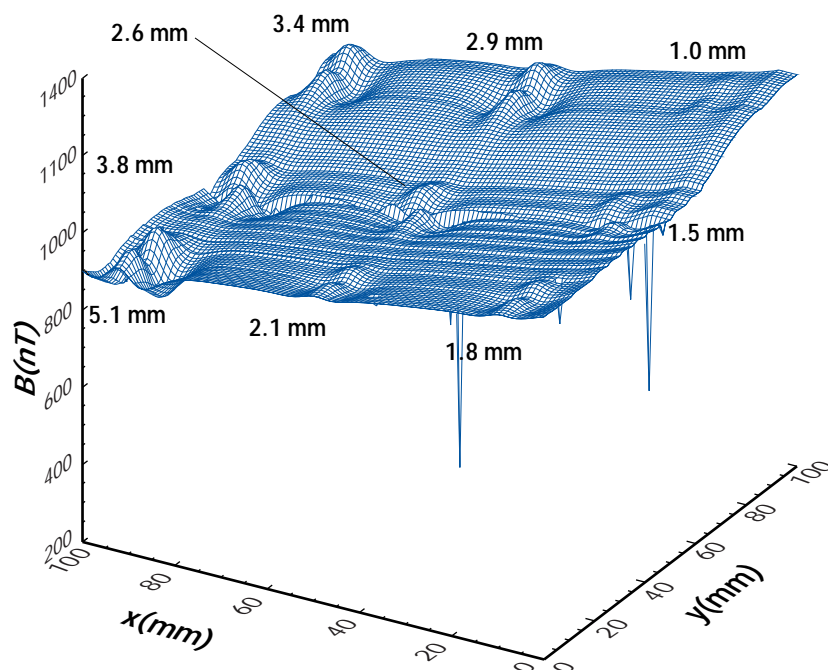
Fig. 4   Raw data for aluminum plate with holes of various diameters. Induction frequency was ~300 Hz.
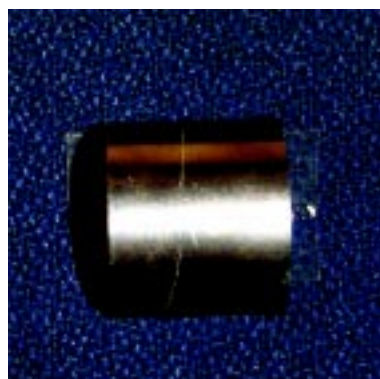
(a)
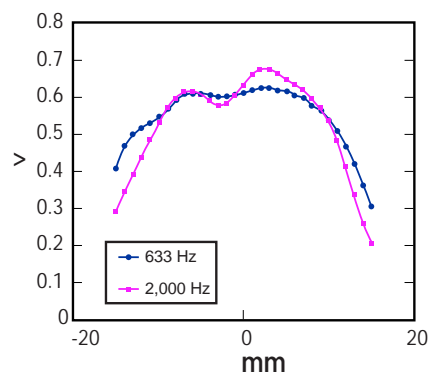
(b)

Fig. 5   (a) Photograph of titanium-tungsten surrogate with a stress fracture. (b) Data from a single scan lengthwise down the surrogate.

(a)

(b)

Fig. 6   (a) Photograph of 150- × 150-mm copper-plated fiberglass plate with "P-21" scratched into the 100-μm-thick copper layer. (b) Raw data from a scan of this plate.

Fig. 7   Data for seams of various widths in a titanium plate at 112 Hz and 266 Hz. The seams were buried under 1 cm of unflawed plate.
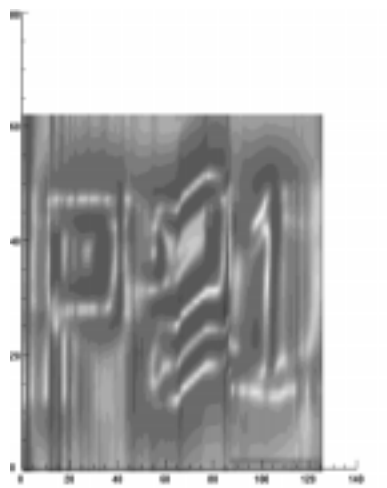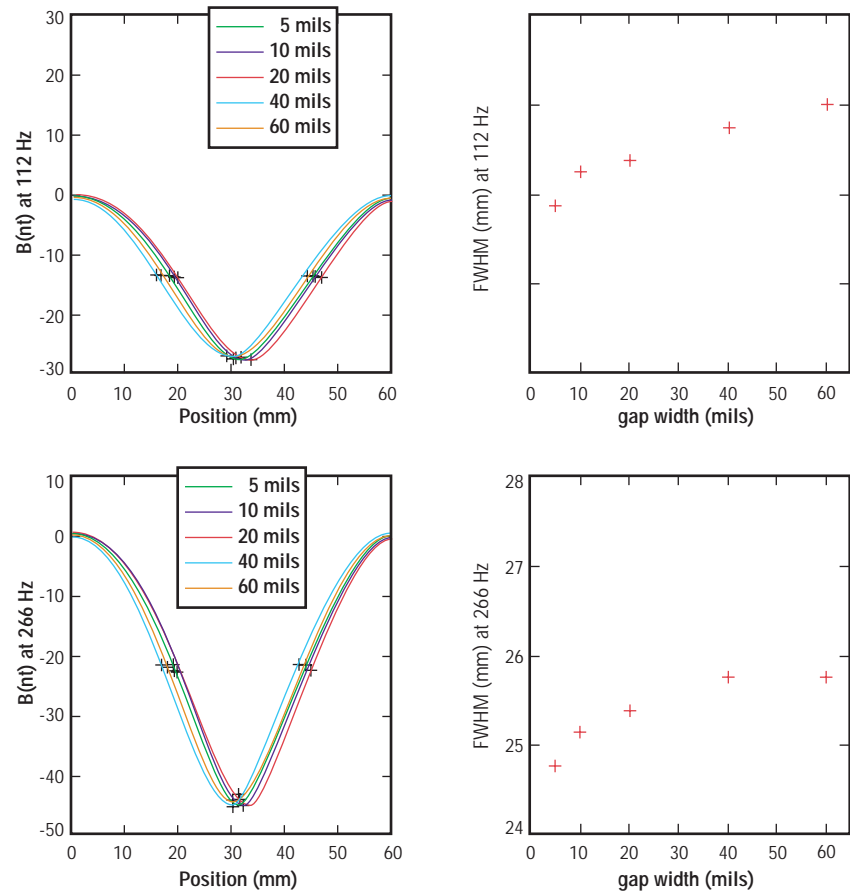

A seam was simulated by cutting one of the plates in half and inserting spacers. In real SBSS cases, seams are typically buried under ~1 cm of conducting material, making it very challenging to determine whether they are changing width as they age. To simulate such a case, the second unflawed titanium plate was stacked on top of the "seamed" plate.

Our goal was to obtain quantitative information about the width of the buried seam. Scans were taken for seam widths of 5, 10, 20, 40, and 60 mils at 112-Hz and 266-Hz induction frequencies. Results are presented in Fig. 7. The response to the seam appears as a valley in the data. The full-width-at-half-minimum (FWHM), or the width of the valley when its height is at half its minimum value, was fit for each scan and is plotted as a function of seam width. As expected, the amplitude of the response grows with frequency. The lower frequency (112 Hz) appears to show the trend of FWHM versus seam width most clearly. This is also somewhat expected; at 112 Hz the skin depth is 2.2 cm (recall that the seam is 1 cm beneath a titanium plate) while the skin depth for 266 Hz is 1.4 cm. Another interesting feature of the data is that at both 112 Hz and 266 Hz the curve of FWHM as a function of seam width appears to be leveling off. One possible explanation is that the response should fall off as the seam width increases beyond the "field of view" of the SQUID.

We have begun modeling the titanium seam width problem using OPERA, a commercial electromagnetic finite-element code developed by Vector Fields, Inc. We anticipate that the results of this modeling effort will enable us to design new induction coils sensitive to specific features of interest at particular depths in a sample. In addition, we have fabricated a series of copper calibration plates with 75-mm-long scratches of depths and widths ranging from 0.125 to 1 mm. We intend to use data taken with these plates in conjunction with the model to further quantify the resolution of the instrument and the competing effects of depth and width of buried seams.

We are also pursuing a number of other improvements to our technique. In collaboration with Oak Ridge National Laboratory, a five-axis motion control system with low magnetic noise is being developed that will enable us to examine spherical and cylindrical samples. In addition, collaborators at Allied Signal/Kansas City Plant are currently developing flux-locked loop electronics with high slew-rate to improve operations in electromagnetically noisy environments. We are also designing a SQUID-array to enhance the resolution of the instrument. While our results are already promising, these improvements will ensure that the SQUID microscope offers useful, accurate results for SBSS and other applications.

References

[1] R. C. Black, "Magnetic Microscopy using a Superconducting Quantum Interference Device," Ph.D. thesis, University of Maryland (1995).

[2] J. R. Kirtley, M. B. Ketchen, C. C. Tsuei, J. Z. Sun, W. J. Gallagher, L. S. Yujahnes, A. Gupta, K. G. Stawiasz, and S. J. Wind, "Design and Applications of a Scanning SQUID Microscope," *IBM Journal of Research and Development* 39, 655 (1995).

[3] A. Cochran, J. Kuznik, C. Carr, L. N. C. Morgan, and G. B. Donaldson, "Experimental Results in Nondestructive Evaluation with High Temperature Superconducting SQUIDs," *Institute of Physics Conference Series* 148, 1511 (1995).

[4] M. A. Espy, R. H. Kraus, Jr., E. R. Flynn, and A. Matlashov, "Two Methods for a First Order Hardware Gradiometer using Two High Temperature Superconducting Quantum Interference Devices," *Review of Scientific Instruments* 69, 123 (1998).

[5] Y. Tavrin, H. J. Krause, W. Wolf, V. Glyantsev, J. Schubert, W. Zander, A. Haller, and H. Bousack, "Eddy-Current Technique with High Temperature Superconducting SQUID Gradiometer for Nondestructive Evaluation of Nonmagnetic Metallic Structures," *Institute of Physics Conference Series* 148, 1519 (1995).

CYRAX™: A Portable Three-Dimensional Laser-Mapping and Imaging System

K. Wilson, C. Smith, and D. Neagley (P-21);
B. Kacyra and J. Dimsdale (Cyra Technologies); and
J. J. Zayhowski (MIT Lincoln Laboratory)

Fig. 1 The Cyrax laser-mapping and imaging system stands about 4-ft tall and can be easily set up and operated by a single user.

Introduction

More than 60 percent of the construction done today is either renovation or expansion work as more owners focus on extending the lives of existing facilities. To plan for expansions and renovations, owners rely heavily on accurate computer aided design (CAD) models of the as-built condition of their facilities. CAD models require considerable investment to ensure that they are updated as the facility is modified. Using conventional methods to create or update models is slow, costly, and often impossible. To meet the need for a quicker, cost-effective way to create accurate three-dimensional (3-D) models, we have developed Cyrax, a portable system for acquiring 3-D data and generating 3-D models of large, complex structures.

Cyrax, shown in Fig. 1, is a completely integrated laser radar and 3-D modeling system that produces a digital model, like that of a digital camera but with added range information that provides the accurate 3-D geometry of the scanned structure. Cyrax eliminates the human error inherent in labor-intensive digitization processes like photogrammetry (in which large numbers of photographs must be taken, scanned, and tiled by hand) by automatically gathering and processing data on the entire structure. Using this stored data, accurate 3-D CAD models of any portion of the scanned structure can be produced at about one-fourth the cost. Cyrax's system provides greater range with a powerful eye-safe laser and greater time resolution. Cyrax is therefore the only technology that can collect accurate 3-D data and create 3-D digital representations and models of large objects such as oil refineries, buildings, mines, and ships.

Development of Cyrax was a joint effort between Cyra Technologies, Los Alamos National Laboratory, and the Massachusetts Institute of Technology (MIT) Lincoln Laboratory. Researchers from the Los Alamos Physics Division developed the time-interval interpolator integrated circuit, a precise time-measuring innovation that makes Cyrax possible. Cyra Technologies was responsible for developing the computer graphics perception (CGP) operating software and CAD software and integrating them with the laser and other mechanical hardware. MIT Lincoln Laboratory developed Cyrax's laser, which generates a 200-ps light pulse that is used with the time-interval interpolator to measure the two-way optical time of flight between Cyrax and an object. The success of this research and development (R&D) collaboration earned Cyrax an R&D 100 Award from *R&D Magazine* as one of the 1998's best innovations (Fig. 2).

Time Interval Interpolator Technology

The time-interval interpolator integrated circuit (Fig. 3) is a technologically significant component in Cyrax. This timing circuit marks the laser firing time and measures the return time of the laser pulse. It is the high speed of the integrated circuit that allows Cyrax to obtain accurate 3-D data at high rates. The time-interval interpolator integrated circuit used in Cyrax is the culmination of

more than eight years of research. The original aim of this research was to meet time-measurement needs of the Los Alamos nuclear weapons program, but the end result is a technology that offers time-measurement solutions for a much wider range of applications.

Before the moratorium on underground nuclear testing, researchers in the nuclear weapons program measured the time history of fast neutron growth rate as an important diagnostic tool during experiments at the Nevada Test Site. The many decades of neutron growth that occur in a very short time during a nuclear event are expressed by the following equations:

$$n(t) = n_0 e^{\int_{t_0}^{t} \alpha(t)dt}$$

and then,

$$\alpha(t) = \frac{n'(t)}{n(t)} = \frac{d}{d(t)}\log_e\left(n[t]\right)$$

where n = number of neutrons, t = time, and α = neutron growth rate.

Historically, the many decades of neutron growth were measured using a series of oscilloscopes that each captured an instantaneous waveform measurement as the experiment progressed. For several decades, this labor-intensive method remained relatively unchanged from Bruno Rossi's first measurements during the Trinity experiment. In the mid-1980s, a better method was conceived that would replace the oscilloscope measurements with measurements of the times at which the growth curve crosses fixed voltages. This method automated the measurement, eliminating the labor costs of the old process.

To make such measurements possible, we developed a high-resolution time interval meter (TIM) (U.S. Patent 5,030,850) based on hybrid circuits and designed for use in high-bandwidth waveform digitizers for the precision monitoring of ultrafast electrical pulses. The waveform recorders built with these circuits proved to be very effective, achieving or exceeding the accuracy of the more labor-intensive method, but they were huge ($10 \times 6 \times 3$ ft), consumed too much power, and generated too much heat. To address these practical problems, we incorporated several technical breakthroughs that allowed us to replace the hybrid-circuit design with a low-cost, low-power, stable integrated-circuit chip without compromising performance. This Los Alamos custom chip, completed in 1994, offers a compact technology that reliably, accurately, and inexpensively makes real-time measurements at picosecond time scales. This chip opened the doors for a wide range of applications, not only for basic research, but also for innovative technologies like Cyrax that depend on that fundamental parameter of all science and technology: time.

Fig. 2 *Physics Division scientists Kerry Wilson, Dan Neagley, and Clayton Smith developed the time-interval interpolator integrated circuit that gives Cyrax its accuracy and speed. Their collaboration with Cyra Technologies and MIT Lincoln Laboratory earned an R&D 100 Award in 1998.*
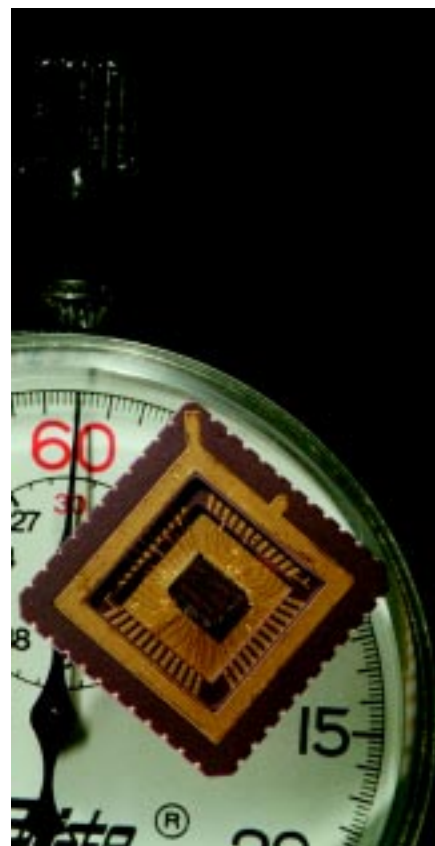
Fig. 3. *The time-interval interpolator integrated circuit, shown with a stopwatch, provides precision timing for Cyrax and other applications. Much as a stopwatch dial divides each minute into 60 second interpolations of the hand's revolution speed, this integrated circuit subdivides a 100-MHz crystal clock's 10-ns cycle into 1,000 subintervals for 10-ps resolution.*

(a)

(b)

(c)

(d)
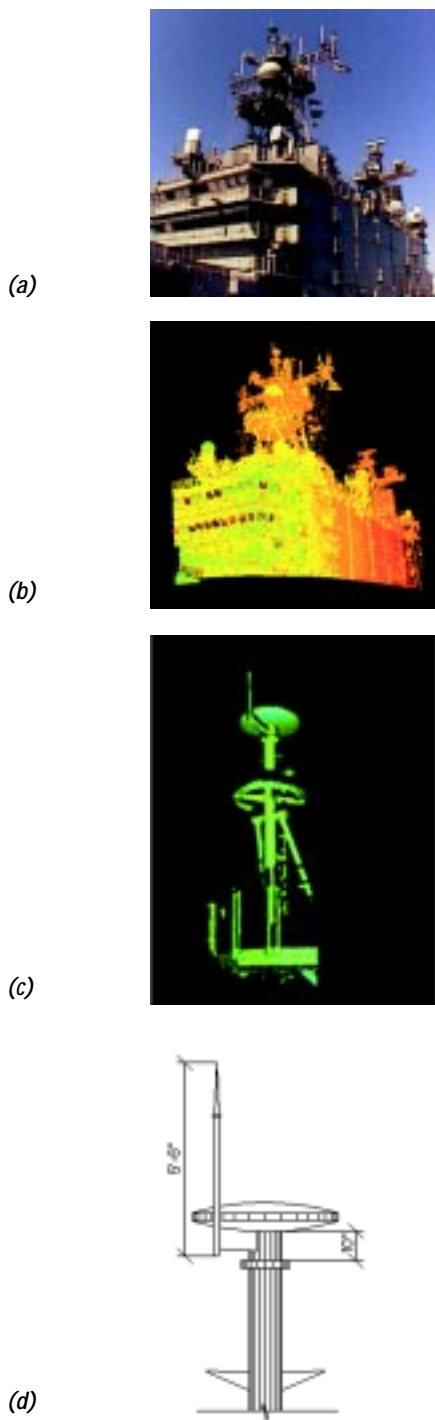
Fig. 4 In a pilot study for the U.S. Navy, Cyrax scanned the U.S.S. Tarawa's island superstructure (a). The associated software instantaneously created a 3-D digital representation (b) that was viewed on a laptop computer as scanning occurred. The data for the ship's mast were then converted into a 3-D surface model (c), which was exported to a CAD application to create an accurate, detailed 2-D drawing (d).

How Cyrax Works

Cyrax contains three primary components. The first is the field digital vision (FDV) machine, which collects the data used to image the structure. The FDV machine comprises a "laser radar" transceiver, an electromechanical scanner, an embedded computer and video camera, and associated electronics, including the time-interval interpolator integrated circuit. The second component is the CGP software application, which runs on a laptop computer to provide FDV control, dynamic visualization, modeling, and interactive 3-D editing. The third component is the software for converting 3-D data to commonly used CAD applications, such as AutoCAD and MicroStation.

Cyrax is simple enough to be operated by one person. The operator sets up the portable, tripod-mounted FDV in front of the object to be scanned. The laser has a 40° field of view and can scan objects from as far away as 100 m without loss of accuracy. The object is displayed by the video display and CGP software on a laptop computer's screen. The operator selects the region of interest and the amount of detail to be scanned by the FDV, and the FDV sends out green, passively Q-switched laser pulses (U.S. Patent 5,394,413) that scan the object as a "cloud of points." This cloud of points is a collection of mathematical points—in x, y, and z space—that represents the actual object's surface in three dimensions. The FDV determines the location of a particular point by measuring the time it takes for a light pulse to travel from the FDV laser to the surface point and back to the FDV light detector. The time interval interpolator integrated circuit measures this time interval to a precision of 10 ps and thus allows locations to be measured to a precision of 2 mm. (This time resolution and accuracy can be characterized from the TIM's own clock frequency and confirmed by the physical dimensions that are measured.) Because of the large volume of 3-D points collected, the green cloud of points appears almost solid.

As the FDV scans the scene, the CGP instantaneously displays the generated 3-D points in another on-screen window. In about an hour, the CGP converts the thousands, or even millions, of data points into representative geometric surfaces, such as the best-fitting planes and cylinders. The software adds "false" color to the representation based on the intensity of light returned by the laser, allowing details as small as 2 to 6 mm to be seen. The CGP can convert the cloud of points into a 3-D surface model that can then be exported, if necessary, to a CAD application to create two-dimensional (2-D) drawings or 3-D models (see Fig. 4).

Unlike traditional surveying and scanning equipment, Cyrax does all the data acquisition and modeling in the field in an integrated (one-step) manner. These features offer clear advantages. Data can be easily spot-checked on-site to eliminate obvious mistakes. As the model is assembled, areas requiring more detail become apparent and more data can be easily acquired. If other views of an object need to be scanned to create its 3-D representation, the operator easily moves Cyrax to another location and repeats the data

acquisition and imaging process. The CGP includes functionality that allows any number of scanning locations to be integrated into a single coordinate system; that is, the different data collections can be "zippered" together to create a single representation of the scanned object.

Applications

Cyrax's primary application is in the architecture, engineering, and construction industry, where it is being used to create as-built CAD drawings of large structures such as buildings, ships, refineries, manufacturing operations, and transportation infrastructure. CAD drawings of these structures are extremely important for new construction and for renovation and expansion work.

In addition, Cyrax can benefit numerous other markets. For example Cyrax has already demonstrated its ability to produce accurate geologic contour maps for industries such as mining. Listed here are just a few other possible applications that show the breadth of this technology.

- *Fine Arts.* Cyrax can document artifacts for preservation and restoration projects.
- *Cinema.* Computer models generated by Cyrax can be used to create realistic special effects. For example, caves measured by Cyrax were used to create background models in the film *Starship Troopers.*
- *Law Enforcement.* Cyrax can generate detailed, accurate archival images of accident and crime scenes.
- *Parts Listing.* Cyrax can recognize shapes in the scanned data and create parts lists for structures as complicated as oil refineries.
- *Facility Management.* Cyrax can provide accurate, detailed structural data throughout a facility's lifetime, allowing facility managers to easily assess the need for and feasibility of redesign as safety standards and facility needs change.

Cyrax has been tested by the U.S. Navy, Fluor Daniel, Raytheon, and Chevron. The results of this testing have produced accurate, detailed images that far exceed other available techniques. Although still a fledgling technology, Cyrax is already changing the way industry looks at 3-D imaging. We anticipate that Cyrax will have profound impacts in many applications, and it will affect our lives over the next few years in ways we can only begin to imagine.
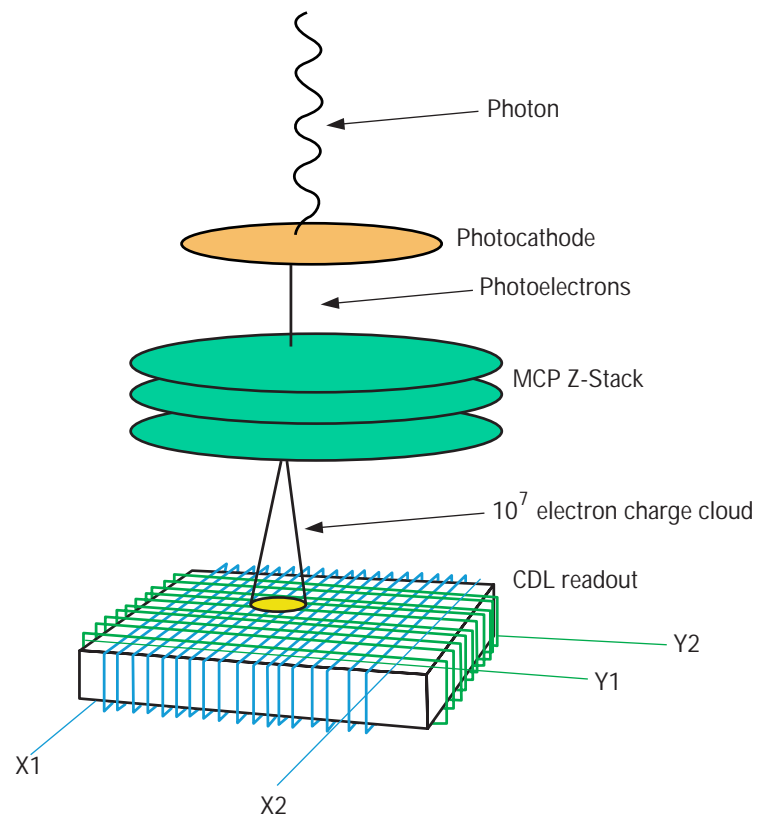
Remote Ultralow-Light Imaging

*R. C. Smith, S. K. Wilson, and
K. Albright (P-21);
R. Scarlett (NIS-6);
C. Ho and A. Bird (NIS-2);
R. Whitaker (NIS-4); and
M. Hindman (NIS-3)*

Much of scientific research depends on the ability to observe objects and phenomena that are invisible to the naked eye because of their small size, high speed, distance, or shielding. Many technologies exist to aid our observations of such objects, and these technologies are constantly advancing to capture more challenging phenomena with greater accuracy and precision.

One area in which the technology has advanced significantly in the last few decades is low-light imaging. Intensified imaging techniques have been in use for many years in applications such as night vision. These techniques allow us to see in the dark, but they provide only two-dimensional views and they do not address the problem of shielded objects. To address these shortfalls, we have developed a remote ultra-low light imaging (RULLI) sensor technology that simultaneously measures the position and absolute time of arrival of individual photons to provide data that are literally three-dimensional (3-D). Our RULLI technique allows us to create 3-D images of objects in low-light conditions—even objects that are moving or, in some cases, shielded from plain sight.

RULLI uses a microchannel plate/crossed delay line (MCP/CDL) detector and pulse absolute timing (PAT) electronics. The MCP/CDL detector is a hermetically sealed vacuum tube that contains a transparent window coated on the inside with visible-light-sensitive photocathode material, a Z-stack of three MCPs, and a CDL readout. Figure 1 shows how the MCP/CDL converts photons into electrical pulses. An active illumination system with known timing characteristics, such as a laser light pulse, is used to illuminate the object, and the returned photons are detected. An incident photon reflects from the object being imaged through the tube window of

Fig. 1   The MCP/CDL detector shown in this diagram converts photons into electrical pulses to record their precise arrival times. Using MDP/CDL technology combined with PAT electronics, our RULLI technique is able to acquire optical data at the single-photon level.

- Photon
- Photocathode
- Photoelectrons
- MCP Z-Stack
- 10^7 electron charge cloud
- CDL readout
- Y2
- Y1
- X1
- X2

the detector, where it strikes the photocathode material. With a finite probability—the quantum efficiency—the photon excites an electron, which leaves the photocathode surface. A bias voltage between the photocathode and the front of the detector's MCP stack attracts the photoelectron towards the first MCP, which consists of many tiny pores. A moderately high voltage, typically above 3,000 V (in vacuum), is applied between the front and the back of the MCP stack. Electrons propagating inside the pores rapidly multiply and avalanche, producing a charge cloud of around 10^7 electrons that is accelerated toward the layered CDLs.

The CDL readout consists of two wires in perpendicular helical windings, one outside of the other. These are supported by a common ceramic structure to fix their position. A ground plane is placed in the middle of the support structure. The charge cloud generated by a single photon event speeds toward and through the windings. Several delay lines interact with the charges, and the signal, after propagation through the windings, becomes a Gaussian-like electrical pulse presented at each of the two ends. With two layers of winding, each having two ends, we have four independent signals: X1, X2, Y1, and Y2.

Measuring the pulses' arrival times, we can reconstruct the position and arrival time of the initial photon event. This is accomplished using the PAT electronics, which is a fast and accurate timing technology that originated in the nuclear test program at Los Alamos. Each PAT board contains the analog and digital electronics to measure the pulse's arrival time relative to a stable clock. One key component of the PAT data acquisition system is a hybrid module known as the Time Interval Meter (TIM) circuit. The TIM measures the time interval between a start and stop signal with a resolution of 10 ps, an accuracy 20 ps for single pulse, and a deadtime of about 80 ns. The TIM uses a built-in constant fraction discriminator (CFD) triggering circuit to ensure that the signal is triggered at a fixed location of the pulse profile, relatively independent of the pulse amplitude. The digital output from the TIM is sent to fast digital electronics to collect, format, and record the data. Through custom algorithms, the position and absolute time of the incident photon event is calculated from the raw data.

To date, we have achieved the following performance in the laboratory: a full-width-half-maximum (FWHM) for a point source of 60 µm, and a timing accuracy for each photon of about 200 ps rms (root mean square) or 420 ps FWHM. We expect the current implementation to offer linear response up to a random count rate of about 10^6 counts per second before significant event degradation due to coincidence. In our literal 3-D imaging field and laboratory experiments (described below), the system had slightly degraded spatial and timing performance from the numbers above. As we continue to improve the system, we expect a point-source FWHM better than 30 µm, an absolute timing FWHM of about 100 ps, and a maximum count rate of 5×10^6 counts/second.
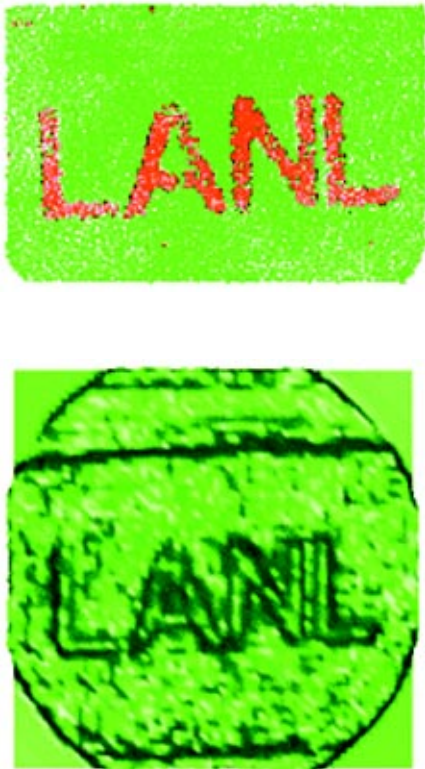
Fig. 2   These images, generated using the data from our laboratory experiment, clearly show that our RULLI technique resolved the 5-cm-high letters. The top image shows the data as a collection of points in 3-D space, with the closest points colored in red. The lower image shows the points as a surface under directed lighting. Our technique allows us to rotate and view these data from any angle.

The combination of MCP/CDL and PAT allows us to acquire optical data at the highest sensitivity possible: the single-photon level. By using the photon counting method to form the RULLI image we have no added readout noise. This means that the imaging limits of the system are dictated by the physics of the scene illumination, not by the detector readout. This level of sensitivity coupled with the timing precision allows the formation of high resolution images on moonless nights, even from moving platforms. Since we measure the CDL pulses at such high precision, we also have a very high resolution optical ranging system that requires the lowest of illumination power. In fact, the system is designed such that the illuminator returns to the detector, on average, one photon per incident pulse.

An end-to-end system with the capabilities needed for this literal 3-D imaging technique has been in operation since mid-1997. Using a commercial pulsed laser in combination with the RULLI technology, several experiments have been conducted under a variety of conditions.

To test RULLI's performance in a laboratory setting, we used a $30 \times 50 \times 5$-cm styrofoam block with 5-cm-thick styrofoam letters glued to the surface to spell out "LANL." The experiment was conducted in a dark laboratory at a distance of 7 m, and a pulsed laser triggered at 1.56 MHz was used for active illumination of the target. The laser was coupled to a 120-μm diameter, 7-m-long multimode optical fiber to achieve a more uniform illumination. The dark count over the entire detector area was about 600 counts per second, and the ambient light through the narrow band filter, including reflected light from two computer screens, contributed another 600 counts per second. The laser return accounted for about 1,200 counts per second. A number of data sets were collected with 240-second (4-minute) exposure times.

Using sophisticated information extraction algorithms, the extracted data were analyzed to separate the returned laser photons from the background photons. Background photons have a random arrival time, whereas the laser return photons have a known time signature that correlates with the laser pulse period. In this experiment, the culled data set contained about 288,000 photons compared to about 2,900 photons contributed from random background, giving a signal to background ratio of about 100:1. The culled data were then processed using a simple topography determination algorithm, and the images shown in Fig. 2 were generated. These images clearly show that we resolved the 5-cm height separation between the LANL letters and the solid styrofoam block.

In another experiment, we applied the RULLI technique to cloud studies. Because clouds are remote, change rapidly, and have structures from small to large scales, the existing tools to study real clouds experimentally have been very limited. We simulated a cloud with different scattering properties by mixing various amounts of fabric softener into a large fish tank filled with water. The 2- $\times$ 3- $\times$ 4-ft tank was observed with the MCP/CDL/PAT

sensor from a distance of 20 ft. A laser beam with sharp pulses at a regular rate of 1.6 MHz was focused close to the center of the field of view. Data were collected using several 60-second exposures.

Preliminary results of this experiment show the behaviors we expect from an optically thick cloud: Following an initial bright point-like spike from the prompt back-scattered photons at the air-tank interface, the photons spread out in spatial dimension and became dimmer. These late photons have undergone multiple scattering in the cloud and return towards the observer after long random walks, which displaces their exit position and angle. Detailed 3-D studies of these behaviors will significantly advance our understanding of clouds and other scattering media.

These experiments demonstrate that the RULLI technique offers a novel tool for imaging complex phenomena that could not be captured using previous techniques. The versatility of this measuring technique—the ability to detect individual photons and accurately measure their positions and arrival times—opens many avenues for gathering data on objects and phenomena that were previously unattainable. RULLI technology will be a solution for many research areas, including the study of small objects in low Earth-orbit, canopy density studies, astronomical imaging, optical brain imaging, and DNA studies. Our work will continue to improve this imaging technique and seek out novel applications. We anticipate that RULLI will reveal exciting phenomena in many areas where observation was previously impossible.

High-Energy-Density Physics at the Pegasus II Pulsed-Power Facility

David Oró (P-22) for the Atlas collaboration: Los Alamos National Laboratory (P Division, X Division, DX Division, MST Division), Lawrence Livermore National Laboratory, the All-Russian Scientific Institute of Experimental Physics (VNIIEF), and Bechtel Nevada
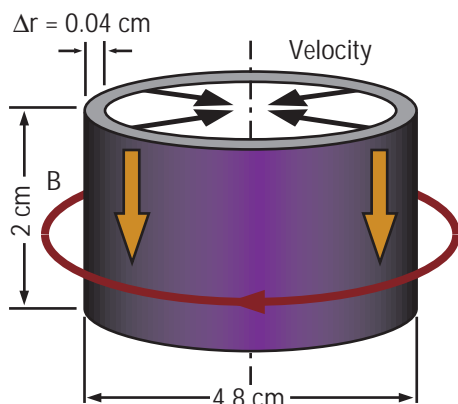
Fig. 1   Diagram of a standardized aluminum liner for Pegasus II. As the Marx bank discharges, electrical current flows in the outer skin of the liner creating a strong magnetic field (B). The interaction of the current and magnetic field produces forces that implode the liner. In some experiments, a target is located inside the liner.

Introduction

The Pegasus II pulsed-power facility is used to conduct a variety of high-energy-density experiments that have applications to the nuclear weapons programs as well as to basic science. Forty-seven experiments were conducted at the facility during calendar years 1997 and 1998. Its unique capability of delivering strong, converging, shock-driven or adiabatically driven compressions in a macroscopic volume, combined with a well-developed suite of permanent and shot-specific diagnostics, have allowed physicists to conduct experiments that are providing important data to the weapons physics community. These data are currently being used to guide the development of particular models of material behavior in high-energy-density regimes and also to validate computer codes used to predict material behavior in these regimes.

The experiments performed at Pegasus II fall under three broad categories: hydrodynamic instabilities, material properties, and basic science and technology. Below, we present an overview of the facility and a discussion of each category with representative examples, and we conclude with a brief overview of the physics agenda for Atlas, the follow-on facility to Pegasus II that is now under construction.

Facility Overview

The Pegasus II facility consists of 144 capacitors arranged in a two-stage Marx bank with a maximum energy-storage capacity of 4.3 MJ. The Marx bank has a maximum erected voltage of 100 kV generating peak electrical currents as high as 12 MA in cylindrical inductive loads.

A typical load, also known as a liner, is shown in Fig. 1. It is made from 1100-series aluminum and is designed such that the inner surface remains solid during the course of the experiment while the liner is heated resistively by the electrical current. Experiments are conducted with or without targets in the interior depending on the nature of the experiment. The dimensions shown in Fig. 1 are for a standardized liner. Pegasus II can deliver ~0.5 MJ of kinetic energy to the 4.8-cm-diameter, 3.2-gram liner. The impact of this liner on an internal target with a diameter of a few centimeters results in shock pressures of 100–500 kbar in the target at liner velocities of ~3 km/s when driven under typical Pegasus II operating conditions. The liner's dimensions and composition are modified to meet the needs of the particular experiment. For example, we can apply a layer of dense material to the liner's inner surface to increase the ram pressure upon impact with a target. For a majority of experiments the liners and targets are constructed at the Los Alamos Target Fabrication Facility operated by the Materials Technology/Coatings and Polymers Group (MST-7).

A panoply of well-developed diagnostics is available for Pegasus experiments. Core diagnostics, those used on every shot, include current probes that measure the current pulse delivered to the liner and flash x-ray radiography with side views of the liner-target assembly. Different shot-specific diagnostics are deployed depending on the nature of the experiment and can include time-resolved pyrometry, particle holography, multiple-frame flash radiography along the liner-target cylindrical axis, laser backlighting, visible imaging of the target, optical pins, and VISAR (an acronym for "velocity interferometer system for any reflector").

Hydrodynamic Instabilities

An important area of research at the Laboratory is the study of the hydrodynamic flow of materials under extreme conditions. Of particular interest are the dynamics of instabilities that can be induced in hydrodynamic flow. Results of experiments are used to guide the development of models that describe the instabilities and to validate various hydrodynamic codes used at the laboratory. A number of experimental series studying hydrodynamic instabilities were carried out using Pegasus II during the last two years. One of these series, RTMIX, involves the study of the Rayleigh-Taylor (RT) instability, a phenomenon observed when acceleration occurs at an interface between two materials of different densities. The goal of these experiments is to diagnose and understand the growth of a mixing layer at an RT unstable interface and to understand the effects of material strength on the development of the mixing layer. Figure 2 shows a cross-section of the load for the first shot in this series, RTMIX 1. The liner consists of a composite cylinder with an outer 800-μm-thick aluminum cylinder in contact with an inner 200-μm-thick copper cylinder having an inner radius of 8 mm. The copper cylinder surrounds uniform, open-cell, polystyrene foam. The glide planes are made from a dense tungsten alloy to inhibit axial motion of the foam during the experiment.
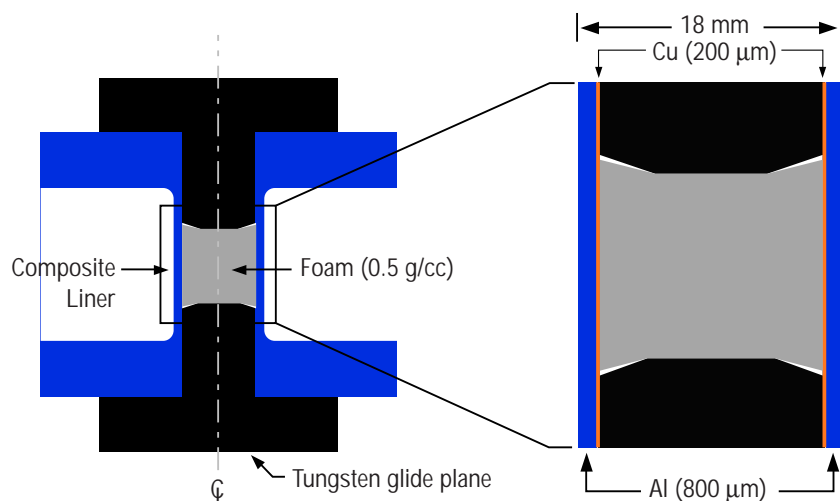
Fig. 2 Side-view cross-section along the midplane of the load for RTMIX 1. During the experiment, the portion of the liner between the tungsten glide planes separates from the rest, imploding against the foam core. The function of the glide planes is to maintain electrical contact and therefore current flow through the liner as it implodes and, for the RTMIX experiment, to inhibit axial motion of the foam as it is compressed.
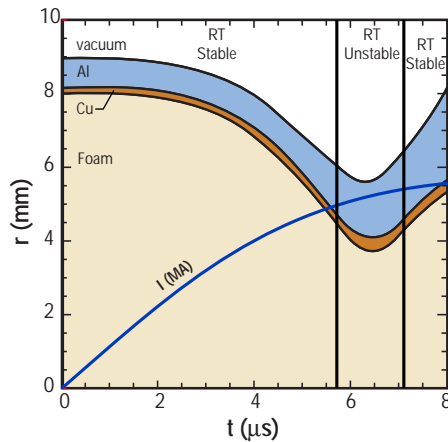
Fig. 3 1-D RAVEN simulation of an RTMIX experiment. The figure shows, as a function of time, the radius of the load interfaces and the current through the load. Also shown are the RT stable and unstable phases of the copper/ foam interface.

Figure 3 shows a simulation of the experiment. The simulation is performed with RAVEN, a one-dimensional (1-D) magnetohydrodynamics (MHD) code. During the initial phase, the liner accelerates inward compressing the foam. As the compression continues, the liner decelerates, stops, and accelerates outwards—in effect, the liner bounces off the foam core. During the period of inward deceleration and outward acceleration the copper/foam interface is RT unstable. Of particular interest is the formation of a mixing layer at the copper/foam boundary as a result of the instability. The liner is designed such that the copper layer remains solid during the experiment and, therefore, it is expected that the copper's strength will play a role in the formation of a mixing layer at the interface through suppression of the instability. Analysis of the original radiographs from the RTMIX 1 experiment shows that the liner does undergo a bounce and an RT unstable phase. However, the data show no discernable evidence of a mixing layer at the copper/foam interface, which is consistent with analyses as well as two-dimensional (2-D) MHD simulations that include strength.

The configuration of the RTMIX 2 experiment was identical to RTMIX 1 with the exception that the inner surface of the copper cylinder had machined sinusoidal perturbations along the length of the cylinder. The perturbations had a wavelength of 1 mm and an amplitude of 50 μm on the upper half and 12.5 μm on the lower half of the cylinder. Analytical results and detailed 2-D MHD simulations predict that the small amplitude perturbation will not grow during the RT unstable phase of the experiment and the large amplitude perturbations will grow. However, the data show no evidence of growth of either amplitude perturbation during the experiment. The results from this experiment will be directly compared with the results from the RTMIX 4 experiment, which was conducted at the end of 1998. (Note that the numbers of the Pegasus experiments follow the order in which the loads for the experimental series are constructed, and not the shot order. The RTMIX 3 load exists, but it has not yet been fielded.) For RTMIX 4, the copper layer was replaced with a low-melting-point indium-tin eutectic alloy with the same perturbations as in RTMIX 2. It was expected that the alloy would melt during the experiment, allowing direct comparison of perturbation growth at an RT unstable interface with and without the effects of material strength. Data from RTMIX 4 are currently under analysis. Details of the RTMIX 1 and 2 experiments can be found in Sheppard, *et al.* [1], and Atchison and Sheppard[2].

Another experimental series performed during the past two years under the general category of hydrodynamic instabilities was a study of the vorticity and mixing generated in a target as a result of a shock-driven Richtmeyer-Meshkov (RM) instability, another hydrodynamic phenomenon associated with an interface between materials of different densities. For these experiments a standard liner was imploded onto a target generating a ~300 kbar shock in

the target. Discontinuous target features seeded RM instabilities that resulted in the formation of jets and vortices. The results of these experiments are currently being employed by the computational design community to benchmark both legacy and Accelerated Strategic Computing Initiative (ASCI) hydrodynamic codes. Details of the comparisons to codes can be found in Guzik, *et al.*[3].

Material Properties

The properties of materials under extreme conditions is an area of active research at the Laboratory. A partial list of topics of interest in this category includes material failure through spall and ejecta, plastic deformations, strain and strain-rate effects, and interfacial friction. A number of experiments were carried out on Pegasus II during 1997–1998 to address various aspects of these topics. One recent series of experiments carried out in collaboration with physicists at Lawrence Livermore National Laboratory concentrated on the spallation of shocked aluminum targets. The goal of these experiments, known as the LLNL series, is to gain understanding of the failure mechanism and its role in the growth of subsequent instabilities and to investigate the role that material strength plays in these phenomena. In these experiments, a standard liner was imploded and collided with a target containing an aluminum cylinder. The collision of the liner with the target drives a shock into the target traveling toward the cylindrical axis. The resulting failure of the aluminum was recorded with multiple-frame flash radiography. Figure 4 shows a cross-section of the general target design for these experiments. The target is an aluminum cylinder with an inner radius of 1.0 cm and an outer radius of 1.3 cm surrounded by 0.2 cm of PMMA (Lucite). The
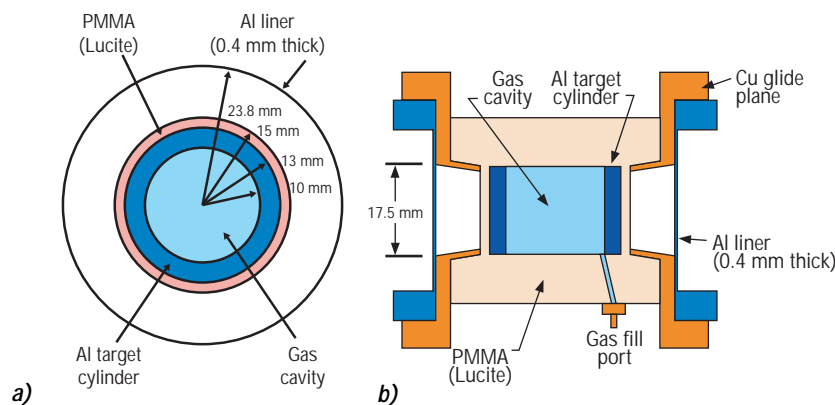
Fig. 4 Top- (a) and side-view (b) cross-sections along the mid-planes of the liner/ target design used for the LLNL series of experiments. During the experiment, current flows through the liner causing the portion between the glide planes to implode and strike the target. For several of the experiments, sinusoidal perturbations, as a function of azimuth, were machined on portions of the interior aluminum surface of the target.
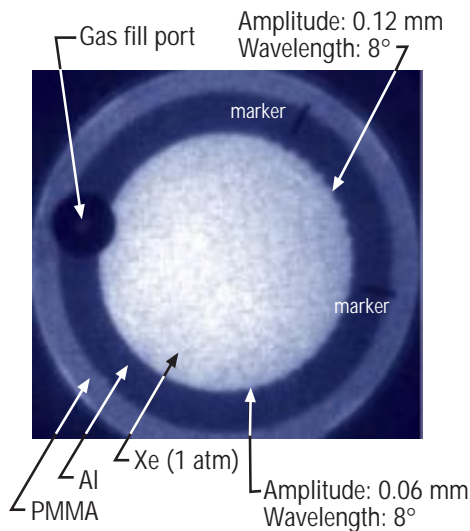
a)
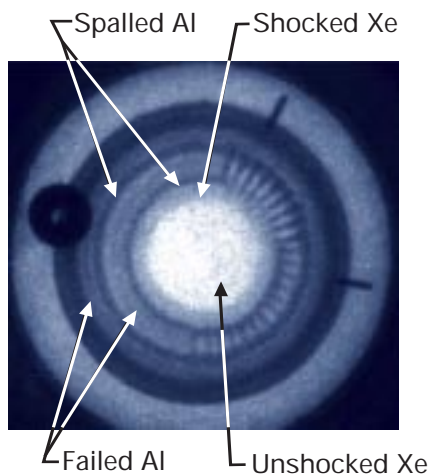
b)

Fig. 5   Axial radiographs of the LLNL-5 experiment (a) before and (b) 3.38 µs after the liner has impacted the target. The impact velocity was 2.2 km/s resulting in a 140-kbar shock in the target. In (b), the shock has exited the aluminum target and is traveling toward the center in the xenon. Visible are the boundary between shocked and unshocked xenon, layers of spalled aluminum, regions of "failed" aluminum, and jets seeded by the perturbations.

central cavity is filled with 1 atmosphere of either xenon or argon. Only a portion of the inner surface of the aluminum cylinder is smooth. Parts of the interior surface have been machined with sinusoidal perturbations, the direction, amplitude, and wavelength of which have been varied with each experiment. The purpose of the perturbations is to act as a seed for instability growth.

Figures 5 and 6 show axial radiographs of the LLNL 5 and LLNL 6 experiments both before and during the implosion. Both targets are constructed from high-yield-strength 6061-T6-series aluminum. For LLNL 5, the liner was driven such that the shock pressure in the target was ~150 kbar, while for LLNL 6 the liner was driven such that the shock pressure in the target was ~500 kbar. Also, there are differences in some of the machined perturbations between both targets, as can be seen from the figures. The data show both layers of spalled aluminum and regions of "failed" aluminum, the exact nature of which is still to be determined. Also shown is the growth of jets that are seeded from the perturbations. The jets form from the "valleys" of the perturbations consistent with results from modeling. Detailed comparisons of these data with data from experiments using low-yield-strength, 1100-series aluminum targets and simulations using the Livermore CALE code, an adaptive Lagrangean-Eulerian hydrodynamic code with a full implementation of the Steinberg-Guinan strength model, are currently underway. More information about these experiments with results from the initial experiments can be found in Chandler, *et al.* [4]

Another experimental series falling under the material properties category is focused on material strength at large strains and strain rates. With Pegasus II, strains greater than 1 and strain rates of up to ~10^6 s^{-1} can be readily achieved in a material sample placed inside of an aluminum liner. In these experiments, a liner constructed of an outer layer of 1100-series aluminum and an inner layer of 6061-T6-series aluminum is imploded. The heating of the 6061-T6 layer from work done against the yield strength is measured with multichannel pyrometry. The temperature data as a function of time are unfolded to give the yield strength as a function of strain and strain rate. These experiments are providing data at conditions where none presently exists, and are being used to test the validity of strength models, some of which are employed in various hydrodynamic codes. Results from the initial experiments can be found in Bartsch, *et al.* [5]

Also under investigation using Pegasus II are frictional effects at shock-loaded material interfaces. For the Dynamic Friction 1 experiment, a liner was impacted on a target constructed with pie-piece-shaped wedges of aluminum and tantalum. The shock travels perpendicular to the aluminum-tantalum interfaces and, as a result of the different material characteristics of aluminum and tantalum, the shock travels faster in the aluminum resulting in a strong sheer between the aluminum and tantalum. The distortion of the materials at the interface is dependent on the frictional force between the materials. The distortion in the aluminum pieces is recorded with flash radiography and the data are being compared to simulations using empirical models of interfacial friction. Also, the tantalum pieces were recovered intact and the interfaces will be subjected to microstructural analysis. Details of the Dynamic Friction 1 experiment can be found in Hammerberg, *et al.*[6]

A series of experiments that continued into the 1997–1998 time frame involves the study of ejecta emitted from a shocked free surface. In these experiments a standard liner is imploded, striking a 400-μm-thick target cylinder. A shock propagates through the target cylinder reaching the inner surface, which causes ejecta to be emitted from the surface. The ejecta are imaged using holography, allowing number *vs.* size distribution to be determined. This work is focusing on understanding how target composition, surface finish, and shock strength affect the production of ejecta. A discussion of this series can be found in Sorenson, *et al.*[7]

a)

b)
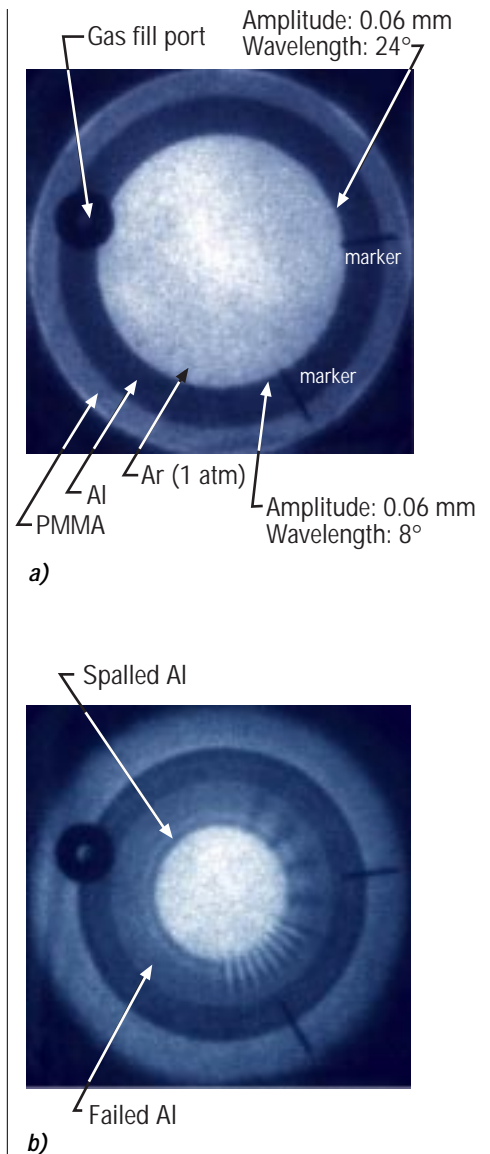
Fig. 6   Axial radiographs of the LLNL-6 experiment (a) before and (b) 2.14 μs after the liner has impacted the target. The impact velocity was 4.5 km/s resulting in a 500-kbar shock in the target. In (b), the shock has exited the aluminum target and is traveling toward the center in the argon. Visible are a layer of spalled aluminum, a region of "failed" aluminum, and jets and density variations seeded by the perturbations. The shock in the argon is not visible in the radiograph due to the reduced x-ray absorption of argon.

Basic Science and Technology

Megagauss 1 was the first in a potential series of experiments intended to use Pegasus II to generate intense magnetic fields in a macroscopic volume lasting for ~1 μs. The technique involves generating a millisecond timescale solenoidal field inside an unimploded liner with a pair of pulsed coils and then having the liner compress the field as it implodes on the microsecond timescale resulting in a magnetic field of multi-Megagauss intensity. It is expected that many electronics properties of materials should be greatly modified in the presence of such strong fields and, therefore, achieving such fields is of keen interest to the condensed matter community.

A number of experiments on Pegasus II over the last two years have been devoted to understanding the limitations of imploding a liner at near-melt conditions. Detailed 2-D MHD simulations show that under strong drive conditions the liner may break up as a result of the magnetic RT instability that occurs on the outer surface of the liner due to the magnetic field pressure pushing on the liner. Experimental data are needed to test the code predictions and have been provided by the Liner Stability (LS) series of experiments. In these experiments, the liners are radiographed during the implosion to determine the extent to which the instability has developed. For some experiments in the series, sinusoidal perturbations are machined on the outer surface of the liner to provide a known initial condition that will result in growth of the magnetic RT instability. The experimentally measured evolution of the instability can then be directly compared with code predictions using the same initial conditions. Results from the LS series can be found in Atchison, *et al.*[8]; Morgan, *et al.*[9]; and Reinovsky, *et al.*[10]

Los Alamos scientists have also collaborated with scientists from the All-Russian Scientific Institute of Experimental Physics (VNIIEF) in Sarov, Russia, in investigating the dynamics of liner implosion physics. Experiments with VNIIEF-designed liners are probing issues related to using materials other than 1100-series aluminum as the primary component in the liner. Details of the Russian experiments can be found in Buyko, *et al.*[11]

A series of experiments related to the Liner Stability and Russian experiments is addressing implosions at the maximum Pegasus II drive current of 12 MA. The motivation for the Megabar series is to develop a liner that can deliver multi-megabar shock pressures when it collides with a target. The liner consists of an 1100-series aluminum cylinder with a platinum layer on the inner surface. The aluminum carries the current and its low density allows the composite liner to achieve high velocity. The high-density platinum impactor layer results in a strong shock delivered to the target. The latest of these experiments, Megabar 3, achieved a liner velocity of ~7 km/s at impact on a 1-cm radius target with minimal bleed-through of the RT instability. This configuration has the capability

of delivering a ~6 Mbar shock to a high-density target. Results of the Megabar 1 experiment can be found in Lee, *et al.*[12]

A number of experiments were carried out on Pegasus II to advance the technology of mechanical joints capable of carrying high current-densities. These experiments were performed in support of Atlas, the follow-on to Pegasus, which will achieve peak currents of 32 MA. Atlas requires the ability to make reliable joints between parts that can carry current densities of up to 51 kA/cm. For this work, several configurations were tested using different materials and geometries, and the results are being used to design the high-current-density connections in Atlas. Results from this work can be found in McCuistian, *et al.*[13]

Atlas: The Next-Generation Pulsed-Power Facility

For many applications in the nuclear weapons program and basic science, the energy of Pegasus II is insufficient to produce the conditions needed to benchmark computational predictions. These requirements have driven the development of the next-generation pulsed power driver, Atlas, now under construction. When complete in late 2000, Atlas will be a 23-MJ capacitor bank, capable of delivering over 30 MA of current to liner targets with a nominal 4-μs rise-time. The machine will consist of 12 pulsed-power modules, each driving a transmission line. All 12 transmission lines connect to a central powerflow channel, which provides a symmetric delivery of current to the target. The target will be contained inside a 2-m-diameter vacuum chamber. At the end of 1998, the final design of the machine was complete with many subsystems tested and many major components on order. When complete, the pulsed power system will be approximately 80 ft in diameter, and it will be supported by a suite of mechanical systems, controls, diagnostics, and data acquisition systems.

Atlas will deliver 2–5 MJ of kinetic energy to nominal 8-cm-diameter, 50-g liners, making possible many new experiments in dynamic materials properties and hydrodynamics. Many candidate experiments have now been identified and are being studied computationally. Among materials properties experiments of interest are absolute equation-of-state measurements along the hugoniot up to 20 Mbar and along the adiabat up to 5–10 Mbar. Both of these experiments will represent significant extensions of present capabilities. We are also designing hydrodynamic experiments with strongly coupled plasmas (plasmas in which the strength of the electrostatic potential of the ions is comparable to or greater than their thermal energy), for which very little prior experimental or theoretical understanding exists. A key feature of these experiments is that the high kinetic energy of Atlas will enable us to create an experimental region large enough that diagnostics can easily resolve hydrodynamic details. Other experiments under development include extension of the high-strain-rate, dynamic friction, and spallation experiments presently

being conducted at Pegasus. Atlas should also provide interesting experimental environments for basic science. For example, generation of magnetic fields up to 2,000 T (20 MG) should be possible. In such fields, the cyclotron radius of a valence electron in a metal is reduced to less than the interatomic spacing, thus involving entirely new mechanisms of electron transport in condensed matter.

References

[1] M. G. Sheppard, *et al.,* "The Rayleigh-Taylor Mix Experiment on Pegasus," *11th IEEE International Pulsed Power Conference, Baltimore, Maryland, 1997,* G. Cooperstein and I. Vitkovitsky, Eds. (IEEE, Piscataway, 1997), p. 1399.

[2] W. L Atchison and M. G. Sheppard, "Studies of Acceleration Driven Instabilities in Convergent Geometries," Nuclear Explosives Code Developers Conference (Las Vegas, Nevada, October 1998), proceedings in press.

[3] J. A. Guzik, K. Koch, and the Antero Team, "Code Validation for the ASCI Antero Project," Nuclear Explosives Code Developers Conference (Las Vegas, Nevada, October 1998), proceedings in press.

[4] E. Chandler, P. Egan, K. Winer, J. Stokes, R. D. Fulton, N. S. P. King, D. V. Morgan, A. W. Obst, and D. W. Oro, "Use of the Pegasus Z-Pinch Machine to Study Inertial Instabilities in Aluminum: A Preliminary Report," 6th International Conference on the Physics of Compressible Turbulent Mixing (Marseilles, France, June 1997), proceedings in press.

[5] R. Bartsch, *et al.,* "Imploding Liner Material Strength Measurements at High-Strain and High Strain Rate," 8th International Conference on Megagauss Magnetic Field Generation and Related Topics (Tallahassee, Florida, October 1998), proceedings in press.

[6] J. E. Hammerberg, G. A. Kyrala, W. E. Anderson, R. D. Fulton, A. W. Obst, H. Oona, D. M. Oro, and M. D. Wilke, "A Pegasus Friction Experiment," Nuclear Explosives Code Developers Conference (Las Vegas, Nevada, October 1998), proceedings in press.

[7] D. S. Sorenson, B. Carpenter, N. S. P. King, D. Morgan, A. W. Obst, D. Platts, P. Rodriguez, J. Roberts, M. Stelts, J. Stokes, T. Taylor, and L. Veeser, "Ejecta Experiments at the Pegasus Pulsed Power Facility," *11th IEEE International Pulsed Power Conference, Baltimore, Maryland, 1997,* G. Cooperstein and I. Vitkovitsky, Eds. (IEEE, Piscataway, 1997), p. 1387.

[8] W. L. Atchison, R. J. Faehl, and R. E. Reinovsky, "Studies of Solid Liner Instability During Magnetic Implosion," Nuclear Explosives Code Developers Conference (Las Vegas, Nevada, October 1998), proceedings in press.

[9] D. V. Morgan, D. Platts, J. S. Shlachter, D. L. Martinex, and B. Carpenter, "Analysis of Radial Radiography for the Liner Stability Series at Pegasus: PGII-59, PGII-62, and PGII-63," *11th IEEE International Pulsed Power Conference, Baltimore, Maryland, 1997,* G. Cooperstein and I. Vitkovitsky, Eds. (IEEE, Piscataway, 1997), p. 1381.

[10] R. E. Reinovsky, *et al.,* "Stability of Magnetically Imploded Liners for High Energy Density Experiments," 8th International Conference on Megagauss Magnetic Field Generation and Related Topics (Tallahassee, Florida, October 1998), proceedings in press.

[11] A. M. Buyko, *et al.,* "Instability Growth in Magnetically Imploded, High Strength, Cylindrical Liners (Results of a Joint VNIIEF/LANL Experiment on the Pegasus-2 Facility)," 8th International Conference on Megagauss Magnetic Field Generation and Related Topics (Tallahassee, Florida, October 1998), proceedings in press.

[12] H. Lee, R. R. Bartsch, R. L. Bowers, W. Anderson, W. L. Atchison, R. E. Chrien, J. Cochrane, H. Oona, D. Platts, M. Rich, W. R. Shanahan, D. W. Scudder, J. Stokes, and L. Veeser, " Megabar Liner Experiments on Pegasus II," *11th IEEE International Pulsed Power Conference, Baltimore, Maryland, 1997,* G. Cooperstein and I. Vitkovitsky, Eds. (IEEE, Piscataway, 1997), p. 366.

[13] B. T. McCuistian, H. Davis, K. Nielsen, and B. Stone, "Atlas Current Tests Performed on Pegasus II," to be presented at the 12th IEEE International Pulsed-Power Conference (Monterey, California, 1999).

Subcritical Plutonium Experiments at the Nevada Test Site

L. R. Veeser, D. A. Clark,
D. B. Holtkamp, P. J. Rodriguez,
and J. K. Studebaker (P-22);
F. H. Cverna, M. Y. P. Hockaday,
N. S. P. King, A. W. Obst, and
D. S. Sorenson (P-23);
J. N. Fritz, R. S. Hixson,
D. L. Shampine, G. G. Schmitt,
and J. E. Vorthman (DX-1);
R. A. Gore (XNH); and
F. Ameduri (NIS-1)
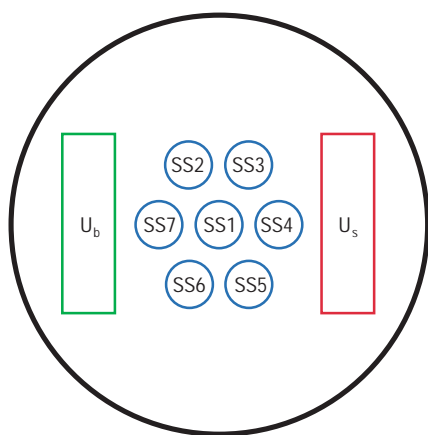
Figure 1. Schematic of the layout for the Rebound 170-GPa experiment. The U_b region contains the diagnostic for measuring flyer plate velocity (see Fig. 2). The U_s region contains the diagnostic for measuring the shock velocities in the plutonium samples (see Fig. 3). The circular regions labeled SS1 through SS7 are the locations of the sound speed samples.

Introduction

In 1997 and 1998, a series of three subcritical plutonium experiments was conducted at the Nevada Test Site (NTS). These experiments, which are the first of their kind to be completed at NTS since the moratorium on underground nuclear testing in 1992, have several purposes. Foremost among these purposes is the study of plutonium physics and the maintenance of our readiness to resume underground nuclear testing should the need arise. These experiments were designed and fielded by the Dynamic Experiments (DX) Division in collaboration with the Physics Division and other Los Alamos divisions, as well as Sandia National Laboratory and Lawrence Livermore National Laboratory. The equation-of-state (EOS) measurement techniques were developed in DX Division, and they have been used by DX Division and its predecessors (GMX and M Divisions) for the past 40 years. Many of the diagnostic and recording techniques, especially for remote data collection, were developed by Physics Division for underground nuclear tests and pulsed power facilities.

The first two experiments, called Rebound and Stagecoach, were executed in July 1997 and March 1998, respectively. Their focus was the plutonium EOS. The third experiment, Cimarron, was conducted in December 1998. Its focus was the ejecta produced when a shock in the plutonium releases into the surrounding vacuum. The data from all three experiments are classified; therefore, this discussion will focus on the experiments themselves and the roles of the Detonation Science and Technology (DX-1), Hydrodynamic and X-Ray Physics (P-22), and Neutron Science and Technology (P-23) groups.

Rebound

The experimental techniques used on Rebound (and Stagecoach), such as the use of explosive-driven flyer plates to shock the samples and flash gaps to identify shock arrivals, were developed at Los Alamos National Laboratory in GMX Division and its successors over the last several decades. Adapting these techniques to the specific plutonium experiments described in this research highlight was done principally by the DX-Division authors listed above, but with significant contributions from the Physics Division. Physics Division personnel came to be involved because of the need to bring the signals out of the enclosed containment room (called the Zero Room because historically it was the room surrounding "ground zero" in underground nuclear testing) to record them at a remote location in the NTS environment. To accomplish this, the direct-view rotating-mirror cameras typically used at the GMX-, M-, and DX-Division firing sites to detect the flashgap signals (described in McQueen, *et al.*[1]) were largely replaced by fiber optics that took the light from the experiment to optical receivers or electronic streak cameras. For Rebound, DX-1, P-22, and P-23 collaborated on a series of seven local experiments to ensure that these diagnostic changes would retain high data quality and to refine the specific geometric parameters of the experiments. These local experiments were very successful.

The goal of Rebound was to study how small plutonium samples, typically a few tens of grams each, respond to shock compression at three specific high-pressure conditions—80 GPa (800 kbar), 170 GPa (1.7 Mbar), and 230 GPa (2.3 Mbar). Three separate experimental assemblies were fielded. Each of the assemblies used a 300-mm-diameter stainless-steel flyer plate that was driven down a barrel by high-explosives (HE) product gases until the plate struck a Lexan target plate holding several samples of gallium-stabilized, delta-phase plutonium. The thickness of the explosives charge, combined with the driver-plate thickness and run distance, determined the driver-plate velocity and consequently the pressures induced in the samples. The aim was to determine the shock Hugoniot (the locus of end points that can be reached in shock wave compression) and sound speed behind the shock front at all three pressures.

The success of the experiment was made possible by close collaboration among DX-1, P-22, P-23, and the other participants. DX-1 used its expertise in shock-wave physics to design experiments most likely to provide results in the EOS regime where the most serious uncertainties lay. Physics Division drew on its experience in underground testing to ensure high-quality data with precision adequate to meet the stringent requirements for such experiments. This is noteworthy because traditionally shock experiments are done under controlled laboratory conditions. In these fundamental subcritical experiments, the research is done underground in a "mining" environment, making it challenging to measure the fiducials, achieve accurate timing, and maintain experimental precision while doing the measurements remotely. Diagnostics included 112 fiber optic pins to measure the velocities and flatness of the flyer plates, shock velocities in the plutonium samples, and sound speeds in shocked plutonium; two electronic streak cameras, each with 35 data channels, which determined any tilt or bowing in the 170-GPa flyer plate and obtained high-time-resolution shock and flyer-speed data; and an energy release measurement to verify that the plutonium was never in a critical-mass configuration and that no self-sustaining fission reaction occurred. Following is a brief outline of the Rebound experiment, explaining what was done and why.

Figure 1 shows the schematic layout of the target plate for the 170-GPa assembly, which had the simplest configuration. The layout for the 800-kbar experiment was similar except two more samples, similar in size and shape to the sound-speed samples and placed near them, were used by DX-Division and Sandia researchers for VISAR (an acronym for "velocity interferometer system for any reflector") measurements of the free surface velocity. The layout for the 2.3-Mbar experiment was also similar except a sample, similar in size and shape to the sound-speed samples and placed near them, was used by Livermore for a release-adiabat measurement. Figure 2 shows a detailed schematic for the diagnostic that measured flyer plate velocity (u_d). The diagnostic consists of fiber-optic pins behind steel of two thicknesses and a flash gap containing argon or xenon that emits light when shocked. Signals travel on fiber optics and are detected by photomultiplier tubes
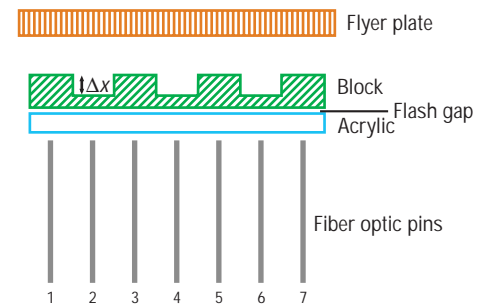

Figure 2. Schematic of the U_b block for measuring flyer plate velocity at the time of impact with the target plate.
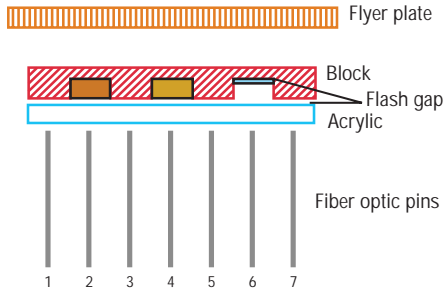
Figure 3. Schematic of the U_s block for measuring the sample shock velocities from the impact of the target plate.

(PMT), avalanche photodiodes (APD), and, when fast recording speed is particularly important, high-speed electronic streak cameras. Flyer plate velocity is determined from the arrival times of signals at two levels. When the flyer plate first strikes the block, a shock forms in the thick regions of the block; when the shock emerges, the flash gap light is detected by the odd-numbered pins. A short time later, the plate strikes the bottom of the notches, where it induces a shock of the same pressure, and that shock is detected by the even-numbered pins. The time difference between the even and odd pins (Δt) is related to notch thickness (Δx), flyer velocity (u_d), and the shock velocity in the block (u_s) by the following equation:

$$\Delta t = \Delta x(1/u_s - 1/u_d)$$

Flyer velocity can be determined by using the known EOS for stainless steel to eliminate u_s. The same principle is used with fiber optics coupled to the streak cameras, except that a closely-packed array of fibers replaces each pin. In this way we can measure detailed local variations in shock arrival times at the flash gap to determine spatial variations in the shock arrival profile, such as might arise from tilt or curvature of the flyer plate.

A detailed schematic for the diagnostic that measured the shock velocity in the plutonium samples is shown in Fig. 3. Two plutonium samples and a piece of transparent Lucite are placed in notches in a stainless steel block. The plutonium shock velocity is determined from the time delay between the start signal when the shock enters the samples, and the stop signals when it leaves the samples. The plutonium start signal is measured through the Lucite and also calculated from stop signals and the shock velocity in the block.

Optical signals proportional to the light intensity were taken from the experiments to the recording stations on fiber optic cables. Long fibers went to either PMT or APD receivers, some in an above-ground station ~1 km away, and some in an underground station about 150 m away. Longer fiber-optic lengths cause increasing distortion of the signals from dispersion, so the data requiring higher time resolution were recorded in the closer station. In the 1-km station, we used 40-nm-wide, 850-nm wavelength filters as a compromise to get adequate light into the receivers while limiting dispersion effects to a few nanoseconds. The fibers were carefully cross-timed in two different ways, one using an optical time domain reflectometer and the other using light from a diode laser injected into many fibers simultaneously. Fibers of similar lengths were timed relative to each other to within 1 ns. This fine control on the cross timing was necessary for the success of the experiment.

Redundant signals from the 170-GPa experiment were also taken a short distance, just a few meters, to a pair of streak cameras located just outside the Zero Room. One camera recorded the flyer speed and one the shock speeds. Before timing, these fibers were cut to lengths such that, as closely as we could determine before the experiment, the signals would all arrive simultaneously at the camera, allowing us to increase the camera sweep speed. We used five times as many fibers as

pins (35 fibers each for U_b and U_s) to image the flashgap region so that we could better determine the shock profile across this region. The imaged spots were spaced along the line of pins so that the shock breakout was determined along the entire length of the flashgap. Although the technique was somewhat developmental, it gave a good measurement of the shock spatial profiles, as well as the shock and flyer speeds. This method also provided us a path for making these measurements on Stagecoach, where they were crucial to our obtaining good data on two of the experiments.

In addition to measuring fundamental quantities, such as shock and particle velocities, in plutonium samples, we also made measurements of a derivative quantity, the sound speed. Sound speed data provide valuable constraints to the EOS when combined with shock Hugoniot data. To measure sound speed, the rarefaction-overtake method described in McQueen, *et al.*[2], and shown in Fig. 4 was used. At the center of the target plate are seven samples of different thicknesses, each backed by a piece of high-density glass that serves as an analyzer material, emitting light when the shock arrives. The flyer plate strikes the samples, driving shocks into them and eventually into the glass. Meanwhile, another shock moves back through the flyer. When it reaches the interface with the driving HE gases, a rarefaction fan is reflected into the flyer, eventually moving into the samples and the glass. The pressure changes gradually in this rarefaction rather than suddenly as in a shock wave, but the rarefaction moves faster than the shock front and eventually overtakes it. The samples are thin enough so that, in most cases, the rarefaction overtake occurs in the glass, where it reduces the pressure and causes the light emitted by the glass to be reduced rapidly. The sound speed (the speed of the leading edge of the rarefaction wave), is determined from Δt, the time from first light in the glass until the light just begins to fade, for each sample thickness. Extrapolation to $\Delta t = 0$ gives the sample thickness for which the overtake would have occurred exactly at the sample-glass interface. The sound speed may be calculated from this thickness and other known quantities.

It is important to have an estimate of the signal levels before the shot so that the recording can be set up appropriately. For the flashgaps, the signals were only a few nanoseconds in duration, and their timing could be determined adequately even if they were slightly saturated. Compressed-gain amplifiers on some of the APDs also helped by increasing the dynamic range of the recording. For the sound speed data, however, any saturation would have caused us to lose the information on when the light began to dim. Compressing the signals would have also obscured the timing of the break. Furthermore, the sound-speed light levels from the lowest-pressure assembly were very low. We were able to obtain good sound-speed data by using redundant receivers and recorders with different gains, and for the low-pressure experiment we replaced the 850-nm APDs with ones based on GaAs photodiodes that operated around 1.3 μm. At these longer wavelengths the signals were large enough to make the experiment a success. Just as crucial were the light levels in the streak
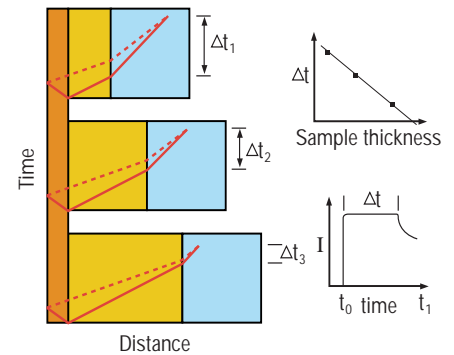
Figure 4. Rarefaction-overtake method for measuring sound speed in samples (yellow) backed by high-density glass (blue) and struck by a flyer plate (orange). The red lines in the sketch show time vs. position for the shock front (solid line) and the fastest rarefaction wave (dashed line). The lower graph illustrates a typical optical signal. The light comes on suddenly when the glass is shocked, remains constant for a time, Δt, until the pressure in the glass is reduced, and then drops gradually as the rarefaction fan overtakes the shock. The upper graph shows Δt for different sample thicknesses.

cameras. All of the levels were estimated from the signals in the seven local experiments.

After corrections for bow and tilt of the flyer plate and other experimental effects, the Rebound experiments produced three points on the shock Hugoniot for the plutonium alloy of interest. Preliminary uncertainties in the u_s-u_p plane were $< \pm 1.5\%$. Sound speeds for the same three pressures were determined with a similar uncertainty. Uncertainties in the release adiabat have not yet been published by Livermore, but they are expected to be slightly larger.

Stagecoach

Stagecoach, the second in this series of experiments, was conducted to improve our understanding of the plutonium EOS, to study the effects of plutonium aging on the EOS, and to develop new diagnostics for future subcritical experiments. The plutonium aging question is complex because plutonium's radioactivity can cause changes in material properties, and we must do experiments to see whether or not it does.

Stagecoach consisted of five experimental assemblies similar to those used in Rebound. Pressures in the plutonium samples ranged from 30 to 320 GPa. All five assemblies had a flyer velocity diagnostic like the one shown in Fig. 2 and a shock speed diagnostic like the one shown in Fig. 3. Each shock assembly included two samples, as shown in Fig. 3, and two of the assemblies included two such shock speed diagnostics. Each assembly had one sample of the plutonium alloy tested on Rebound and one or three aged plutonium samples, providing a test of the response of the aged plutonium at all five pressures. Overtake measurements were made for two assemblies. Four streak cameras were fielded to measure the shock and flyer speeds on the lowest-pressure assembly, where distortion of the flyer plate was of concern, and on the highest-pressure assembly, where the faster speeds made better timing essential. All of these measurements were conducted as described for Rebound, and they returned data of comparable quality at all five pressures.

In addition to the EOS work, we used this opportunity to test new diagnostics intended for measuring the surface temperature of samples on Cimarron. While the pressure, density, and internal energy can be determined from traditional shock-wave measurements of mechanical variables, temperature cannot, and therefore it requires a separate measurement. Shock temperature is an important parameter for benchmarking the EOS, and also for studying phenomena such as insulator-metal transitions, melting, and dissociation. Furthermore, the addition of temperature as a measured quantity, when combined with measured mechanical properties, allows determination of a complete EOS. Including this type of thermodynamic information is often a much more sensitive test of theoretical models such as the EOS than pressure-volume information alone. Temperature data are also useful for modeling phase changes, such as melting and the formation of ejecta at a free surface.

Pyrometry measurements of the shocked material provide the temperature only at the sample surface or interface, while it is the

temperature behind the shock front that is of interest. However, the surface temperature is very useful in validating models that estimate the internal temperature. To obtain the free-surface temperature accurately it is necessary to eliminate ejecta from the field of view. One way to reduce the ejecta to manageable levels is by polishing the sample surface to a metallographic finish. However, plutonium is very difficult to polish and it oxidizes quickly, further compromising the surface finish. Another technique involves using a transparent window, or anvil, fastened to the plutonium surface to tamp the ejecta and maintain the release pressure at a higher value, closer to the shock pressure than for free-surface release. The interface temperature is thus closer to the internal temperature and the model validation should be more accurate. Lithium fluoride (LiF) is currently the best material for use as an anvil and as a window to transmit the radiation from the interface. Its heating under shock is low and its emissivity is small. It is important that there be no air or other shock-light-emitting material in the plutonium-LiF interface, although this is difficult to achieve because of the difficulty of polishing plutonium.

We fielded six-channel infrared pyrometers on both polished samples and samples with windows attached to determine which provides better results and to obtain data for release both into vacuum and LiF. We also fielded a comparison measurement of a polished surface and one with a coarser finish to determine whether the ejecta problem was severe enough to require polishing Cimarron samples. With the information from the Stagecoach pyrometers we were able to design the Cimarron temperature samples for optimum chances of success. Pyrometric measurements were also fielded by personnel from Sandia. Data quality and results were similar to ours.

Cimarron

As the nuclear weapons stockpile ages, it will be necessary to make occasional small changes in the materials used and the processes by which the manufacturing is done. Materials in nuclear weapons, including plutonium, HE, and plastics, are subject to change from effects such as oxidation and radioactivity. As it becomes necessary to remanufacture weapons or change out parts, we must be sure that the effects of any changes are minimized and that the changes are understood as much as possible. Furthermore, we need to make baseline measurements of current unaged weapons so that we will know when they have changed.

Cimarron was designed to study the ejecta emitted from a shocked plutonium surface. Ejecta production is sensitive to the surface roughness and oxidation, the material grain structure, and the shock profile. Cimarron diagnostics fielded by the Physics Division included holography to measure the distribution in ejecta size, x-ray shadowgraphy to measure ejected mass density, visible-light shadowgraphy to observe the ejecta cloud, fiber-optic pins to measure the shock timing and profile, pyrometry to measure the temperature of the shocked surface, and, as on the other subcritical experiments, a measurement of the energy release from the experiment to verify lack of criticality.

The in-line Fraunhofer holography technique, developed on the Pegasus pulsed-power system, has been adapted to make three-dimensional measurements of ejecta particles. Because the ejecta particles are moving at velocities of many millimeters per microsecond, a short-pulsed light source is required to stop their motion on film. Also, the explosive energy from the experiment is such that any hardware located nearby is destroyed. As a source, we used a 100-ps-pulsed, 200-mJ Nd:YAG laser with a 532-nm wavelength. This laser was developed by the Laboratory's Materials Science and Technology (MST) Division in collaboration with Bechtel Nevada. A 4.5-m-long optical relay system, consisting of 16 lenses, was designed to protect the laser and the holographic film, which were placed outside the Zero Room. The holography measurement is designed to resolve particles as small as 15 mm in diameter in a cylindrical image volume 1.5 cm in diameter and 6 mm in depth.

The x-ray imaging system also originated at Pegasus, the result of multi-year development of a unique wide-dynamic-range, four-frame framing camera; a newly-designed, blue-transmitting fiber-optic bundle; and modification of the stacked, pulsed x-ray sources used at Pegasus. The system has evolved so that ejecta can be measured over a 25-mm spatial extent at four arbitrary times. Time-dependent measurements were made possible by stacking four x-ray heads and independently triggering the anodes. Each source had a dose of 100 mRad at 30 cm. The heads were 50 to 70 cm from the imaged region and were nearly coaxial, so that they gave nearly the same view at four different times. The imaging system viewed a 4-mm-wide slot above the shocked surface using a powdered yttrium ortho-silicate (YSO) phosphor about 25 mm from the source and isolated from the plutonium region by a beryllium window. The phosphor was deposited directly onto a 120-mm-long fiber-optic plug, which was then directly coupled to a coherent fiber-optic bundle 2.7 m in length. The image passing through the bundle was reduced in size by a fiber-optic taper and connected to a blue-sensitive photocathode framing camera recently built by Bechtel Nevada. Finally, a cooled charge-coupled-device (CCD) camera coupled to the framing camera was used to record the images. The framing camera was fielded in the Zero Room in an environmentally-shielded enclosure. The increased sensitivity and uniformity of field resulting from substituting the coherent bundle for lenses permitted greatly-improved image quality. We also gained valuable experience to allow future, more complex Zero Room experiments with fewer penetrations of the containment wall.

The optical shadowgraphy system was designed around a pair of newly-developed Bechtel Nevada cameras capable of taking four images each. The four images can be gated individually with separate trigger times and intervals down to 50 ns. Light is taken from the Zero Room to the cameras using an optical line of sight, and the readout is done by a Pixel Vision $1,600 \times 1,600$-element CCD camera. System resolution for static images is about 25 µm over a 2-cm field of view. Although the system was initially intended to work with a ruby-laser backlighter, technical complications during setup dictated the removal

of the laser. Consequently the shadowgraphy experiment's emphasis was modified to observe background light and background-light-illuminated ejecta, respectively, with somewhat slower gating of the cameras.

The pins and pyrometers were similar to those described for Rebound, except that the pins served to measure the shock arrival, not the plutonium EOS. Detailed results are not available because the experiment was executed only a few days before this article was written; however, it appears that all of the Physics Division diagnostics returned their data.

Conclusions

We have now completed three subcritical experiments at the NTS. The first two studied the basic EOS of plutonium and the third studied the ejecta produced under specific conditions. All three experiments returned high-quality data. In all three experiments, energy-release measurements showed that there were no neutrons or gamma-rays produced above the level of the background radiation from spontaneous fissions in the plutonium. Given the small plutonium samples involved in the experiments, this is not at all surprising. Other experiments not involving Physics Division personnel were not described in this research highlight, but it is worth noting that DX Division and Sandia researchers fielded optical interferometers to measure spall strength, surface velocity, and total ejecta mass, while researchers from Livermore measured shock releases on Rebound and Stagecoach. Excellent data were obtained on these experiments.

Presently there are no firm plans for further EOS measurements on NTS subcritical experiments. Although more data are needed, the funding situation will not now support another major EOS experiment. Should the need for data persist, we hope to revive the EOS work on JASPER, the plutonium gas gun to be built at NTS. We will continue the ejecta studies begun on Cimarron and also begin to study plutonium spall strength on subsequent subcritical experiments.

References

[1] R. G. McQueen, S. P. Marsh, J. W. Taylor, J. N. Fritz, and W. J. Carter, "The Equation of State of Solids from Shock Wave Studies," in *High-Velocity Impact Phenomena*, R. Kinslow, Ed. (Academic Press, New York, 1970), Chap. VII.

[2] R. G. McQueen, J. W. Hopson, and J. N. Fritz, "Optical Technique for Determining Rarefaction Wave Velocities at Very High Pressures," *Review of Scientific Instruments* 53, 245 (1982).

Fundamental Symmetries with Magnetically Trapped ^{82}Rb

A. Hime, S. J. Brice,
A. Goldschmidt, and
R. Guckert (P-23); and
S. G. Crane, W. A. Taylor,
D. J. Vieira, and X. Zhao
(CST-11)
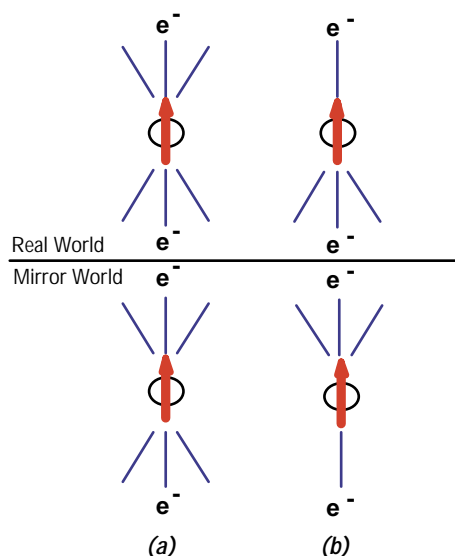
Fig. 1   (a) If parity (or space-reflection symmetry) were preserved in nuclear beta decay, no asymmetry would be detected in the distribution of electrons relative to the spin-orientation of the parent nucleus. In this scenario, the real world and mirror world would be indistinguishable. (b) Due to parity violation, electrons observed in nature exhibit an asymmetry in their angular correlation with the nuclear spin direction.

Theories of fundamental processes develop in tandem with our understanding of symmetry principles and the invariance of physical laws under specific transformations in space and time. Of the four fundamental forces in nature (strong, electromagnetic, weak, and gravity), the weak interaction is unique in that it violates parity, or space-reflection, symmetry. Four decades have passed since the first suggestion by Lee and Yang that parity could be violated in weak interactions,[1] and the subsequent discovery by Wu *et al.* of parity violation in the beta decay of polarized cobalt-60 (^{60}Co).[2] Today, maximal violation of parity is described in the standard model by a universal interaction between leptons and quarks. This model is based on empirical data established by nuclear and particle physics experiments during the second half of this century. Nonetheless, the origin of parity violation and how it is related to other conservation laws and physical processes is unresolved and marks one of the central mysteries of modern physics. Within the framework of modern gauge theories, an underlying theme speaks of spontaneously broken symmetries wherein discrete symmetries, such as parity, are restored at higher energy scales. Low-energy physics experiments that exploit nuclear beta decay continue to offer a means to probe the fundamental origin of parity violation and, more generally, the helicity structure of the weak interaction.[3]

Parity violation is manifest in nuclear beta decay as an asymmetry in the angular distribution of beta particles emitted relative to the spin orientation of the parent nucleus (see Fig. 1). In pure Gamov-Teller (GT) transitions, wherein the nucleus undergoes a change in angular momentum by one unit, the electrons are emitted preferentially in a direction opposite to the spin of the parent nucleus. Furthermore, since both the electron and the neutrino emerging from the decay must each carry away one-half unit of angular momentum (intrinsic spin) it follows that the electron must carry off its spin angular momentum aligned anti-parallel to its direction of motion. In other words, the weak interaction is *left-handed.* These, and other, observations have culminated in what we now call the standard model of weak interactions that couples leptons and quarks according to the famous vector-axial vector (V-A) prescription.

The pure GT transitions still offer the most direct route to study parity violation because they proceed solely through the axial-vector couplings responsible for parity violation. Historically, however, studies of pure GT transitions have been limited for lack of good candidates, namely reasonably long-lived and unhindered transitions. Hindered (as opposed to allowed) transitions exhibit energy-dependent behavior beyond the standard (allowed) beta spectrum, which can complicate the analysis of a precision experiment. Technical difficulties have also limited the degree of absolute nuclear polarization achievable to about 60–70%. Because uncertainty in polarization is directly reflected as an uncertainty in the correlation coefficient being measured, it is desirable to design

experiments where polarization arbitrarily close to 100% can be obtained. In addition, experiments making use of solid sources are limited by the difficulties in understanding electron scattering and energy loss effects that can masquerade as a false asymmetry. For these reasons there is little hope of breaching the 1% precision level in the study of pure GT decays using conventional techniques, and one is forced to look to new technologies to improve the situation. It is now possible to envision a new generation of pure GT experiments by exploiting optical and magnetic traps for radioactive atoms.

Our research aims specifically at exploiting magnetically trapped rubidium-82 (^{82}Rb) in a new generation of fundamental symmetry experiments. ^{82}Rb, a pure and allowed GT beta decay nucleus, has the appropriate atomic structure and lifetime (75 seconds) to be exploited in a magneto-optical trap. A prototype experiment has been mounted to measure the positron-spin correlation coefficient (A) from polarized ^{82}Rb in a magnetic TOP (time-orbiting potential) trap. In a TOP trap, an essentially massless source of highly polarized ^{82}Rb atoms is suspended in vacuum in the form of a localized cloud ~1 mm in diameter, and the direction of the magnetic bias field aligning the nuclear spin rotates uniformly in a plane.[4] We propose to exploit this rotating beacon of spin-polarized ^{82}Rb nuclei to measure the parity-violating correlation as a continuous function of the positron energy and emission angle relative to the nuclear spin orientation. The positron spin correlation function can be defined,

$$\chi(E,\Theta) = AP\beta(E)\cos\Theta ,$$

where E is the electron energy, $\beta(E)$ its velocity relative to light, Θ the angle between the electron momentum vector and the nuclear spin orientation, and P the polarization of the parent nucleus. We are planning an experiment to measure, on an event-by-event basis, the energy of the positron registered in a plastic scintillator, which will allow the determination of $\beta(E)$. Together with a snapshot of the magnetic field configuration, this will allow us to reconstruct the angle of the nuclear polarization vector relative to the momentum vector of the emitted positron ($\cos\Theta$).

While several groups are pursuing fundamental weak-interaction experiments with trapped atoms, the challenge remains to harness sufficient numbers to undertake a meaningful experiment. ^{82}Rb is the daughter product following electron-capture of the parent, strontium-82 (^{82}Sr). The ^{82}Sr source is produced at the isotope production facility of the Los Alamos Neutron Scattering Center (LANSCE) by 750-MeV proton irradiation of a molybdenum target. The strontium sample is then handled at the Chemical Science and Technology (CST) Division's hot cell, where the target is dissolved in hydrogen peroxide and the strontium fraction is extracted using an ion-exchange column. The ^{82}Rb is electrostaticly extracted from an ^{82}Sr ion source via a mass separator, where it is implanted into an yttrium foil. The ^{82}Rb is then released as a

Fig. 3   Data recorded while trapping ⁸²Rb atoms in MOT-I. The top panel shows the release of atoms from the yttrium foil (red curve) upon heating the foil to a temperature of 850° C (black-curve). The lower panel shows the modulated fluorescence signal as measured with a photomultiplier and lock-in amplifier (blue-curve) as atoms are trapped at the center of MOT-I. The peak signal of 25 nA corresponds to a trapping signal of some six million radioactive atoms, and the characteristic half-life of ⁸²Rb is observed as the radioactive atoms decay.

neutral atom by heating the foil, and it is subsequently released to a magneto-optical trap (MOT-I), as shown in Fig. 2. The neutral ^{82}Rb ions are trapped in MOT-I and confined to a 1-mm-diameter cloud at the center of a glass cell. Using an optical push-beam, the ^{82}Rb atoms are then transferred through a hexapole guide tube to a second magneto-optical trap (MOT-II). In MOT-II, they are trapped in a vacuum chamber housing the positron detector hardware. MOT-II is implemented with a set of magnetic bias coils, which are used to polarize the ^{82}Rb atoms in the TOP-trap configuration. The TOP-trap is rabily switched on such that the direction of the magnetic bias field aligning the nuclear spin rotates uniformly in a plane. The rotating, spin-polarized ^{82}Rb nuclei can then be used to measure the parity-violating correlation.

With an ^{82}Rb ion source, mass separator, and MOT in place, we have demonstrated a world record by trapping several million radioactive ^{82}Rb atoms.[5] Fig. 3 summarizes the data from these experiments. We have also demonstrated a transfer efficiency of 50% in loading the atoms into MOT-II, where the ultra-high vacuum environment provides a trapping lifetime of 500 seconds. The combination of the large trapping numbers and long trapping lifetime makes us well poised to accumulate sufficient statistics for a precision experiment.

Design of the TOP trap for fundamental symmetry investigations has posed a significant challenge. Large magnetic fields are required to achieve sufficient global polarization of the atom cloud while, at the same time, care must be taken to ensure that energy-dependent magnetic acceptance effects do not produce a false positron-spin asymmetry. Extensive Monte Carlo simulations have been implemented for the design and construction of the TOP trap to minimize systematic effects, and the hardware, including a first generation positron-telescope, are in place. We have only just begun to fully exercise our TOP trap and anticipate performing prototype measurements of the positron-spin correlation function during the coming months.

Prototype experiments will be geared to address a number of experimental details to assess our ultimate sensitivity in measuring
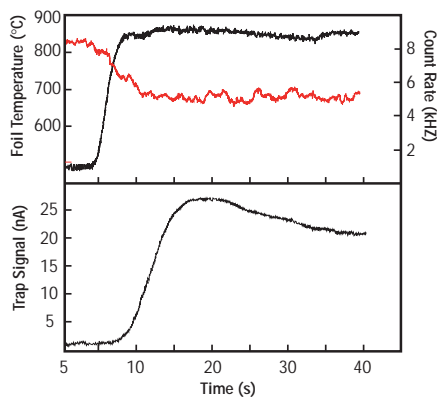
the positron-spin correlation coefficient. Perhaps the most challenging detail facing us is in our ability to ascertain the absolute polarization of the atom cloud. With systematic issues under control, the ultimate sensitivity of the experiment could be limited at the 0.5% level of accuracy due to energy-dependent, recoil-order corrections that are complicated by nuclear structure in complex nuclei. It is possible, however, to recover the recoil-order correction in a novel manner by exploiting both the asymmetry and higher multipole anistropy terms. Both terms are available in our experiment since the correlation function can be mapped out as a continuous function of both positron energy and emission angle. In this way, the data could be exploited in the search for physics beyond the standard model while extracting the recoil-order corrections experimentally and without reliance on difficult and inaccurate calculations.

We have an opportunity at Los Alamos to play an active and lead role in the next generation of fundamental symmetry experiments that exploit trapped radioactive atoms. The combination of nuclear chemistry and atomic, nuclear, and particle physics capabilities inherent in this collaboration gives us a unique potential for precision and world-class experiments that are unlikely to take place anywhere else in the world in the foreseeable future. Indeed, the success of the proposed experiment would mark the first fundamental nuclear physics experiment that exploits a TOP-trap and the first effort to measure the positron-spin correlation as a continuous function of positron energy and emission angle.

References

[1] T. D. Lee and C. N. Yang, "Question of Parity Conservation in Weak Interactions," *Physical Review* 104, 254 (1956).

[2] C. S. Wu, E. Ambler, R. W. Hayward, D. D. Hoppes, and R. P. Hudson, "Experimental Test of Parity Conservation in Beta Decay," *Physical Review* 105, 1413 (1957).

[3] J. Deustch and P. Quin, "Symmetry-Tests in Semileptonic Weak Interactions," and P. Herczeg, "Beta Decay and Muon Decay Beyond the Standard Model," in *Precision Tests of the Standard Electroweak Model, Advanced Series on Directions in High Energy Physics*, Vol. 14, P. Langacker, Ed. (World Scientific, New Jersey, 1995).

[4] W. Petrich, M. H. Anderson, J. R. Ensher, and E. A. Cornell, "Stable, Tightly Confining Magnetic Trap for Evaporative Cooling of Neutral Atoms," *Physics Review Letters* 74, 3352 (1995).

[5] R. Guckert, X. Zhao, S. G. Crane, A. Hime, W. A. Taylor, D. Tupa, D. J. Vieira, and H. Wolnik, "Magneto-Optical Trapping of Radioactive ^{82}Rb Atoms," *Physics Review A* 58, R1637 (1998).

Advances in Quantum Computation

R. J. Hughes, D. J. Berkeland,
D. Enzer, M. H. Holzscheiter,
P. G. Kwiat, S. K. Lamoreaux,
C. G. Peterson, M. M. Schauer,
and A. G. White (P-23);
J. Gomez, M. S. Gulley,
V. Sandberg, and D. Tupa (P-25);
A. G. Petschek (P-DO);
D. F. V. James (T-4);
J. M. Ettinger (NIS-8); and
M. S. Neergaard (NIS-9)
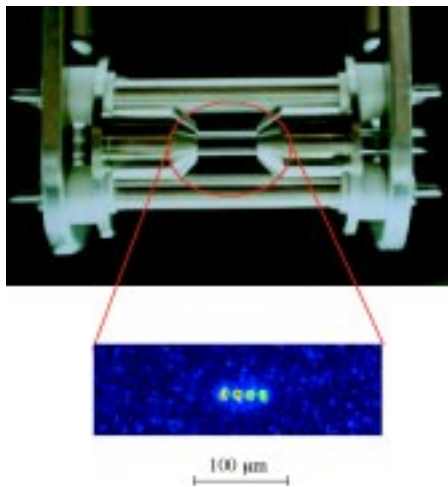
Fig. 1 A string of four calcium ions localized by laser cooling in the ion trap. The trapping region is about 1-cm long by 1.8-mm high. The image is formed by the ion fluorescence in the 397-nm cooling laser beam.

The representation of information by classical physical quantities such as the voltage levels in a microprocessor is familiar to everyone. But over the past decade, quantum information science has been developed to describe binary information in the form of two-state quantum systems, such as photon polarization states. (A single bit of information in this form has come to be known as a "qubit.")

With two or more qubits it becomes possible to consider quantum logical-"gate" operations in which a controlled interaction between qubits produces a (coherent) change in the state of one qubit that is contingent upon the state of another. These gate operations are the building blocks of a quantum computer. In principle, a quantum computer is a much more powerful device than any existing or future classical computer because the superposition principle allows an extraordinarily large number of computations to be performed simultaneously. In 1994 it was shown that this "quantum parallelism," which has no counterpart in conventional computation, could be used to efficiently find the prime factors of composite integers.[1] Integer factorization and related problems that are computationally intractable with conventional computers are the basis for the security of modern public-key cryptosystems. However, a quantum computer running at desktop personal computer speeds could break the keys of these cryptosystems in only seconds (as opposed to the months or years required with conventional computers).[2] This single result has turned quantum computation from a strictly academic exercise into a subject whose practical feasibility must be urgently determined.

The architecture of a quantum computer is conceptually very similar to a conventional computer: multiqubit, or "multibit," registers are used to input data; the contents of the registers undergo logical-gate operations to effect the desired computation under the control of an algorithm; and, finally, a result must be read out as the contents of a register. The principal obstacles to constructing a practical quantum computer are (1) the difficulty of engineering the quantum states required; (2) the phenomenon of "decoherence," which is the propensity for these quantum states to lose their coherence properties through interactions with the environment; and (3) the quantum measurements required to read out the result of a quantum computation. The first proposals for practical quantum-computation hardware, based on various exotic technologies, suffered from one or more of these problems. However, in 1994 it was proposed[3] that the basic logical-gate operations of quantum computation could be experimentally implemented with laser manipulations of cold, trapped ions: a qubit would comprise the ground (S) state (representing binary 0) and a suitably chosen metastable excited state (to represent binary 1) of an ion isolated from the environment by the electromagnetic fields

of a linear radio-frequency quadrupole (RFQ) ion trap. Figure 1 shows schematically how the constituent parts of an ion trap quantum computer come together.

The principal components of this technology are already well developed for frequency-standard and high-precision spectroscopy work. Existing experimental data suggest that adequate coherence times are achievable, and a read-out method based on so-called "quantum jumps" has already been demonstrated with single trapped ions. We are developing an ion-trap quantum computer experiment using calcium ions, with the ultimate objective of performing multiple gate operations on a register of several qubits (and possibly small computations) to determine the potential and physical limitations of this technology.[4]

The heart of our experiment is a linear RFQ ion trap with cylindrical geometry in which strong radial confinement is provided by radio-frequency potentials applied to four "rod" electrodes, and axial confinement is produced by a harmonic electrostatic potential applied by two "end caps" (Fig. 1). After laser cooling on the 397-nm transition from the ground state (S) to the excited state (P), several calcium ions will become localized along the ion trap's axis because their recoil energy (from photon emission) is less than the spacing of the ions' quantum vibrational energy levels in the axial confining potential. Although localized to distances much smaller than the wavelength of the cooling radiation, the ions nevertheless undergo small amplitude oscillations, and the lowest frequency mode is the axial center of mass (CM) motion in which all the ions oscillate in phase along the trap axis. The frequency of this mode, whose quantum states will provide a computational "bus," is set by the axial potential. The inter-ion spacing is determined by the equilibrium between this axial potential, which tends to push the ions together, and the ions' mutual Coulomb repulsion. For example, with a 200-kHz axial CM frequency, the inter-ion spacing is on the order of 20 μm.

The first excited state of a calcium ion has a long radiative lifetime (~1 second), so the transition from this level (D) to the ground state has such a narrow width that it develops upper and lower sidebands separated from the central frequency by the CM frequency. With a laser that has a suitably narrow linewidth and is tuned to the lower sideband, an additional stage of laser cooling is used to prepare the "bus" qubit (CM vibrational mode) in its lowest quantum state ("sideband cooling"). On completion of this stage, the quantum computer is prepared with all qubits in the "zero" state, ready for quantum computation (see Fig. 2).

The narrow-linewidth laser tuned to the S-D transition is the essential tool for changing the contents of the quantum register of ions and performing quantum logical-gate operations. By directing this laser at an individual ion for a prescribed time, we will be able to coherently drive the ion's quantum state between the two qubit levels that the ion represents. An arbitrary logical operation can be constructed from a small set of elementary quantum gates, such as the so-called "controlled-NOT" operation, in which the state of one qubit is flipped if a second qubit is in the "1" state but left unchanged if the second qubit is in the "0" state. This gate operation can be effected with five laser operations using quantum states of the ion's CM motion as a computational bus to convey quantum information from one ion to the other. The result of the quantum computation can be read out by turning on the S-P laser. An ion in the "0" state will fluoresce, whereas an ion in the "1" state will remain dark. So, by observing which ions fluoresce and which are dark, a value can be obtained.

To date, we have succeeded in laser-cooling calcium ions into crystalline strings in our ion trap, which will be used as a quantum register. We used a charge-coupled device (CCD) camera to image ion strings of various lengths (see Fig. 1).

Fig. 2   A schematic representation of an ion trap quantum computer. Within the cylindrical RFQ ion trap, ions are radially confined by radio-frequency potentials applied to the four rod electrodes and axially confined by a harmonic electrostatic potential applied to the end caps. After a first stage of laser cooling, ions become localized along trap's axis. A second stage of laser cooling cools the ions to their lowest quantum states. The quantum computer is then ready for computation.

Ions localized in trap after laser cooling

Coherent laser interactions with ion change register values
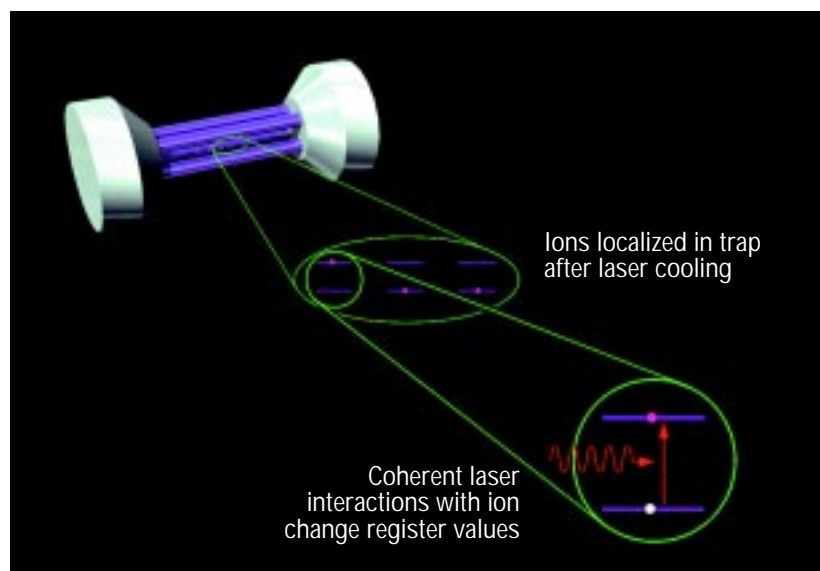
In addition, we have developed an optical system that can direct the computational laser beam with low-crosstalk to individual ions and rapidly switch the beam from ion to ion as required for quantum computational operations. We have also studied the intrinsic computational potential of ion-trap quantum computers. By taking into account the relevant decoherence mechanisms, we have found that on the order of one million gate operations could be performed on registers of 50 or so ions.[5] This is a tremendous amount of quantum computation relative to the current state of the art: one logic operation on two qubits. We have also performed a theoretical study of the mechanisms causing ion heating, which limit the amount of computation possible in an ion trap system, and we have determined how the heating rate depends on critical parameters such as the trap dimensions and frequencies. Because a quantum computer can create an arbitrary quantum state using quantum logic operations, this computational capacity opens up a wide variety of quantum-mechanics experiments in domains that are today inaccessible. We expect therefore that ion-trap quantum computers will allow us to explore quantum computation and the foundations of quantum mechanics.

References

[1] P. W. Shor, "Algorithms for Quantum Computation: Discrete Logarithms and Factoring," 35th Annual Symposium on the Foundations of Computer Science (Santa Fe, New Mexico, 1994), *Proceedings of the 35th Annual Symposium on the Foundations of Computer Science*, S. Goldwasser, Ed. (IEEE Computer Society Press, Los Alamitos, California, 1994) p. 124–134.

[2] R. J. Hughes, "Crytography, Quantum Computation, and Trapped Ions," *Philosophical Transactions of the Royal Society of London A* 356, 1853 (1998).

[3] J. I. Cirac and P. Zoller, "Quantum Computation with Cold, Trapped Ions," *Physics Review Letters* 74, 4094 (1995).

[4] R. J. Hughes, *et al.*, "The Los Alamos Trapped Ion Quantum Computer Experiment," *Fortschritte der Physik* 46, 329 (1998).

[5] R. J. Hughes, *et al.*, "Decoherence Bounds on Quantum Computation with Trapped Ions," *Physical Review Letters* 77, 3240 (1996).

Practical Free-Space Quantum Key Distribution

W. T. Buttler, R. J. Hughes, P. G. Kwiat, S. K. Lamoreaux, G. G. Luther, G. L. Morgan, J. E. Nordholt, C. G. Peterson, and C. M. Simmons (P-23)

Introduction

Quantum cryptography was introduced in the mid-1980s[1] as a new method for generating the shared, secret random number sequences, known as cryptographic keys, that are used in cryptosystems to provide communications security. Existing methods of key distribution derive their security from the perceived intractability of certain problems in number theory (which grow more vulnerable as computers grow more powerful), or from the physical security of the distribution process (which often depends upon couriers, increasing the likelihood that the key might be compromised). The appeal of quantum cryptography is that its security is based on the natural laws governing the behavior of photons, laws that solidly guard against the possibility of successful eavesdropping and interception.

In past years, our team has played a major role in demonstrating that quantum key distribution (QKD) is possible over multikilometer distances of optical fiber.[2, 3, 4] Free-space QKD, however, presents a greater challenge. The success of free-space QKD depends on the ability to transmit and detect single photons against a high background (that is, interference from other photon sources) and through a turbulent medium (the air). Building on previous efforts to demonstrate free-space QKD[5,6] we have developed and successfully tested a QKD system over an outdoor free-space optical path of close to 1 km under nighttime conditions. Our results, which were reported in *Physical Review Letters*[7], show that free-space QKD can provide secure, real-time key distribution between parties who need to communicate secretly. This has definite practical advantages over fiber optic systems, making QKD a viable alternative for secure surface-to-satellite communications.

Demonstration and Results

The QKD transmitter in our demonstration (Fig. 1) consisted of a temperature controlled single-mode (SM) fiber pigtailed diode laser, a fiber to free-space launch system, a 2.5-nm bandwidth interference filter (IF), a variable optical attenuator, a polarizing beam splitter (PBS), a low-voltage Pockels cell, and a $27\times$ beam expander. The diode laser wavelength was temperature-adjusted to 772 nm, and the laser was configured to emit a short pulse of approximately 1-ns duration, containing $\sim 10^5$ photons.
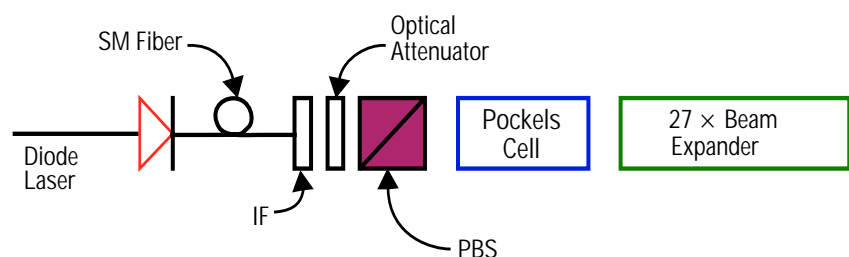

Fig. 1 Diagram of our free-space QKD transmitter.

In our QKD system, the sender, "Alice," starts by generating a secret random binary number sequence. Using a computer control system, Alice pulses the laser at a rate previously agreed upon between herself and the recipient, "Bob." Each laser pulse is launched into free space through the IF, and the pulse is then attenuated to an average of less than one photon per pulse, based on the assumption of a statistical Poisson distribution. The photons that are transmitted by the optical attenuator are then polarized by the PBS. Alice and Bob agree in advance on the polarization states that she will send, as well as those he will measure; their algorithm can be shared with the public without threatening the security of the system. In our demonstration, we used the B92 protocol.[8] The PBS was set to transmit an average of less than one horizontal-polarized photon, $|h>$, to the Pockels cell, and the Pockels cell was then randomly switched to either pass the light unchanged as $|h>$ (zero-wave retardation) or change it to a right-circular-polarized photon, $|r>$ (quarter-wave retardation).

The QKD receiver in our demonstration (Fig. 2) used an 8.9-cm Cassegrain telescope to collect the photons and direct them to the receiver optics and detectors. The receiver optics consisted of a 50/50 beam splitter (BS) that randomly directed the photons onto either of two distinct optical paths, each of which measures for one of the agreed-upon polarization states. One output port along each optical path was coupled by multimode (MM) fiber to a single-photon counting module (SPCM). Although the receiver did not include IFs, the spatial filtering provided by the MM fibers effectively reduced ambient background noise during nighttime operation (~1.1 kHz) to negligible levels. The lower optical path contained a polarization controller (a quarter-wave retarder and a halfwave retarder) followed by a PBS to test collected photons for $|h>$; the upper optical path contained a half-wave retarder followed by a PBS to test for $|r>$.
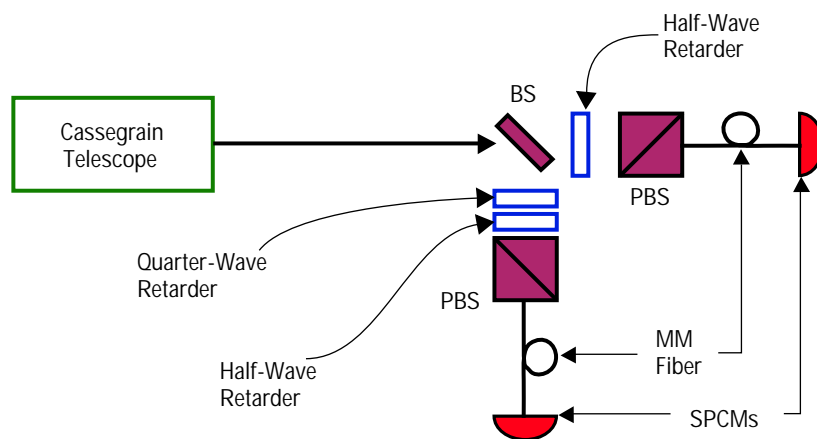
Fig. 2 Diagram of our free-space QKD receiver.

Note that Bob does not look for Alice's original states, but for related states. This ensures that Bob will never detect a photon for which he and Alice have used a preparation/measurement pair that corresponds to different bit values, which happens for 50% of the bits in Alice's sequence. For example, a single $|r>$ photon traveling along the lower path encounters the polarization controller and is converted to $|v>$ and reflected away from the SPCM by the PBS. Conversely, a single $|h>$ photon traveling the same path is converted to $|r>$ and transmitted toward or reflected away from the SPCM in this path with equal probability. Similarly, a single $|h>$ photon traveling the upper path encounters a half-wave retarder and is converted to $|v>$ and is reflected away from the SPCM in this path, but a single $|r>$ photon traveling this path is converted to a left-circular-polarized photon, $|l>$, and transmitted toward or reflected away from the SPCM with equal probability. Thus, by detecting single photons, Bob identifies only a random 25% portion of the bits in Alice's random bit sequence, assuming a single photon Fock state with no bit loss in transmission or detection. This 25% efficiency factor is the price that Alice and Bob must pay for secrecy.

To complete the QKD procedure, Bob and Alice reconcile their common bits through a public discussion by revealing the locations, but not the bit values, in the sequence where Bob detected photons; Alice retains only those detected bits from her initial sequence. The resulting detected bit sequences comprise the raw key material from which a pure key is distilled using classical error detection techniques. Once Alice and Bob share this unique key, they can code, transmit, and decode messages securely.[7]

In our demonstration, we operated the transmitter and receiver optics over 240-, 500-, and 950-m outdoor optical paths under nighttime conditions with the transmitter and receiver collocated to simplify data acquisition. All optical paths were achieved by reflecting the emitted beam from a 25.4-cm mirror positioned at the halfway point of the transmission distance.

Results for the 950-m path showed a bit error rate (BER), defined as the ratio of the bits received in error to the total number of bits received, of ~1.5% when the system was operating at a level of ~0.1 photons per pulse (BERs of ~0.7% and ~1.5% were observed for the 240-m and 500-m optical paths, respectively). A sample of raw key material from the 950-m test, including errors, is shown in Fig. 3. Using narrow gated coincidence timing windows (~5 ns) and spatial filtering, we minimized the bit errors due to ambient

Fig. 3   A sample of the sender's and receiver's raw key material, which was generated in our demonstration across a free-space distance of ~1 km. Only two errors, indicated in red, occurred during this transmission.

Sender's raw key:
111111100000010101011011111100111111011110101001101001011101111
Receiver's ray key:
11111010000001010101101111110001111101111010100110100101110111 1

background to less than ~1 every 9 seconds. Further, because detector dark noise (~80 Hz) contributed only about one dark count every 125 seconds, we believe that the observed BER was mostly caused by misalignment and imperfections in the optical elements (wave plates and Pockels cell). While this BER surpasses even the BER attained with our fiber systems[2,3,4], any BER may potentially be caused by an eavesdropper. "Privacy amplification" must therefore be applied.[9]

Toward QKD for Satellite Communications

One of the goals of our demonstration was to evaluate the feasibility of conducting free-space QKD between a ground station and a satellite in a low-earth orbit. We designed our QKD system to operate at a wavelength of 772 nm, at which the atmospheric transmission from surface to space can be as high as 80%, and for which single-photon detectors with efficiencies as high as 65% are commercially available; at these optical wavelengths, atmospheric depolarizing effects are negligible, as is the amount of Faraday rotation experienced on a surface-to-satellite path.

To detect a single QKD photon it is necessary to know when it will arrive. The photon arrival time can be communicated to the receiver by using a bright precursor reference pulse. Received bright pulses allow the receiver to set a 1-ns time window within which to look for the QKD photon. This short time window reduces background photon counts dramatically. Background can be further reduced by using narrow bandwidth filters.

Atmospheric turbulence introduces beam wander, impacting the rate at which QKD photons would arrive at a satellite from a ground-station transmitter. The optical influence of turbulence is dominated by the lowest ~2 km of the atmosphere, the region in which our demonstration was conducted; the results of our 1-km experiment provide strong evidence that surface-to-satellite QKD will be feasible.

Assuming 30-cm diameter optics at both the transmitter and satellite receiver[7] and worst-case atmospheric "seeing" of 10 arc-seconds, we estimate that with a laser pulse rate of 10 MHz, an average of one photon per pulse, and atmospheric transmission of ~80%, photons would arrive at the collection optic at a rate of 800 to 10,000 Hz. Then, with a 65% detector efficiency, the 25% intrinsic efficiency of the B92 protocol, IFs with transmission efficiencies of ~70%, and a MM fiber collection efficiency of ~40%, a key generation rate of 35–450 Hz is feasible. With an adaptive beam tilt corrector, the key rate could be increased to about 3.5–45 kHz; these rates would double using the BB84 protocol.

Another challenge for surface-to-satellite QKD is the influence of ambient background. From our preliminary estimates of background photon rates during the full moon and new moon, we infer BERs of $\sim 9 \times 10^{-5}$ to 9×10^{-3} and $\sim 2 \times 10^{-6}$ to 3×10^{-5}, respectively. During daytime orbits the background radiance will be ~1% larger. We have recently demonstrated point-to-point, free-space QKD in daylight conditions. Results from initial tests have been positive, promising solutions to the challenge of distinguishing the single-photon signal in a bright background.

Already, our results show that QKD between a ground station and a low-earth orbit satellite should be possible on nighttime orbits, and possibly even in full daylight. During the several minutes that a satellite would be in view of the ground station there would be adequate time to generate tens of thousands of raw key bits, from which a shorter error-free key stream of several thousand bits would be produced after error correction and privacy amplification. If our tests in daylight conditions prove successful, it will remove the last great obstacle to this technology, ensuring that the promise of secure, surface-to-satellite communications becomes a reality.

References

[1] C. H. Bennett and G. Brassard, "Quantum Cryptography: Public Key Distribution and Coin Tossing," in *Proceedings of the IEEE International Conference on Computers, Systems, and Signal Processing, Bangalore, India* (IEEE, New York, 1984), p. 175.

[2] R. J. Hughes, D. M. Alde, P. Dyer, G. G. Luther, G. L. Morgan, and M. Schauer, "Quantum Cryptography," *Contemporary Physics* **36**, 149 (1995).

[3] R. J. Hughes, *et al.*, "Quantum Cryptography Over Underground Optical Fibers," *Lecture Notes Computational Science* 1109, 329 (1996).

[4] R. J. Hughes, "Secure Communications using Quantum Cryptography," *SPIE Proceedings* 3076, 2 (1997).

[5] W. T. Buttler, R. J. Hughes, P. G. Kwiat, G. G. Luther, G. L. Morgan, J. E. Nordholt, C. G. Peterson, and C. M. Simmons, "Free-Space Quantum-Key Distribution," *Physical Review A* 57, 2379 (1998).

[6] B. C. Jacobs and J. D. Franson, "Quantum Cryptography in Free Space," *Optical Letters* 21, 1854 (1996).

[7] W. T. Buttler, R. J. Hughes, P. G. Kwiat, S. K. Lamoreaux, G. G. Luther, G. L. Morgan, J. E. Nordholt, C. G. Peterson, and C. M. Simmons, "Practical Free-Space Quantum Key Distribution Over 1 km," *Physical Review Letters* 81, 3283 (1998).

[8] C. H. Bennett, "Quantum Cryptography using any Two Nonorthogonal States," *Physical Review Letters* 68, 3121 (1992).

[9] C. H. Bennett, *et al.*, "Generalized Privacy Amplification," *IEEE Transactions on Information Theory* 41, 1915 (1995).

"Interaction-Free" Measurements: The In's and Out's of Quantum Interrogation

P. G. Kwiat and A. G. White (P-23)

For those of us familiar with quantum mechanics, it is common belief that a measurement on a system will necessarily disturb it (unless the system is already in an eigenstate of the measurement observable). This makes the concept of "interaction-free" measurements all the more intriguing. By incorporating the principle of complementarity and the "quantum Zeno effect," one can in fact achieve just such a measurement, in which the presence of an opaque object is determined optically, but with a negligibly small chance that the object absorbs or scatters any light in the process.

The idea was first proposed several years ago by Elitzur and Vaidman. They suggested using a simple interferometer, balanced so that an incident photon would always exit to a particular output port—the other port would remain dark due to complete destructive interference of the two paths in the interferometer; here a wave-like description is appropriate. However, the presence of an object in one arm will disrupt this interference. Now a particle-like description is more appropriate to account for the distinguishable trajectories of the photon. At the first beamsplitter, the photon has a 50% probability to take the path containing the object and be absorbed. But half the time the photon will take the other path; moreover, at the second beamsplitter, there is no longer any interference, so the photon will have a net 25% chance of going to the previously dark port. A "click" at the detector in this port unambiguously indicates the presence of the object, even though the photon could not have taken the path containing the detector (for then it would have been absorbed). Such measurements were termed "interaction-free," although the *possibility* of an interaction is crucial.

We have modified the basic idea of Elitzur and Vaidman to incorporate the possibility of *imaging*. A schematic of our setup is shown in Fig. 1. A photon polarized at 45° is incident on a polarizing Mach-Zehnder interferometer. The first polarizing beamsplitter transmits the horizontal component of the light and reflects the vertical component. These two are then recombined at the second polarizing beamsplitter. The polarization of the light is then measured in the 45/-45° basis. If the two paths are unimpeded and the path lengths are the same, then the light will still be polarized at 45°. If, on the other hand, there is an object in the vertical-polarization arm, then any light leaving the interferometer will be horizontally polarized, and hence will have a 25% chance of being detected by the -45° detector, an "interaction-free" quantum interrogation. By including a focusing lens before the interferometer and a similar collecting lens after it, we were able to create a small beam waist, through which we scanned a variety of ~one-dimensional objects, such as hairs, wires, optical fibers, *etc.* A typical example is shown in Fig. 2. With this system we were able to achieve a resolution of about 10 μm.
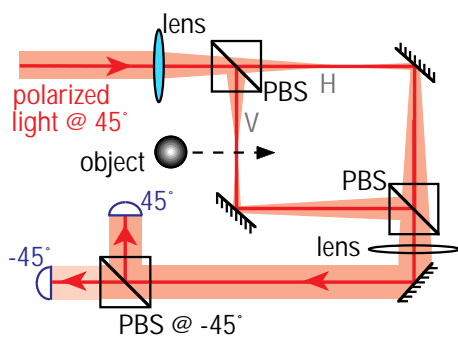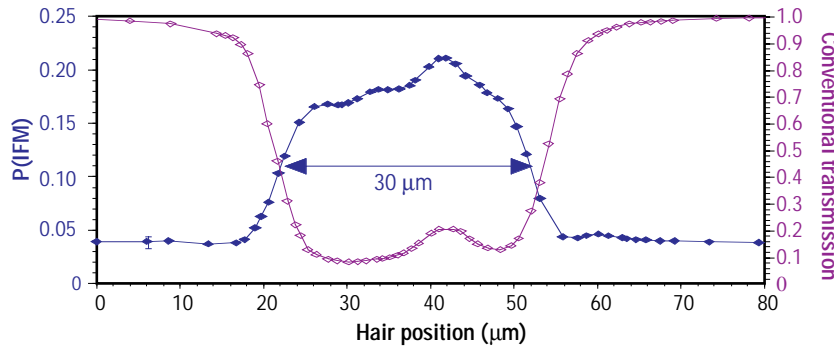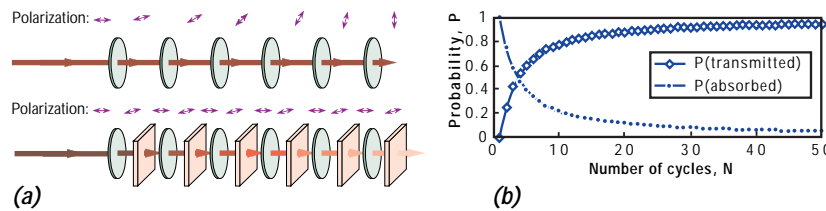

Fig. 1 Schematic of experimental setup to demonstrate the principle of "interaction-free" measurements, modified to allow one-dimensional imaging.

One immediate problem of the system proposed by Elitzur and Vaidman is that the object still absorbs the photon some fraction of the time. In fact, by varying the reflectivities of the interferometer beamsplitters (or by varying the input and analysis polarization in our imaging setup), one can affect the efficiency of the technique (see Fig. 3). Nevertheless, one can never get an efficiency over 50%, *i.e.*, at most half of the measurements will be "interaction-free."

Along with collaborators at the University of Innsbruck in Austria, we have discovered a way in which one can in principle achieve efficiencies arbitrarily close to 1 (*i.e.*, the probability of absorption by the object can be arbitrarily small). A new quantum phenomenon must be utilized, namely the Quantum Zeno effect. A simple optical example is shown in Fig. 4a. A single horizontally-polarized photon is directed through a series of N polarization rotators (for concreteness we could imagine using an optically-active sugar solution), each of which rotates the polarization by $\Delta\theta = \pi/2N$; thus upon exiting the system, the photon now has
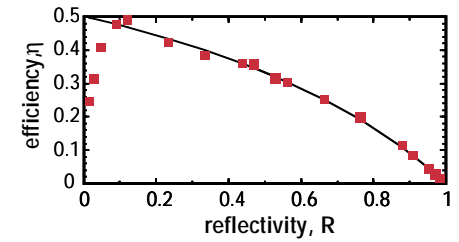

Fig. 3   The measured efficiency of the Elitzur-Vaidman technique as the effective reflectivity of the beamsplitters is varied. The solid curve is the theoretical prediction. The deviation of the experimental results for small reflectivities is due to unavoidable "crosstalk" in the polarizing beamsplitters (i.e., a small amount of horizontally-polarized light is reflected).

Fig. 4   (a) The quantum Zeno effect. In the top image, a single photon with horizontal polarization is rotated stepwise to vertical by a series of polarization rotators (green disks). The bottom image shows how this quantum evolution may be inhibited by interspersing a series of horizontal polarizers (red squares), which continually project the photon back into its original state. (b) Calculated probabilities of transmission and absorption through the system, as a function of the number of cycles.

vertical polarization. We may inhibit this stepwise evolution by making a measurement of the polarization at each stage. This may be accomplished by inserting a horizontal polarizer after each rotation element. Since the probability of being transmitted through each polarizer is just $\cos^2(\Delta\theta)$, the probability of being transmitted through all N of them is simply

$$\cos^{2N}(\Delta\theta) = \cos^{2N}(\pi/2N) \approx 1 - \pi^2/4N,$$

and the complementary probability of absorption is $P(\text{abs}) \approx \pi^2/4N$ (see Fig. 4b). Hence, by increasing the number of cycles, one can in principle have an arbitrarily small probability that the photon is absorbed by one of the polarizers, and yet, because the photon exits the system still in its initial horizontal polarization state, we know the polarizers are present.

Obviously the system from Fig. 4a is of limited use because it only works with polarizing objects. To be able to make a quantum interrogation of *any* nontransmitting object, one needs a hybrid solution. We have developed and tested such a system. The basic concept is shown in Fig. 5. A single photon is made to circulate N times through the setup before it is somehow removed and its polarization analyzed. As in the Zeno example, the photon initially has horizontal polarization, and is rotated by $90°/N$ on each passage through the rotator. In the absence of any object, the polarization-interferometer has absolutely no effect on the polarization of the light; it merely breaks the light into its horizontal and vertical components and adds them back with the same relative phase. Hence, if there is no object, after N cycles the photon is found to have vertical polarization. On the other hand, if there *is* an object in the vertical arm of the interferometer, only the horizontal component of the light is passed, *i.e.*, each *non*absorption by the object—with probability $\cos^2(\Delta\theta)$—projects the wavefunction back into its initial state. In this case, after N cycles, either the photon will still have horizontal polarization, unambiguously indicating the presence of the object, or the object will have absorbed the photon. And by going to higher N, the probability of absorption can in principle be made arbitrarily small.

To demonstrate this phenomenon in an actual experiment, several modifications were made (see Fig. 6). First, a horizontally-polarized pulsed laser was coupled into the system by a highly reflective mirror. The light was attenuated so that the average photon number per pulse after the mirror was only ~0.3. The photon then bounced several times between this recycling mirror and one of the mirrors making up a Michelson polarization interferometer (like a normal Michelson interferometer, but with a polarizing
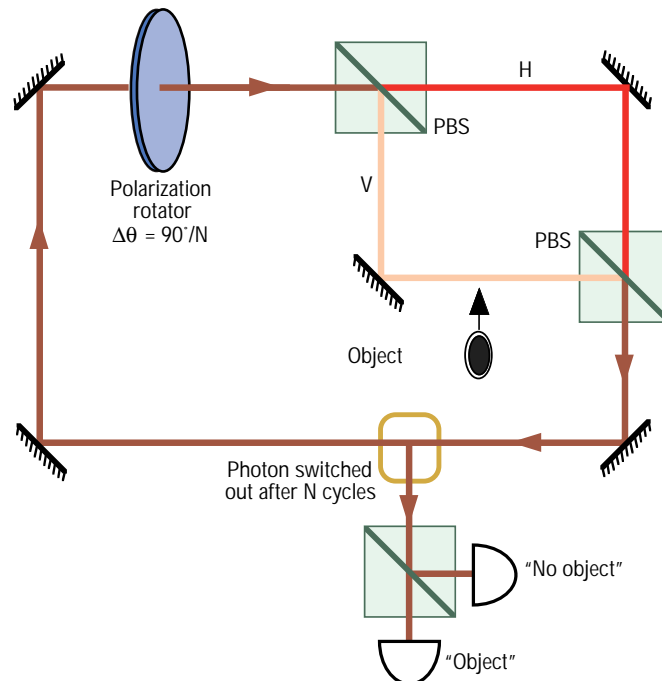
Fig. 5   Simplified schematic of a hybrid system, combining the quantum Zeno effect with a polarization interferometer to allow >50% efficient interaction-free measurements.

beamsplitter instead). At each cycle the polarization was rotated by a specific amount, and after the desired number of cycles the photon was switched out of the system using the high-voltage Pockel's cells in the interferometer arms. The photon was then analyzed using an adjustable polarizer, and detected by a single-photon detector. In the absence of any object in the vertical arm of the interferometer, the polarization was found to be essentially vertical, indicating that the stepwise rotation of polarization had taken place. In the presence of the object, this evolution was inhibited, and the photons exiting the system were still horizontally-polarized, an interaction-free measurement of the presence of the object. The fraction of measurements that were interaction-free was measured as the number of cycles N was increased (and the rotation angle, $\Delta\theta$, was correspondingly decreased).

   Rather unexpectedly, we found that after an initial increase in efficiency, the efficiency actually decreased toward zero past some optimal number of cycles. A detailed theoretical calculation verified that this decrease arises due to loss in the system: basically, a photon that makes it to the detector experiences the single-cycle loss N times, while a photon that is absorbed by the object (which may happen at any cycle), experiences this loss only $\sim N/2$ times. The net effect is to reduce the efficiency for high-cycle numbers
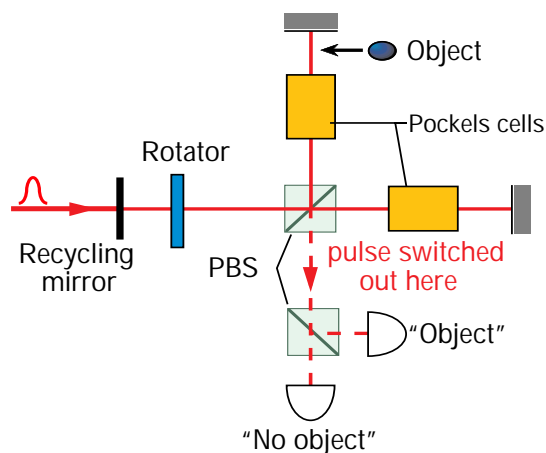

Fig. 6 Experimental setup to demonstrate high-efficiency quantum interrogation. A photon remains in the system for N cycles, at which time the Pockel's cells are activated and the light is switched out. The polarization of the exiting photons depends on whether or not an object is blocking the vertical-polarization arm of the interferometer.

rather than having it asymptote to 1. Figure 7 shows the experimental verification of this phenomenon, as well as the theoretical predictions, which are in good agreement. Despite this effect, we were able to observe efficiencies of up to 73%, which means that the presence of the object could be ascertained with only one-fourth of a photon being absorbed. Ours was the first measurement to break the 50% limit of the simple Elitzur-Vaidman technique. In addition, we have made measurements which confirm the feasibility of efficiencies up to 85%. And we now think we have a method to improve our system so that the probability of absorption could be as low as 1–2%. If these methods could be combined with the imaging techniques already explored, one would have a very useful tool for noninvasive diagnostics, *e.g.*, of delicate biological specimens or even photosensitive chemical reactions.

Another very interesting area we are studying is the possibility of making such quantum interrogations of truly quantum mechanical objects, such as single atoms or ions. The advantage of this is that the quantum object can be readily prepared into a superposition of states, one of which is sensitive to the "interaction-free" measurement technique, and one of which is not. Theoretical calculations predict that the state of the light and the state of the object will then become quantum mechanically *entangled*. Remarkably, it seems that this will be true even for light pulses containing several photons. If the object were measured to be in its

Fig. 7   Plot of experimentally measured efficiency versus number of cycles for several different values of loss.
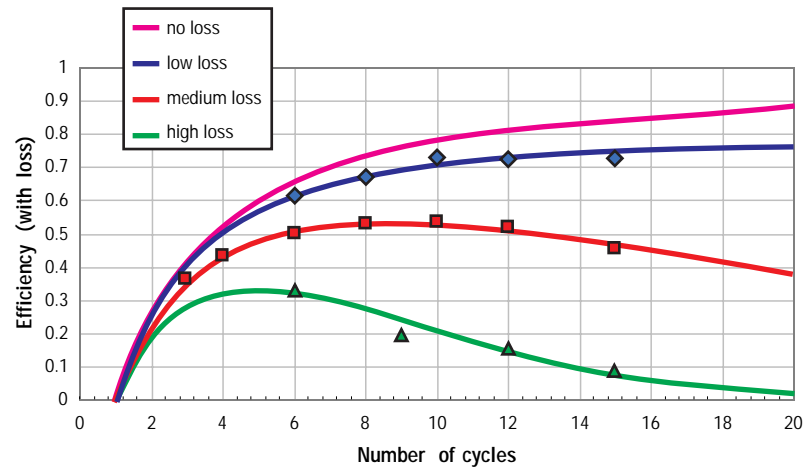
initial state, one would then have a multiphoton pulse of light, in a superposition of horizontal and vertical polarization. This is an example of a Schrödinger cat and would open the door to a whole range of fundamental experiments on the nature of decoherence. It would also help to answer the question of why we do not observe macroscopic quantum superpositions in our everyday lives, even though we believe that quantum mechanics is a correct description of nature. One practical application of these interaction-free measurements of quantum objects is as a sort of quantum "interface" for connecting together different quantum computers (a separate research highlight addresses our contributions to quantum computation).

Further Reading

P. G. Kwiat, "Experimental and Theoretical Progress in Interaction-Free Measurements," *Physica Scripta* T76, 115 (1998).

P. G. Kwiat, H. Weinfurter, T. Herzog, A. Zeilinger, and M. A. Kasevich, "Interaction-Free Measurement," *Physical Review Letters* 74, 4763 (1995).

P. G. Kwiat, H. Weinfurter, and A. Zeilinger, "Interaction-Free Measurement of a Quantum Object: On the Breeding of 'Schrödinger Cats,'" in *Coherence and Quantum Optics VII*, J. Eberly, L. Mandel, and E. Wolf, Eds. (Plenum Publishing, 1996).

P. G. Kwiat, H. Weinfurter, and A. Zeilinger, "Quantum Seeing in the Dark," *Scientific American*, November 1996, pp. 52–58.

A. G. White, J. R. Mitchell, O. Nairz, and P. G. Kwiat, "'Interaction-Free' Imaging," *Physical Review A* 58, 605 (1998).

Plasma Source Ion Implantation Research, Development, and Applications

C. P. Munson, B. Cluggish (currently at Archimedes, San Diego), and B. Wood (P-24); and Kevin Walter (MST-8)

Introduction

Plasma Source Ion Implantation (PSII) is a room temperature, plasma-based, surface enhancement technology that uses an ionized gas surrounding a target and high-negative-voltage, high-current pulses to accelerate ions into a target surface from all directions. Ion implantation can modify the target surface in beneficial ways, making it harder, reducing the coefficient of friction, and enhancing its resistance to corrosion.[1,2,3,4,5,6,7,8,9,10] These benefits are similar to those obtained through conventional ion beam implantation[11,12], but PSII differs from conventional techniques in several important aspects (see Fig. 1). First, ions are accelerated into the target through a plasma sheath[13] that surrounds the target, so the process is not "line-of-sight"—there is no requirement of an unobstructed path from a single ion source to the surface being treated. This allows PSII to treat multiple target surfaces and even multiple targets simultaneously without the need for in-vacuum manipulation of the target assembly. In addition, the average ion current to the target surface can be more than an order of magnitude larger than using conventional techniques[14,15,16], significantly reducing the required treatment time for large, complex target assemblies. This increase in average ion current is possible because nearly the entire target surface (potentially many square meters in area) can be treated simultaneously with a high pulsed-current source. Spreading the total applied current over a large surface area also tends to minimize local surface heating effects.

Plasma Source Ion Implantation

Conventional Ion Beam Implantation

Fig. 1 Schematic comparison of PSII and conventional ion beam implantation. PSII uses the plasma sheath to accelerate ions into the target (or multiple targets) from all directions. Conventional, accelerator-based ion implantation is a line-of-sight process, which requires in-vacuum manipulation of a target to implant complex surfaces.
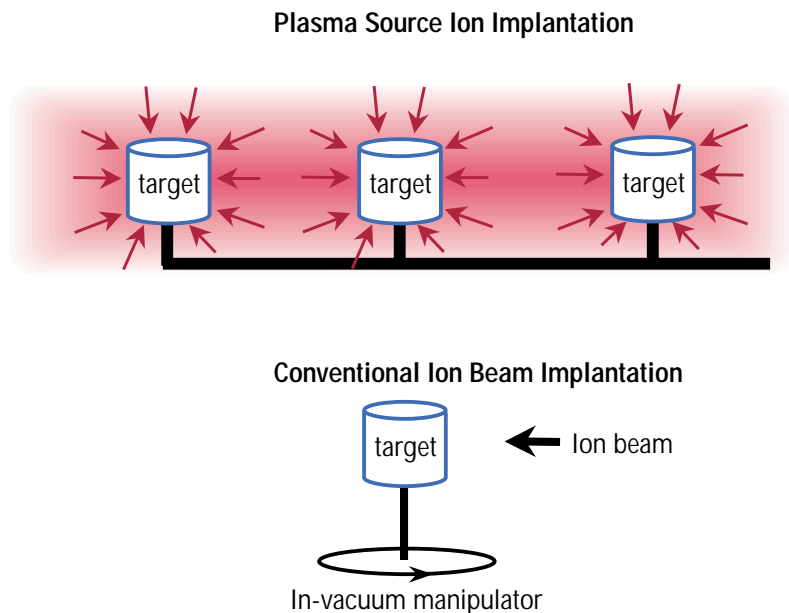
PSII was originally patented by John Conrad of the University of Wisconsin, Madison, and has been further developed and demonstrated at industrially relevant scales by researchers at Los Alamos in collaboration with the University of Wisconsin and General Motors Research. This technique is currently being commercialized through the efforts of General Motors, Asea Brown Boveri, Litton Electron Devices, Nano Instruments, Diversified

Technologies, Ionex, PVI, Empire Hard Chrome, A. O. Smith, Harley-Davidson, Kwikset, Boeing, and DuPont, as well as Los Alamos National Laboratory and the University of Wisconsin at Madison in a National Institute of Standards and Technology Advanced Technology Program project managed by the Environmental Institute of Michigan, Ann Arbor. The success of this research and development (R&D) effort earned an R&D 100 award from *R&D Magazine* in 1996 (Fig. 2).

There are several key factors that must be considered to successfully design and operate a commercial PSII system. These include the surface material science, overall vacuum system design, plasma source requirements, plasma-target interaction considerations, pulsed high-voltage subsystem (modulator) requirements, and target requirements and limitations. Critical system components are outlined in Fig. 3. This research highlight will focus on several important plasma physics effects related to the plasma-target interaction, particularly in the case of large, complex, multiple-component, target assemblies.
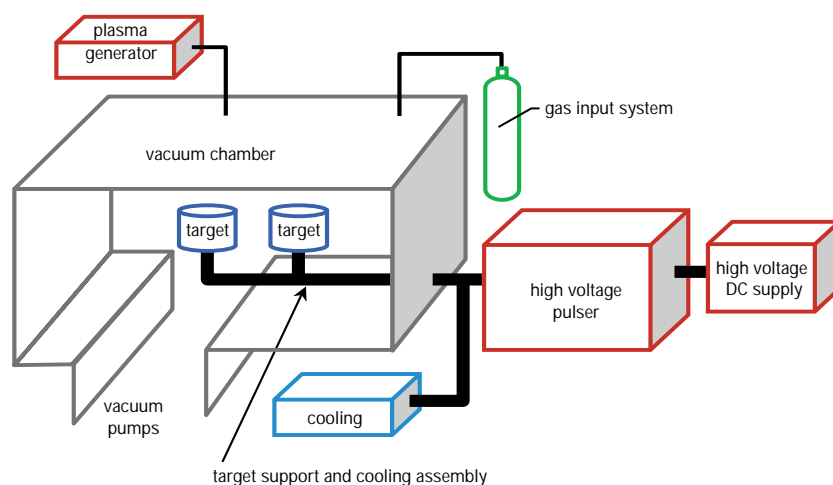
Fig. 3 Block diagram of a typical PSII system. Major system components include the vacuum chamber, pumping system, high voltage DC power supply, high voltage pulser or modulator, cooling system, target support assembly, plasma generation system, and working gas input system.
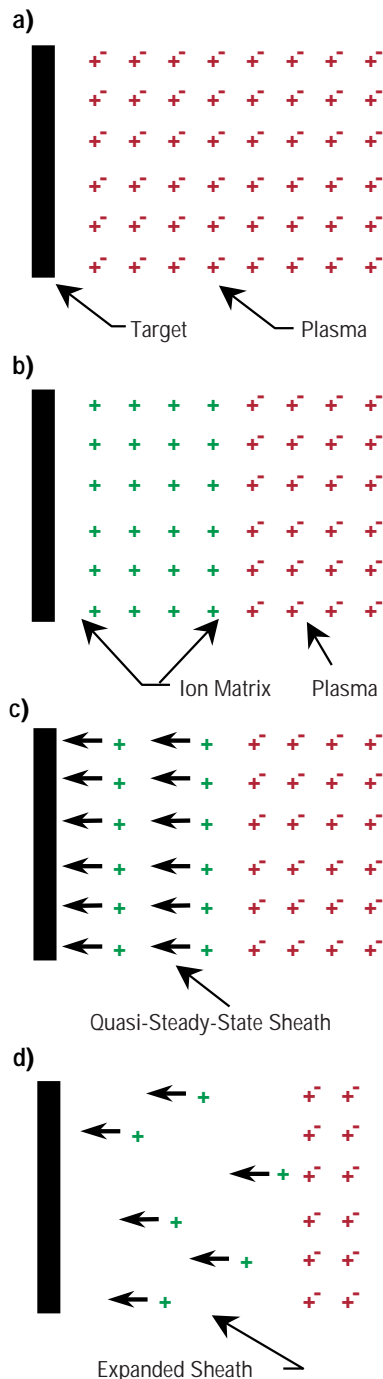
Fig. 4 Plasma sheath temporal behavior for a planar target. Shown are the initial configuration with nearly uniform plasma surrounding the target (a), the formation of the ion matrix after electrons have been excluded from the region close to the target (b), ions accelerating through the sheath region into the target surface (c), and the expanded sheath late in the voltage pulse (d).

Basic Plasma Sheath Physics

During the PSII process, a negative high voltage pulse is applied to create a transient plasma sheath[17,18,19] around the target and accelerate ions into the target surface. The characteristics of the plasma sheath play a major role in the PSII process. The fundamental evolution of the plasma sheath is illustrated in Fig. 4. In simple configurations (uniform plasma density and geometrically simple targets) the dimensions of the sheath are determined primarily by the initial plasma density, the voltage applied to the target, and the duration of the voltage pulse. In the basic initial configuration (Fig. 4a) a nearly uniform plasma surrounds the target. The great difference in mass between the electrons and ions in the plasma causes the electrons to move rapidly away from the target during the early portion of the voltage pulse, exposing plasma ions (Fig. 4b). The electric field established in the sheath region accelerates ions into the target (Fig. 4c). As ions are implanted into the target and lost from the sheath, the sheath edge recedes from the target (Fig. 4d). The sheath thickness increases during this time. Eventually, the sheath edge will extend to the vacuum chamber wall, or arcing will occur, limiting the useful pulse duration for implantation. Typical pulse widths, therefore, range from several microseconds to almost 100 μs.

From the fundamental equations describing the sheath evolution, it is clear that higher initial plasma densities result in smaller sheaths. Sheath dimensions that are small compared to the scale size of important target features result in more uniform implantation of the critical target surfaces, but require larger currents from the modulator.

Plasma Sheath and Target Interactions

A serious factor affecting PSII's commercial success is the production of secondary electrons.[8] Secondary electrons are produced when plasma ions impact the target surface, with each high-energy (many keV) ion potentially displacing a large number of electrons upon impact. For an aluminum target biased to 40 kV, as many as 19 secondary electrons are produced by each ion.[20] This would indicate an ion implantation efficiency of only 5% for the PSII process, since the total current that must be supplied by the modulator is composed of both the ion and secondary electron currents.

Under certain circumstances, the secondary electrons, rather than being a nuisance, may actually enhance the plasma discharge. The secondary electrons are repelled by the strong negative potential of the target and are accelerated to high energy in their outward passage through the sheath surrounding the target. When multiple, large, complex target assemblies are being treated with PSII, secondary electrons emitted by one portion of the target may be reflected from the sheath edge associated with other portions of the target surface, resulting in an increase in the residence time of the secondaries in the plasma. A larger portion of the energy of the

secondary electrons is then deposited into the plasma, producing increased ionization and higher plasma densities than could be achieved without the secondaries.

Figure 5 shows the target assembly used in our experiments immersed in a background plasma. The assembly consists of four vertical racks consisting of 504 cylindrical targets (surrogates for aluminum automotive pistons). Each surrogate piston is a 5.08-cm-long section of 8.25-cm-diameter aluminum alloy tubing. The surrogate pistons are mounted lengthwise in pairs with a thin aluminum cap on each end. Fig. 6 shows a schematic of the arrangement. The cylinders can be packed tightly in the racks because only the sides need to be treated. The cylinder pairs are separated horizontally by 0.75-cm gaps, and vertically by ~1.1 cm of support structure and copper cooling lines. The total exposed area is over 16 m^2. The racks are spaced 25 cm apart and centered in a cylindrical vacuum chamber that is 1.5 m in diameter and 4.6 m long. The racks are supported by ceramic insulators and are connected to the high-voltage feedthrough by a manifold constructed from stainless steel tubing. A cooling fluid runs through the target assembly to remove energy deposited by the implantation process and limit the target's temperature excursion.
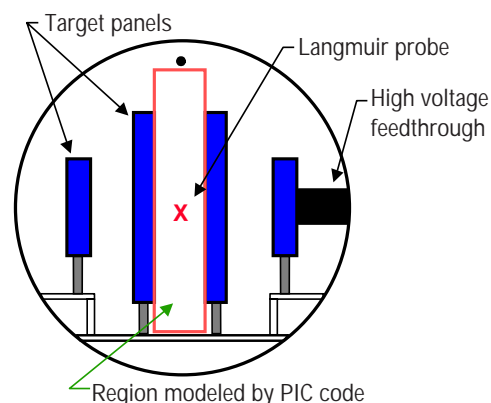
Fig. 6 Schematic of the piston surrogate assembly, vacuum chamber, and Langmuir probe insertion position (shown by an "X" in the figure).
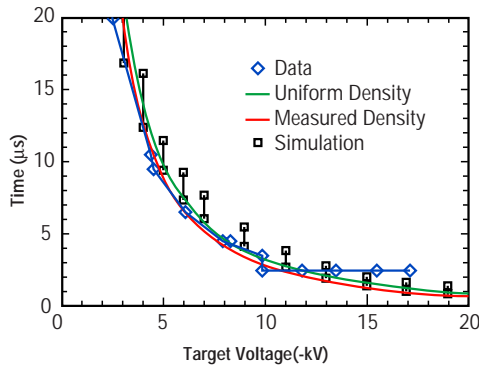
Fig. 7 Sheath overlap times between the racks of pistons as a function of target voltage. The blue data points were measured with the center probe tip. The green line is from the Lieberman theory for uniform density plasma, and the red line is for a parabolic density profile. The black squares are from the simulation, showing the finite time for the electron density to drop to zero.

To produce the background plasma, two 3×350-cm stainless steel radio frequency (RF) antennas are situated ~20 cm from the top of the vacuum chamber. One is centered and the other is displaced approximately 30° from vertical. A separate 1000-W, 13.56-MHz RF generator and matching network drives each antenna. The two RF generators are phase-locked, and are operated at the same power output setting. Driving the antennas creates a capacitive RF discharge of density n~10^8 to 10^9 cm^{-3}, with an estimated electron temperature, T_e, of ~3 eV.[13] The electron distribution is not expected to be entirely Maxwellian, and probably contains a high energy tail.[21] In conventional systems, methane (CH_4) is typically used as a working gas during the ion implantation step of making a diamond-like-carbon coating.[10] However, we used argon as the working gas to reduce complications from multiple ionic species and time-dependent surface conditions of Langmuir probe tips. Argon fill pressures used in these experiments ranged from 20 to 65 mPa.

A Langmuir probe assembly was inserted axially into the vacuum chamber and positioned between the two center racks (Fig. 6). The probe assembly was used to monitor basic plasma parameters, primarily plasma density, floating potential, and indications of plasma fluctuations. The probe was also used to determine the spatial characteristics of the plasma sheath expansion within the target assembly. To clarify the experimental results, the central portion of the target assembly was modeled using a two dimensional particle-in-cell (PIC) computer code (XPDP2, obtained from the Plasma Theory and Simulation Group at the University of California in Berkeley). The experimental configuration and modeling efforts are described in detail in two recent publications[22,23] and are summarized below.

In the interior portion of the assembly, the target racks appear essentially as quasi-planar structures and generate roughly planar plasma sheaths. If plasma density, applied target voltage, and voltage pulse duration are in the appropriate range (moderate plasma density, applied target voltages above a few kV, and pulse durations in excess of a few microseconds), these sheaths expand outward from the target racks and collide with each other on the planes dividing the racks. Measurements obtained from the Langmuir probe assembly allow a direct determination of the sheath overlap time (referenced to the start of the voltage pulse) for various experimental conditions. These measurements have been compared with sheath overlap times calculated from simple analytic theory, from a modification of the standard analytic theory to account for the measured variation of the plasma density in the sheath expansion region, and from results of the numerical PIC code. The comparison of these results is shown in Fig. 7. In general, the agreement is fairly good for the set of conditions of this measurement set. These conditions, however, minimize the impact of the secondary electrons on the background plasma and sheath propagation characteristics.

The strong interaction of the secondary electrons, target assembly, and background plasma appears in the form of two

different instabilities. The first, the "hollow cathode" instability, operates in much the same way as a hollow cathode discharge. Secondary electrons are temporarily trapped in the potential well between the racks of pistons, and directly ionize the background gas. The cross-section for ionization is enhanced by a reduction in the kinetic energy of the secondaries due to the overlap of the sheaths from adjacent racks of pistons so that this instability has significant impact only at low plasma densities and relatively high gas pressures. Furthermore, it occurs only if the secondary electron flux is sufficiently high. In experiments where a layer of graphite on the racks of pistons reduced the secondary electron emission coefficient, the instability was not observed until the graphite was sputtered off of the pistons. The hollow cathode instability effects are shown in Fig. 8.
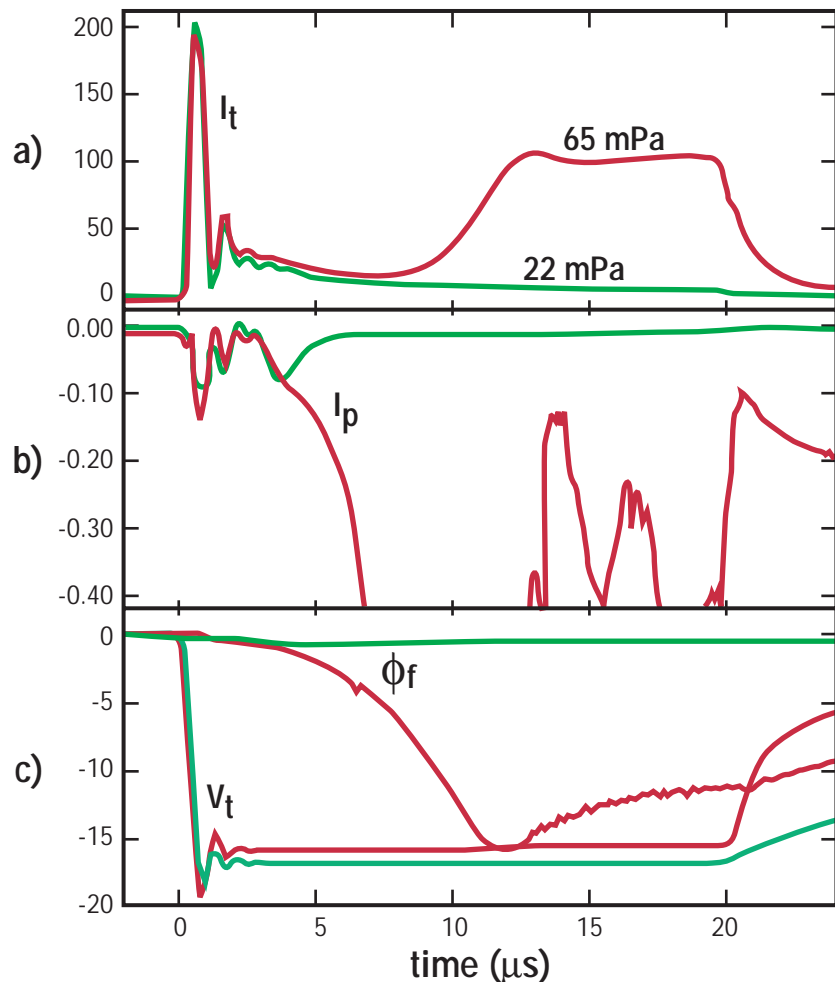

Fig. 8 Measurements of the (a) target current, I_t; (b) probe current, I_p; and (c) probe floating potential, ϕ_f, and target voltage, V_t, during the hollow cathode instability for 100 W of radio-frequency power. Negative currents signify the collection of electrons. The instability appears at 65 mPa fill pressure (red lines) but not at 22 mPa (green lines).

The second interaction mechanism is a beam-plasma instability, where the secondary electrons resonantly excite plasma waves. The energy in the plasma waves is transferred to the bulk plasma through Landau damping, causing an increase in the electron temperature and thereby an increase in the ionization rate. (A similar concept has been patented, but no experimental results have been published.) Unlike the hollow cathode instability, the beam-plasma instability requires a relatively large initial density. If the initial density is sufficiently large, the energy of the secondary electrons can be transferred to the bulk electrons before sheath overlap. The subsequent ionization of the background gas is then so rapid that the sheath motion is halted, preventing the sheaths from overlapping. A relatively high neutral gas pressure and a large flux of secondary electrons are also requirements for this instability to take hold. Impact of beam instability is illustrated in Fig. 9.

Fig. 9 Measurements of the (a) target current, I_t; (b) probe current, I_p; and (c) target voltage, V_t, during the beam-plasma instability for 1,800 W of radio-frequency power and a gas pressure of 65 mPa. Negative currents signify the collection of electrons. The instability appears after sputter cleaning has increased the secondary electron flux (blue lines) but not before (red lines).
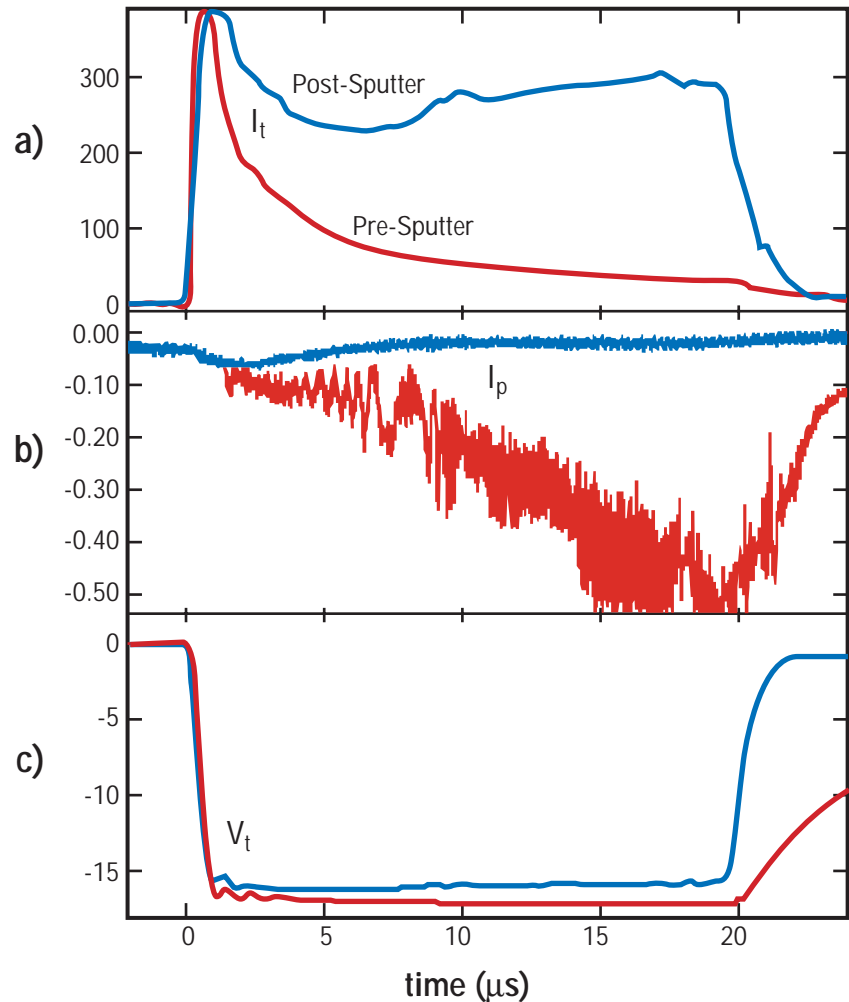
Conclusions

Successful commercial application of PSII depends on the ability to appropriately implant target components in a wide range of geometric configurations, particularly those in which the components have been relatively densely packed into a processing chamber. In our experiment, we explored the plasma sheath and plasma-target interaction characteristics within such a complex target assembly. This study yielded the first experimental demonstration of several important interaction mechanisms which are driven in the geometrically complex PSII system by the presence of energetic secondary electrons generated at the target surface by the implanted ions. Understanding these interactions will significantly increase our ability to predict the behavior of complex targets, and optimize target configurations for commercial application of PSII technology.

References

[1] R. J. Adler and S. T. Picraux, "Repetitively Pulsed Metal-Ion Beams for Ion Implantation," *Nuclear Instruments and Methods in Physics Research B* 6, 123 (1985).

[2] J. R. Conrad and K. Sridharan (Eds.), "Papers from the First International Workshop on Plasma-Based Ion Implantation: August 4–6, 1993, University of Wisconsin," *Journal of Vacuum Science and Technology B* 12, 813 (1994).

[3] G. A. Collins (Ed.), "Proceedings of the Second International Workshop on Plasma-Based Ion Implantation, Sydney, Australia, February 12-15, 1995," *Surface Coatings and Technology* 85, 28 (1996).

[4] J. R. Conrad, "Sheath Thickness and Potential Profiles of Ion-Matrix Sheaths for Cylindrical and Spherical Electrodes," *Journal of Applied Physics* 62, 777 (1987).

[5] J. R. Conrad, J. L. Radtke, R. A. Dodd, F. J. Worzla, and N. C. Tran, "Plasma Source Ion Implantation Technique for Surface Modification of Materials," *Journal of Applied Physics* 62, 4591 (1987).

[6] J. R. Conrad, "Method and Apparatus for Plasma Source Ion Implantation," U.S. Patent No. 4,764,394 (August 16, 1988).

[7] J. R. Conrad, "Plasma Source Ion Implantation: A New Approach to Ion-Beam Modification of Materials," *Materials Science and Engineering A* 116, 197 (1989).

[8] D. J. Rej and R. B. Alexander, "Cost Estimates for Commercial Plasma Source Ion Implantation," *Journal of Vacuum Science and Technology B* 12, 2380 (1994).

[9] D. J. Rej, "Plasma Source Ion Implantation," in M. Nastasi and J. W. Mayer (eds.), *Ion-Solid Interactions: Fundamentals and Applications*, Vol. I (Cambridge University Press, New York, 1996), p. 467.

[10] C. P. Munson, R. J. Faehl, F. Henins, M. Nastasi, W. A. Reass, D. J. Rej, J. T. Scheuer, K. C. Walter, and B. P. Wood, "Recent Advances in Plasma Source Ion Implantation at Los Alamos National Laboratory," *Surface and Coatings Technology* 84, 528 (1996).

[11] R. B. Alexander, "Using Ion Implantation to Improve Forming-Tool Life," *The Fabricator* 11, 1 (1992).

[12] A. Chen, J. T. Scheuer, C. Ritter, R. B. Alexander, and J. R. Conrad, "Comparison between Conventional and Plasma Source Ion-Implanted Femoral Knee Components," *Journal of Applied Physics* 70, 6757 (1991).

[13] M. A. Lieberman and A. J. Lichtenberg, *Principles of Plasma Discharges and Materials Processing* (Wiley-Interscience, New York, 1994).

[14] S. B. J. Charter, L. R. Thompson, and G. Dearnaley, "The Commercial Development of Ion Implantation for Steel and Carbide Tools," *Thin Solid Films* 84, 355 (1981).

[15] F. A. Smidt and D. B. Sartwell, "Manufacturing Technology Program to Develop a Production Ion Implantation Facility for Processing Bearings and Tools," *Nuclear Instruments and Methods in Physics Research B* 6, 70 (1985).

[16] J. R. Treglio, A. J. Perry, and R. J. Stinner, "Economics of Metal Ion Implantation," in *Proceedings of the Eighth International Conference on Surface Modification of Metals by Ion Beams* (September 1993, Kanazawa, Japan) *Surface and Coatings Technology* 65, 184 (1994).

[17] J. T. Scheuer, M. Shamim, and J. R. Conrad, "Model of Plasma Source Ion Implantation in Planar, Cylindrical, and Spherical Geometries," *Journal of Applied Physics* 67, 1241 (1990).

[18] J. G. Andrews and R. H. Varley, "Sheath Growth in a Low-Pressure Plasma," *Physics of Fluids* 14, 339 (1971).

[19] B. P. Wood, "Displacement Current and Multiple-Pulse Effects in Plasma Source Ion Implantation," *Journal of Applied Physics* 73, 4770 (1993).

[20] M. Shamim, J. T. Scheuer, R. P. Fetherston, and J. R. Conrad, "Measurement of Electron Emission due to Energetic Ion Bombardment in Plasma Source Ion Implantation," *Journal of Applied Physics* 70, 4756 (1991).

[21] V. A. Godyak, R. B. Piejak, and B. M. Alexandrovich, "Probe Diagnostics of Non-Maxwellian Plasmas," *Journal of Applied Physics* 73, 3657 (1993).

[22] B. P. Cluggish and C. P. Munson, "Sheath Overlap During Very Large-Scale Plasma Source Ion Implantation," *Journal of Applied Physics* 84, 5937 (1998).

[23] B. P. Cluggish and C. P. Munson, "Secondary-Electron Enhanced Discharges in Plasma Source Ion Implantation," *Journal of Applied Physics* 84, 5945 (1998).

Convergent Hydrodynamics of Inertial Confinement Fusion Implosions

C. W. Barnes, J. A. Oertel, and R. G. Watt (P-24);
R. E. Chrien (P-22);
J. B. Beck, N. D. Delamater, and D. L. Tubbs (X-TA);
N. M. Hoffman (X-CI);
H. Bush, R. D. Day, S. Dropinski, J. Duke, P. Gobby, V. Gomez, D. Hatch, R. Manzanares, J. Moore, and G. Rivera, (MST-6 and MST-7);
M. J. Edwards, W. W. Hsing, J. D. Colvin, O. L. Landen, and B. A. Hammel (Lawrence Livermore National Laboratory);
C. J. Keane (DOE);
D. Galmiche and A. Richard (DRIF/CEA, France);
M. Dunne, P. Graham, S. Rothman, and B. Thomas (AWE, United Kingdom);
T. R. Boehly, D. K. Bradley, P. Jaanimagi, and J. P. Knauer (Laboratory for Laser Energetics, University of Rochester);
D. Haynes and C. Hooper (University of Florida);
S. A. Voss (University of New Mexico); and
N. A. Shambo (North Carolina State University)

Introduction

The National Ignition Facility[1] (NIF), a large laser presently under construction at the Lawrence Livermore National Laboratory, is designed to produce 1.8 MJ of 0.35-µm light in a 500-TW pulse for defense applications and inertial fusion ignition. Although fundamental questions about the feasibility of achieving high gain in inertial fusion capsule implosions were settled a decade ago in a series of underground experiments at the Nevada Test Site, it remains a major scientific and technical challenge to obtain capsule ignition and gain in the laboratory with the laser energy and power available at the NIF.

Inertial fusion ignition and gain requires that a fuel region with enough size and density be heated to a high temperature such that fusion burn can be transiently sustained by energy deposited by the charged fusion reaction products. Ignition is easiest to obtain using a deuterium-tritium fuel mixture, and for this fuel the requirements are a temperature of about 20 keV and a density-radius product of a few g/cm^2. Rather than producing these conditions in a uniform volume (which would require a laser energy on the order of 100 MJ), the mainline capsule design for the NIF employs a concept known as "hot-spot" ignition. In this concept, a small fraction of the fuel mass is ignited in a central hot spot, and then a thermonuclear burn wave propagates outward into the surrounding compressed fuel to produce a significant fusion yield.[1]

Hydrodynamic perturbation growth during the capsule implosion plays a major role in determining whether the hot spot in the fuel can ignite. Hydrodynamic instabilities pose a threat to ignition by creating spikes of cold fuel that penetrate into the hot spot and increase thermal losses from this region. The energy required to ignite a capsule increases as shell thickness increases, and the minimum acceptable shell thickness depends on the magnitude of the perturbation growth that would disrupt the shell. Hydrodynamic instabilities can also reduce the efficiency with which the kinetic energy of the imploding shell (or "pusher") is converted to temperature of the hot spot and reduce the overall compression of the fuel. Another mechanism that could affect ignition is the introduction of contaminants from the shell into the fuel (a process known as "mix") and subsequent radiative energy loss.

Perturbations occur because of nonuniformities in the radiation drive on the shell or fuel surface. During the ablative acceleration phase, perturbations at the ablation front grow via the Rayleigh-Taylor instability, whereby the lower-density ablated material accelerates the higher-density unablated shell. These perturbations are transferred or "fed through" to the inner surface of the shell, where they can further grow during the convergence and deceleration phases (see Fig. 1). These inner surface perturbations cause mix of the cold ablator with the hot fuel, either preventing ignition or, conversely, increasing the size of the driver required to achieve a fixed gain.

Because the Rayleigh-Taylor instability at the ablation front is expected to be the dominant effect for inertial confinement fusion (ICF) implosions, there has been much effort devoted to theoretical development and measurement of the instability under ICF-relevant

conditions. However, few experiments have explored the effects of ablatively driven Rayleigh-Taylor growth in convergent geometries. Calculations of the hydrodynamic performance of ignition capsules[2] for the NIF need to be validated by present-day experiments. To address this issue, the Laboratory's ICF Program has launched two campaigns to explore the growth of hydrodynamic instabilities in cylindrical and spherical geometries. This research highlight describes each of these research efforts with an overview of the results.

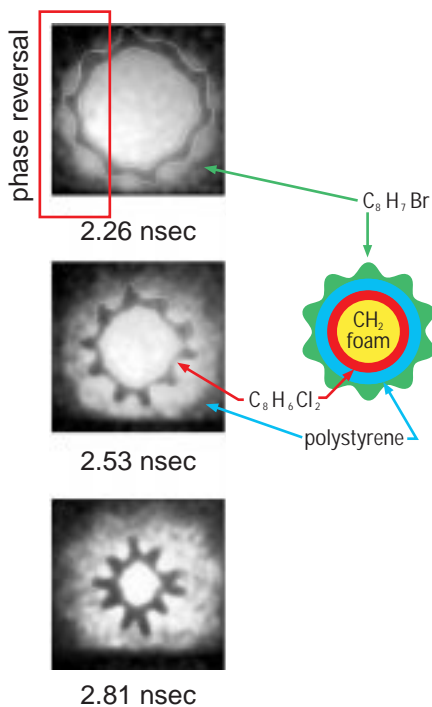## Cylindrical Implosion Research on the Ablative Rayleigh-Taylor Instability

Cylindrical implosions can provide physical insight into convergent hydrodynamics issues because cylindrical geometry allows for excellent diagnostic access along a line of sight and provides a good match to present two-dimensional (2-D) simulation codes. By contrast, in a spherical implosion along any diagnostic line of sight, material is moving towards, away from, and across the diagnostic. Unfolding the radial dependence of the implosion from such line-integrated observations is difficult. Thus, spherical implosion experiments usually rely on "integrated" measurements of the performance of the implosion. In a cylindrical implosion, the diagnostic view along the cylindrical axis only has material moving at right angles to the field of view and the radial unfolding of the information is straightforward. With proper design of the axial implosion, the experiment can be kept relatively 2-D and thus tractable for detailed comparison to present-generation simulation codes. Convergent effects are not as strong in a cylindrical implosion (only increasing as $1/R$ and not $1/R^2$ as in a spherical implosion), but those effects can still be effectively studied.

Our early research focussed on cylindrical implosions using indirect-drive at Livermore's Nova laser.[2,3] Experiments were conducted using a cylinder that extended transversely across the entire diameter of a Nova hohlraum, which was driven using eight Nova beams with a total energy of 22–25 kJ (Fig. 2). The eight beams were arranged symmetrically around the cylinder in the hohlraum to provide the best possible drive symmetry although there still was an initial m = 4 azimuthal variation of illumination. The implosions were radiographed axially using a gated x-ray pinhole imaging system and a silver or titanium backlighter foil on the far side.
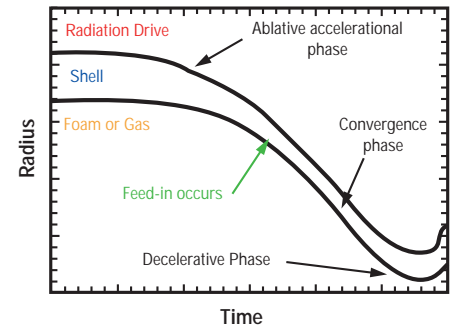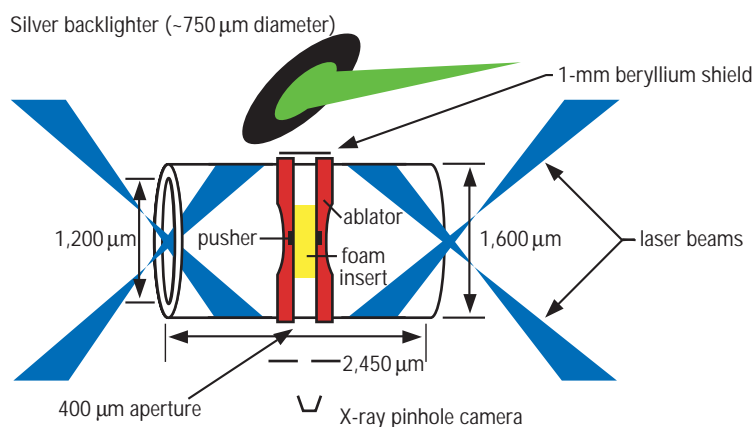
Fig. 1 *Phases of hydrodynamic instability during an implosion. Perturbations on the outside of the shell are fed through to the inner surface, where they grow as the implosion progresses.*

Fig. 2 *Experimental design for an indirect-drive experiment on Nova. The cylinder is mounted transversely across the diameter of the hohlraum. Eight laser beams are arranged symmetrically around the cylinder and drive its implosion with an energy of 22–25 kJ. The x-ray pinhole imaging system (which includes the backlighter, beryllium shield, aperture, and pinhole camera) provides axial radiographs of the imploding cylinder.*

Fig. 3 *Sequence of gated x-ray framing camera images from an indirectly-driven cylindrical implosion at Nova. The dark, convoluted region comes from feed-in of perturbations growing at the ablation surface to a marker region of chlorinated plastic. The dark region at the outside is ablated brominated plastic. The lighter area between these layers is the polystyrene ablator. (Diagram of layers is not to scale.)*

The cylinder design primarily used in these experiments had a 472-μm outer diameter, and it comprised a brominated polystyrene ablator over a plain polystyrene pusher with a 60-mg/cc, 430-μm-inner-diameter, polystyrene foam insert. The cylinder was shielded by gold coating at its ends and was tapered along its length so that only an approximate 300-μm waist region imploded. The axial length was further defined by a thin, 160-μm-long chlorinated polystyrene marker layer between the pusher and the foam; however, further tests have confirmed that most of the radiographic contrast comes from radial densification of the implosion and not from the opacity of the chlorinated marker. Perturbations were machined azimuthally on the outside of the ablator.[4]

A sequence of over 20 targets was shot at Nova with nearly identical conditions. Only the azimuthal mode number (either m = 10 or m = 14) or amplitude (unperturbed, 0.25, 0.5, 1.0, 1.5, 3.0, and 5.0 μm) of the machined perturbation varied. (The mode number is the number of perturbation wavelengths around the circumference of the cylinder.) An example of the sequence of data provided from a single shot is shown in Fig. 3. These experiments provided valuable data for all three phases of instability growth during cylindrical implosions. There is a clear indication of phase reversal at the ablation surface (the outer dark region).

The first phase of the implosion consists of initial ablative Rayleigh-Taylor instability growth at the ablation front, in which the perturbations feed into the marker region (which has a higher compressed density at the plastic-foam interface). The ratio of the final measured perturbation amplitude and initial machined perturbation amplitude is the measured growth factor. In these initial indirect-drive experiments, the acceleration tended to occur only while the convergence ratio was less than about 1.5. The measurements of instability growth occur at or after the time this convergence is reached. Hence the ablative Rayleigh-Taylor instability growth sets the initial amplitude observed in the experiment. Our experiments confirm the expectation that the mode m = 14 grows faster and to higher amplitude than the m = 10. Perturbations with initial amplitude 1.5 μm or less remained linear during the ablative Rayleigh-Taylor phase, and the growth factors for the same mode number were the same during the entire implosion. Detailed time-dependent measurements of mode amplitudes can then be compared to hydrodynamic simulations. A post-processing code is used to simulate the x-ray radiographs from calculations with LASNEX, a 2-D radiation hydrodynamics code, using the same filtering and analysis as done in the experimental data reduction (see Fig. 4).

In the second phase, convergence, the perturbations continue to grow even in the absence of acceleration. This "crenulation" effect, first identified by Bell[5] and Plesset[6], is a feature of all convergent implosions that act incompressibly. For a ring or shell of material to maintain its volume as it converges, it must thicken and its wrinkles must grow. In our experiments, all of the perturbations appeared to grow at the same rate regardless of size, even when the perturbations exceeded usual "nonlinearity conditions" (*e.g.*, even when the amplitude was a

significant fraction of the wavelength or radius). The largest initial amplitude perturbations did show signs of saturation in their growth, but not until they reached amplitudes divided by wavelength of nearly unity! Examples of the different nonlinear shapes that result from starting with increasing initial amplitude are shown in Fig. 5. These nonlinear effects were studied in detail using a target with the largest initial amplitude yet tried, an m = 10, 5-μm perturbation. This amplitude was chosen to go nonlinear during the ablative Rayleigh-Taylor phase. Several features are seen in these images. First, the rod-like spikes grew steeper and, for the first time in these experiments, developed observable harmonics of the fundamental. The image also shows that, late in time, the spikes "crush in" from the compressibility effects of Bell-Plesset growth.

During these first two phases of the implosion, there is second-order, weakly nonlinear mode coupling between the machined perturbations and the m = 4 illumination asymmetry caused by the eight laser beams in the hohlraum. This leads to m = 10 + 4 = 14 and m = 10 - 4 = 6 modes with phases and amplitudes that appear consistent (within factors of two) with theory[7] when derived for convergent geometry. This mode coupling creates the "lumpy" look of the data, which is not noise, but actually an important feature of the physics.

In the third phase, deceleration, there is expected to be Rayleigh-Taylor growth at the unstable pusher-foam interface. However, three-dimensional (3-D) end effects in the target design made the interface inside the marker layer diffuse and such effects were not seen. At the outside of the marker layer, compressibility effects[3] reduced the size of the perturbations.

To improve upon the Nova experiments, we collaborated with scientists from the University of Rochester on a series of experiments to study convergent hydrodynamics using direct-drive illumination at the Laboratory of Laser Energetics Omega facility.[8] The use of direct-drive illumination couples more energy into an implosion (perhaps 10 kJ out of 18 kJ of ultraviolet laser light instead of 3 kJ from the

(a)

(b)
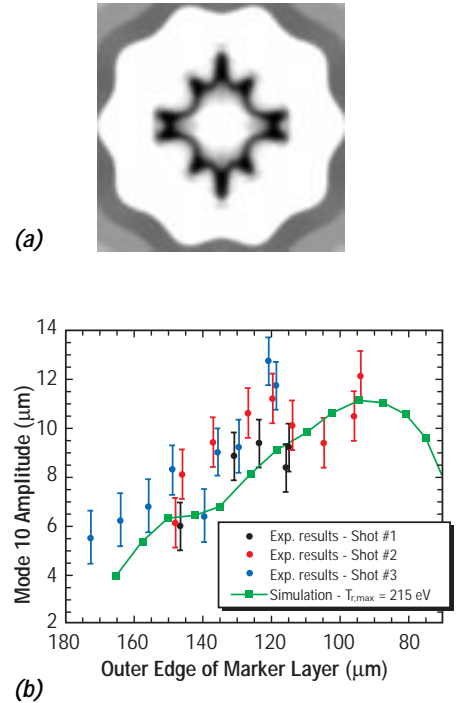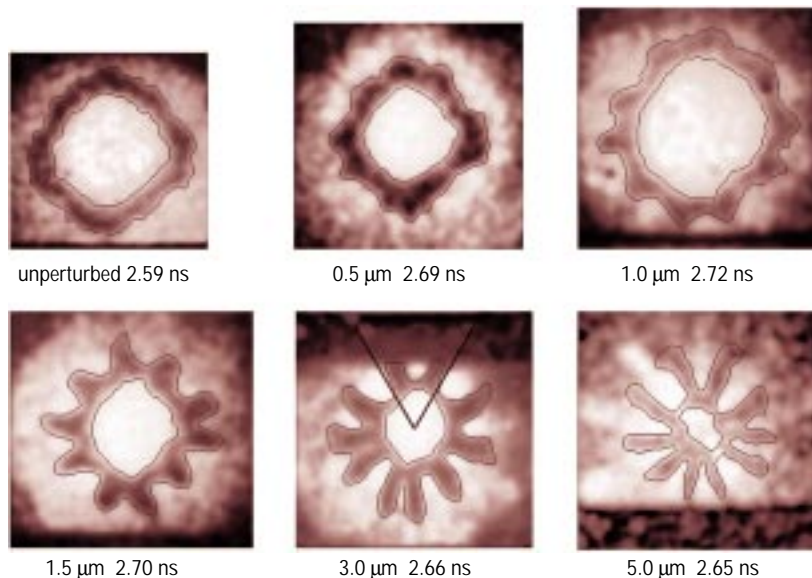
Fig. 4 *Post-processed simulation of an axial x-ray radiograph generated from a hydrodynamic simulation of an indirect-drive cylindrical implosion on Nova (the image includes m = 4 illumination asymmetry). (b) Comparison of simulated amplitude and experimental measurements from m=10, 1-μm initial amplitude perturbations. The simulations fit well with the experimental results.*

unperturbed 2.59 ns   0.5 μm 2.69 ns   1.0 μm 2.72 ns

1.5 μm 2.70 ns   3.0 μm 2.66 ns   5.0 μm 2.65 ns

Fig. 5 *Images at similar times (and hence radii) of cylindrical implosions, starting from different initial perturbation amplitudes. Varying the starting amplitude produces widely different nonlinear shapes.*

Fig. 6 *Photograph of the cylinder used in direct-drive experiments on Omega. The cylinder is aligned along the diagnostic axis and includes components of the imaging system (axial backlighter, leaded acrylic aperture, and various alignment fibers).*
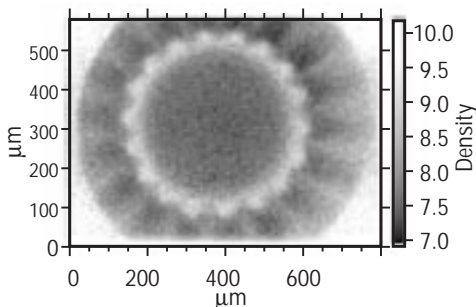
Fig. 7 *X-ray radiograph from a "feed-out" test using direct-drive cylindrical implosion on Omega. The experiment used a cylinder with m = 18, 1.5-µm amplitude perturbations on the interior surface of the ablator. These perturbations "fed-out" to the ablation front and grew as the implosion progressed.*

indirect-drive x-ray radiation for a similar amount of ultraviolet laser energy). Thus, we were able to implode cylinders that were twice as large as the ones used in the Nova experiments with corresponding increases in convergence ratio at maximum acceleration (2.5 instead of 1.5), growth factors (30 instead of 15), and resolution (nearly twice the pixel resolution elements at the same convergence). Using direct drive advances in smooth beam illumination (distributed phase plates and smoothing by spectral dispersion) we achieved generally more symmetric implosions with less mode coupling as well.[9]

The cylinders used in the Omega experiments (see Fig. 6) were unique because of their thin-wall construction. With an inside diameter of 860 µm and a wall of 20 µm, these polystyrene cylinders were particularly fragile. To ensure their survival, the polystyrene-coated mandrels were annealed three times prior to final mandrel removal. The outer surface of the cylinders was machined with azimuthal modes varying with m = 14, 28, 38, or 58, with amplitudes from 0.5 to 1 µm. The 2.25-mm-long plastic cylinders were coated with 500 Å of aluminum that served as a shine shield to provide uniform plasma breakdown. They were filled with 60 mg/cc polystyrene foam; some targets had the foam doped with deuterium or chlorine to enhance neutron or spectroscopic diagnostic measurements. Extensive metrology of the completed targets (measuring angles to within 0.1° and position to within a few µm) ensured that the Omega beams provided the illumination required and that all of the beams hit the target.

During the Omega experiments, 50 laser beams were focussed around a central band of the cylindrical target. Very symmetric implosions were achieved with convergence ratios of seven for the shell and 10 for the hot spot or axial emission spike. Twenty-two shots were obtained in this first scoping campaign, including 17 implosions, 15 of which had both excellent energy and power balance. Thirty-four shots were obtained in the second campaign including 28 implosions scoping out a variety of experimental and theoretical issues. On each shot, five to eight of the remaining laser beams were focussed on titanium backlighters. X-ray radiography was performed both axially and transverse to the cylinder axis to produce excellent sets of gated framing camera images of the hydrodynamics of the cylinder imploding.[10] Results from one experiment are shown in Fig. 7. In addition, framing and streaked images and time-resolved x-ray spectroscopy were used to explore the behavior of these targets.

During this campaign, we modified two of the target cylinders to allow for study of perturbations on the interior surface. The image in Fig. 7 shows an x-ray radiograph from this experiment. Perturbations with m = 18 and 1.5 µm amplitude were put on the inside surface of the ablator at the foam interface. The results from these interior perturbation experiments can be used to study the "feed-out" problem associated with the Rayleigh-Taylor instability.[11] In this process, the initial shock driven through the ablator reflects off the rippled surface at the inside and bounces back to the ablation front where it seeds instability growth there.

Detailed analysis of these experiments and design for future campaigns continues, now in additional collaboration with researchers from the Atomic Weapons Research Establishment in the United Kingdom and from the University of Florida. These results are providing high quality data useful for validation of complex hydrodynamic calculations such as those used to predict ignition at the NIF.[12] Figure 8 shows comparisons of measured mode amplitude with LASNEX simulations, showing disagreement late in the acceleration history with the predicted mode growth. Current work concentrates on understanding and ameliorating the effects of short-wavelength laser nonuniformities on the perturbation growth; measuring the "thermodynamics" of the cylindrical implosions by spectroscopic or neutronic methods for comparison to the observed hydrodynamics; and observing mix and defect evolution at the inside interface of the ablator.

Spherical Capsule Implosions using a Deuterated Layer

While experiments such as those described above provide useful information about perturbation growth, ignition capsules designed for the NIF are, in general, much more unstable than cylindrical (and most spherical) implosions studied in Nova and Omega experiments. In the absence of nonlinear effects that reduce the perturbation growth rate, the spikes of cold pusher material penetrating into the hot-spot region of these NIF capsules are predicted to be ~400-times larger than the initial perturbations on the capsule surfaces (this is known as the linear growth factor). Fortunately, nonlinear processes reduce the perturbation growth and thus the size of the spikes. In order to test the ability of our computer simulations to predict the *actual* levels of perturbation growth in NIF capsules, a series of spherical capsule implosions on Nova was designed to maximize the perturbation growth and produce linear growth factors at levels as close as possible to those expected in ignition capsules on NIF.

These high-growth Nova implosions, designed by Keane[13] and performed by Hammel and Landen[14], enhanced the perturbation growth by using a germanium dopant in the pusher, producing linear growth factors of ~100. The main diagnostic of capsule performance was the neutron yield from deuterium gas filling the capsule (Fig. 9a). In these Nova implosions, the three deleterious effects of perturbation growth (enhanced thermal losses, mix, and reduced compressional heating) all act to cool the deuterium fuel so that their relative

(a)

(b)
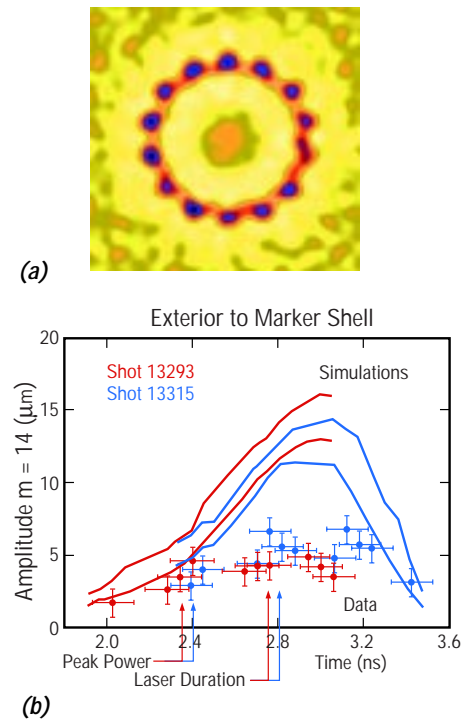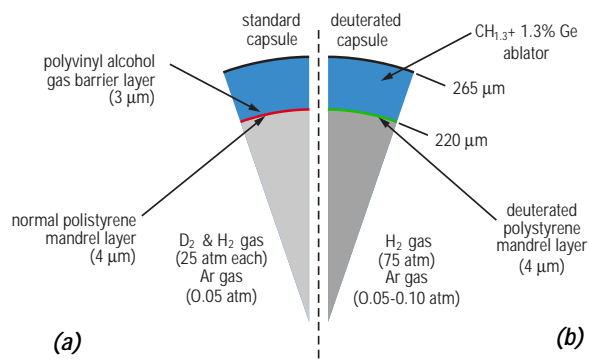
Fig. 8   (a) Post-processed simulation of an x-ray radiograph generated from a hydrodynamic calculation, including the effects of finite photon statistics. (b) Comparison of simulated and experimental measurements of mode and amplitude for an m = 14, 0.5-μm initial amplitude perturbation. The amplitude is measured at the interface exterior in radius to the chlorinated marker shell. There is disagreement in the predicted and actual mode growth late in the acceleration history.

(a)   *(b)*

Fig. 9   Pie diagram of the standard deuterium-filled capsule (a) and the hydrogen-filled deuterated-shell capsule (b). In (a) the neutron yield is produced in the compressed deuterium gas region, while in (b) it is produced in the deuterated inner layer of the pusher heated by thermal conduction from the nonreacting gas. Higher linear growth factors are produced in capsule (b), approaching the values calculated for NIF capsules.

importance cannot be separated through a neutron yield measurement. However, we realized that in capsules made with a deuterated inner layer and filled with nonreacting hydrogen gas (Fig. 9b), increased heat loss and atomic mix would both *increase* the temperature of the deuterated layer. These deuterated shell capsule implosions would be sensitive to the interface between the pusher and the gas, but relatively insensitive to the compressed gas region. As a result, deuterated shell implosions would provide an additional and qualitatively different constraint on simulations that would be complementary to the deuterium-filled, high-growth capsule implosions and would help to determine the relative importance of the effects of perturbation growth. A series of implosions using deuterated shell capsules was performed. As described below, these implosions reached linear growth factors of ~325, approaching those predicted for NIF capsules.

The capsules were imploded by indirect x-ray drive on the Nova[15] laser using a shaped, 2.2-ns-long laser pulse with 31 kJ of energy. The capsules were mounted in 2.40-mm-long, 1.65-mm-diameter pentagonal hohlraums. The laser pulse produced a peak radiation temperature of 232 eV in the hohlraum. As shown in Fig. 9b, the capsule shells included a germanium dopant to reduce preheat of the pusher and the gas by gold *M*-band x-rays from laser-plasma interactions at the hohlraum wall, steepen the density gradient at the ablation front, and reduce the ablation rate.[16] These effects increased the perturbation growth from hydrodynamic instabilities to values approaching those calculated for NIF capsules.

To study the effect of perturbation growth on capsule performance, we varied the surface roughness of the shells by laser ablation pitting.[17] The roughness was varied by adjusting the laser energy to control the depth of the pits, and the surface perturbations were measured by atomic force microscopy.[17] The power spectrum of the surface perturbations (Fig. 10) can be used as a starting point for hydrodynamic stability calculations. The most dangerous modes are

Fig. 10   One-dimensional power spectra for smooth and laser-roughened capsules, which can be used as a starting point for hydrodynamic stability calculations. Mode numbers below 10 have much slower predicted growth rates and are excluded from calculations by substituting the power in mode 10, as indicated by the dashed lines.
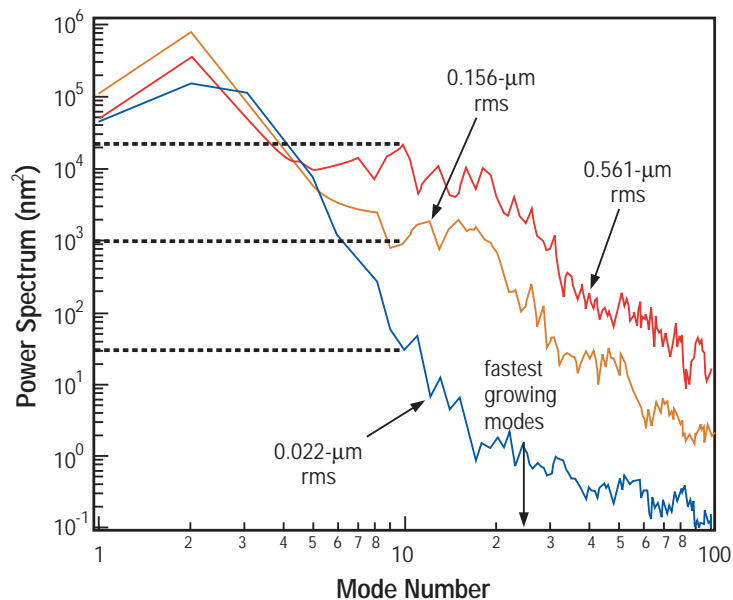
expected to be those with wavelengths similar to the capsule thickness. As a simple measure of the surface roughness, the power spectrum is also summed to obtain the surface variance and, from the square root of the variance, the root-mean-square (rms) surface roughness. Low mode numbers (below 10) have much slower calculated growth rates than modes in the range 10–30 and are excluded from the surface variance summation by substituting the power in mode 10 for the power in modes 1–9.

The observed dependence of yield on surface roughness is shown in Fig. 11. The neutron yields are obtained from Nova's Tion[18] and LaNSA[19] single-interaction neutron detector arrays located at 27 m and 20 m, respectively, from the target. The neutron yields are
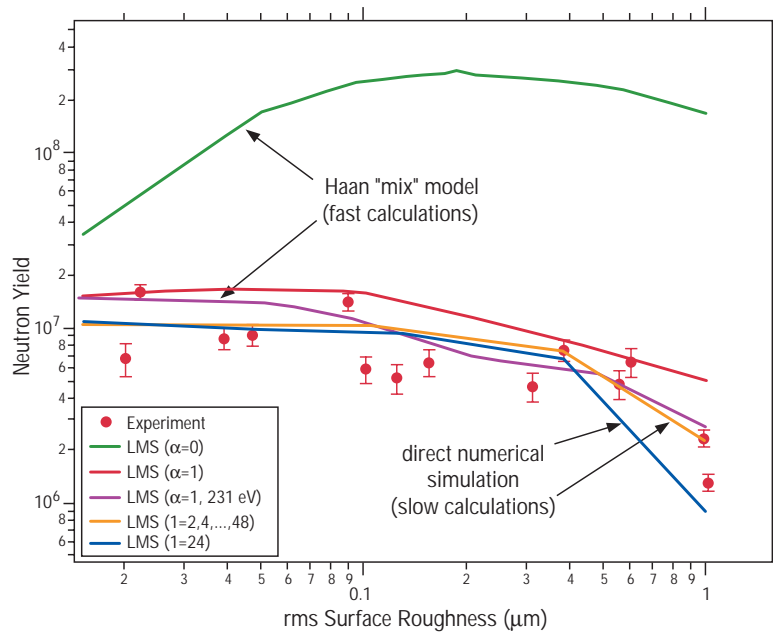

Fig. 11 Variation of measured and simulated (LMS and DNS) neutron yield with surface roughness. All experimental data points are from the Tion array except two points at 1-μm rms roughness from the LaNSA array. This table illustrates that the simulations fit well with the results except in the case of the LMS α = 0 simulation.

approximately constant for surface roughness up to 0.2 μm and decrease for rougher surfaces. X-ray images (in the 3–4 keV photon energy range) of 1-μm-roughness capsules at peak compression are distinctly larger and weaker than the images at other surface roughnesses (Fig. 12), suggesting that these shells have broken up
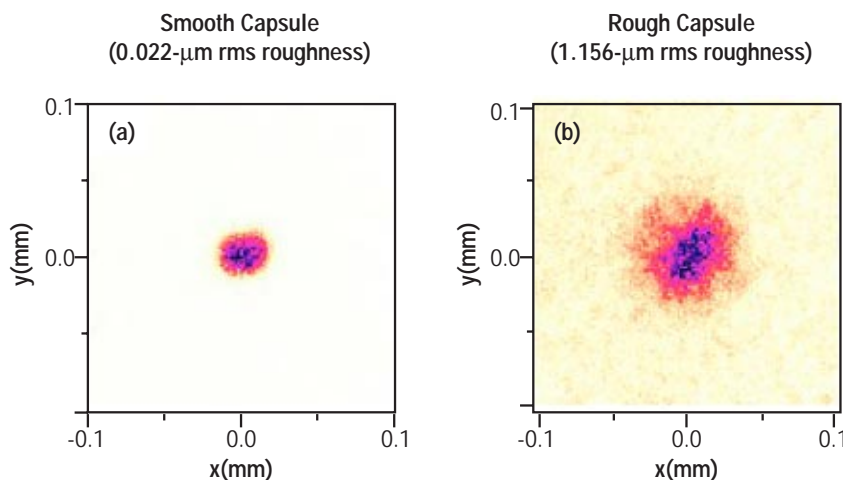

Fig. 12   Gated x-ray images of smooth and rough capsules at peak compression times. In general, capsules with roughnesses ≥1 μm produced larger, weaker images, suggesting that the capsules broke up during the implosion.

during the implosion. The image diameters at the 50% intensity contour for the smooth and 1-μm-roughness capsules are 25 ± 5 μm and 50 ± 10 μm, respectively. The neutron energy spectrum, summed over all the shots, had a full-width-at-half-maximum (FWHM) energy spread of 99 ± 6 keV. This energy spread, if caused solely by thermal motion of the deuterons[20], would correspond to an ion temperature $T_i = 1.43 \pm 0.17$ keV. However, the neutrons could also be subject to Doppler broadening from bulk fluid motion[21] during the time of neutron production as a result of the motion of the deuterated layer.

We performed two types of simulations of these implosions. The first type is known as direct numerical simulation (DNS).[22,23] It involves direct calculation of perturbation growth using the LASNEX[24] 2-D radiation hydrodynamics code, starting with a realistic mode spectrum and following the perturbations into the nonlinear regime. Neutron yield and other observables are calculated at the same time as the perturbation growth. The simulation involves no adjustable parameters associated with hydrodynamic instabilities, heat conductivity, or mode saturation. The simulations directly predict the nonlinear "bubble and spike" structures on the inner surface of the capsule which increase the inner surface area and thus heat loss from the gas. Furthermore, DNS explicitly predicts the reduction in compressional heating of the gas as a result of perturbation growth. For small rms roughness, the yield predictions of DNS are nearly independent of roughness and are the same whether they are started with a spectrum of 24 modes ($\ell = 2, 4, . . ., 48$) or with the same roughness in the dominant mode ($\ell = 24$). However, for large rms roughness (>0.4 μm), when the shell is beginning to break up, the single-mode $\ell = 24$ calculations predict a more rapid decrease in yield than the multimode calculations, as expected for the dominant mode.

Fig. 13 Variation of DNS calculations of peak compressional heating power (circles) and peak fusion-weighted ion temperature (squares) with capsule surface roughness.
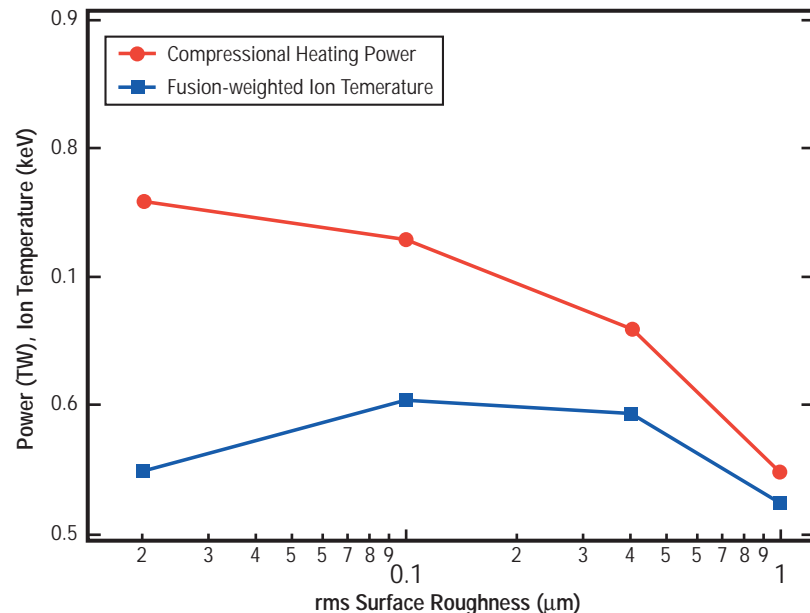
DNS predictions are in quantitative agreement with the measured yields (Fig. 11), and thus provide a confirmation of the method. Both single- and multi-mode DNS yields decrease slowly with surface roughness up to 0.4-μm and then begin to fall more rapidly. The most obvious effect of perturbation growth in DNS is a reduction in the peak compressional heating power. The decrease in compressional heating is partially compensated for by an increase in the temperature of the deuterium. This effect is manifested in DNS as an increase in the fusion-reaction-weighted ion temperature (Fig. 13). The increase in temperature from a smooth implosion to 0.1-μm roughness corresponds to a nearly two-fold increase in fusion reactivity, and is roughly balanced by a similar decrease in the average density of the deuterated layer. These simulations indicate fully developed turbulence and shell breakup for implosions with roughness greater than 0.4 μm, in agreement with the experiments.

DNS predictions for the x-ray image sizes are similar to the experimental observations. The diameter of the x-ray images in the 3–4 keV range at the time of peak emission is predicted to be 29 μm for smooth capsules, increasing to 33 μm for 0.4-μm-roughness and 43 μm for 1-μm-roughness capsules. The maximum intensity of the images is also predicted to decrease by a factor of two from the smooth to the roughest capsules, similar to the trend toward weaker images in the experiments.

The ion temperature inferred from the neutron spectra (1.4 keV) is higher than the DNS predictions and corresponds to a 200-times larger fusion reactivity. To reconcile the measured yields with this temperature, one would have to postulate a 200-fold reduction in the product of deuterium density, inventory, and burn duration. Any such explanation would be difficult to reconcile with simulations of other ICF implosions, which typically match the average measured yield within 30%. On the other hand, mass flows can increase the neutron energy spread without increasing the fusion reactivity. Neutron spectra calculated by post-processing the output of DNS calculations show the qualitative effect of broadening by mass flow, especially in the early part of the burn when spike speeds are largest. Quantitatively, however, the calculated mass-flow broadening integrated over the entire burn duration is insufficient to explain the observed spectral width. This discrepancy may indicate that significant mass-flow broadening occurs at scales too small to be resolved in the calculations, that the symmetry enforced in 2-D single-hemisphere calculations causes unrealistic stagnation of the flow, or that 3-D spikes in the experiment travel faster than 2-D spikes in the calculations. Neutron energy broadening from mass flow may also be important in other ICF experiments whenever deviations from spherical symmetry produce flows in the gas region with speeds approaching 1×10^7 cm/s during the fusion burn.

The second type of simulation, known as linear mode superposition and saturation (LMS), has been extensively applied to NIF capsule design.[25] It begins with a calculation using LASNEX of the linear growth rates of individual spherical harmonic modes (with infinitesimal amplitudes) seeded at the outer surface. The calculated

linear growth factors (ratios of final and initial mode amplitudes without any mode saturation) are largest for modes between 20 and 24, and reach ~325 at the time of peak neutron emission. The individual modes are superimposed, using the measured initial surface perturbations on the capsule and including a saturation criterion for the growth rate of each mode.[26] The procedure is used to predict the rms amplitude L of the perturbations at the gas-pusher interface throughout the implosion. An annulus of width L is assumed to be mixed on an atomic scale. Once the extent of the mixed region is known, the neutron yield is predicted in a separate one-dimensional (1-D) calculation. Since LMS simulations do not account for increased surface area in the mixed region, an enhancement to the usual electron thermal conductivity is applied in that region, with a diffusion coefficient having a form given by $\alpha L \dot{L}$ where α is an adjustable multiplier.

The LMS predictions of neutron yield are shown in Fig. 11 for two values of α. For comparison, the yield predicted in a clean 1-D simulation is 9.9×10^6. A large increase with increasing surface roughness, followed by a decrease, is predicted for the yield as the surface roughness increases when enhanced heat loss is not included ($\alpha = 0$). The yield is predicted to increase because the shell converges farther as gas effectively leaks into the shell via mix. Further mixing reduces the central temperature and hence the neutron yield. The prediction using $\alpha = 0$ is clearly inconsistent with the measurements. When enhanced heat loss is included ($\alpha = 1$), the predicted yield varies by less than a factor of three with surface roughness because the effects of mix and heat loss nearly balance each other. Calculations with larger values of α (up to 5) differ little from the $\alpha = 1$ predictions. The variation with roughness shows that the yield is insensitive to the extent of the mix region which, at the time of peak neutron emission, varies between 4-μm spike growth for smooth capsules and 19-μm spike growth for capsules with initial 0.5-μm rms roughness. This lack of sensitivity arises because, as deuterated shell material moves closer to the hotter capsule center due to increasing perturbation growth, it also conducts heat away more quickly, so the temperature in the mix region stays approximately constant. The yield measurements cannot, therefore, be used to distinguish between different ways of modeling nonlinear hydrodynamic perturbation growth (DNS *vs.* LMS). The results do, however, demonstrate the importance of including enhanced heat loss in LMS modeling and also illustrate the relative importance of competing effects in determining the physical conditions in the burn region. The yield is most sensitive to the temperature in the shell which is, as these results show, insensitive to perturbation growth. However, the temperature in the shell is very sensitive to the radiation drive, as illustrated by an LMS calculation with a peak drive temperature of 231 eV (Fig. 11). For peak drive temperatures of 231–233 eV, consistent with the experimental drive, the yields predicted by LMS are very close to those predicted by DNS and also in good agreement with the data (Fig. 11).

In conclusion, we have performed the first measurements and numerical simulations of fusion yield from the gas-pusher interface of

ICF implosions. The yields predicted by DNS are found to be in quantitative agreement with the measured yields, even in the highly nonlinear regime where shell breakup occurs, without using adjustable parameters for enhanced thermal losses or mix. These measurements also show that, in a mix model based on LMS and saturation, enhanced heat loss in the mixed region is essential to match the yields. The neutron energy spectrum shows enhanced broadening, most likely arising from bulk fluid motion of the deuterated layer. The sensitivity of these measurements to the gas-pusher interface helps to test capsule implosion simulations in a way that is not possible with conventional implosions, and thereby helps to validate the models used to design ignition capsules for the NIF laser.

References

[1] J. D. Lindl, "Development of the Indirect-Drive Approach to Inertial Confinement Fusion and the Target Physics Basis for Ignition and Gain," *Physics of Plasmas* 2, 3933 (1995).

[2] W. W. Hsing, C. W. Barnes, J. B. Beck, N. Hoffman, D. Galmiche, A. Richard, J. Edwards, P. Graham, S. Rothman, and B. Thomas, "Rayleigh-Taylor Instability Evolution in Ablatively Driven Cylindrical Implosions," *Physics of Plasmas* 4, 1832 (1997).

[3] W. W. Hsing and N. M. Hoffman, "Measurement of Feedthrough and Instability Growth in Radiation-Driven Cylindrical Implosions," *Physical Review Letters* 78, 876 (1997).

[4] P. L. Gobby, L. J. Salzer, R. D. Day, J. J. Bartos, Jr., G. Rivera, D. J. Hatch, F. P. Garcia, R. Manzanares, L. R. Foreman, and H. Bush, Jr., "Micromachining of Inertial Confinement Fusion Targets," *Nuclear Instruments and Methods for Physics Research A* 397 (1997) 183.

[5] G. I. Bell, "Taylor Instability on Cylinders and Spheres in the Small Amplitude Approximation," Los Alamos National Laboratory Technical Report LA-1321, Los Alamos Scientific Laboratory (1951).

[6] M. S. Plesset, "On the Stability of Fluid Flows with Spherical Symmetry," *Journal of Applied Physics* 25, 96 (1954).

[7] S. W. Haan, "Weakly Nonlinear Hydrodynamic Instabilities in Inertial Fusion," *Physics of Fluids B* 3, 2349 (1991).

[8] Cris W. Barnes, D. L. Tubbs, J. B. Beck, N. M. Hoffman, K. A. Klare, J. A. Oertel, R. G. Watt, T. R. Boehly, D. K. Bradley, and J. P. Knauer, "Experimental Configuration of Direct Drive Cylindrical Implosions on the OMEGA Laser," *Review of Scientific Instruments* 70, 476 (1999).

[9] D. L. Tubbs, C. W. Barnes, J. B. Beck, N. M. Hoffman, J. A. Oertel, R. G. Watt, T. Boehly, D. Bradley, and J. Knauer, "Direct Drive Cylindrical Implosion Experiments: Simulations and Data," *Lasers and Particle Beams* (to be published in 1999).

[10] Sarah A. Voss, C. W. Barnes, J. A. Oertel, R. G. Watt, T. R. Boehly, D. K. Bradley, J. P. Knauer, and G. Pien, "Gated X-Ray Framing Camera Image of a Direct-Drive Cylindrical Implosion," *IEEE Transactions on Plasma Science Triannual Issue on Images in Plasma Science* (to be published in 1999).

[11] D. P. Smitherman, R. E. Chrien, N. M . Hoffman, and G. R. Magelssen, "The Feed-out Process: Rayleigh-Taylor and Richtmyer-Meshkov Instabilities in Uniform, Radiation-Driven Foils," *Physics of Plasmas* 6, 932 (1999); D. Palmer Smitherman, R. E. Chrien, N. M. Hoffman, and G. R. Magelssen, "Feed-out Coupling of Richtmyer-Meshkov and Rayleigh-Taylor Instabilities in Stratified, Radiation-Driven Foils," *Physics of Plasmas* 6, 940 (1999).

[12] D. L. Tubbs, C. W. Barnes, J. B. Beck, N. M. Hoffman, J. A. Oertel, R. G. Watt, T. Boehly, D. Bradley, P. Jaanimagi, and J. Knauer, "Cylindrical Implosion Experiments using Laser Direct Drive," *Physics of Plasmas* 5 (to be published in 1999).

[13] C. J. Keane, G. W. Pollak, R. C. Cook, T. R. Dittrich, B. A. Hammel, O. L. Landen, S. H. Langer, W. K. Levedahl, D. H. Munro, H. A. Scott, and G. B. Zimmerman, "X-ray Spectroscopic Diagnostics of Mix in High Growth Factor Spherical Implosions," *Journal of Quantitative Spectroscopy and Radiative Transfer* 5 4, 207 (1995).

[14] O. L. Landen, C. J. Keane, B. A. Hammel, W. K. Levedahl, P. A. Amendt, J. D. Colvin, M. D. Cable, R. Cook, T. R. Dittrich, S. W. Haan, S. P. Hatchett, R. G. Hay, R. A. Lerche, R. McEachern, T. J. Murphy, M. B. Nelson, L. Suter, and R. J. Wallace, "Effects of Variable X-Ray Preheat Shielding in Indirectly Driven Implosions," *Physics of Plasmas* 3, 2094 (1996).

[15] E. M. Campbell, "Recent Results from the Nova Program at LLNL," *Lasers and Particle Beams* 9, 209 (1991).

[16] S. V. Weber, B. A. Remington, S. W. Haan, B. G. Wilson, and J. K. Nash, "Modeling of Nova Indirect Drive Rayleigh-Taylor Experiments," *Physics of Plasmas* 1, 3652 (1994); B. A. Remington, S. V. Weber, S. W. Haan, J. D. Kilkenny, S. G. Glendinning, R. J. Wallace, W. H. Goldstein, B. G. Wilson, and J. K. Nash, "Laser-Driven Hydrodynamic Instability Experiments," *Physics of Fluids B* 5, 2589 (1993).

[17] R. J. Wallace, R. L. McEachern, and W. W. Wilcox, "Laser Ablation Machining of ICF Capsules," *ICF Quarterly Report* 4, 79–86,

Lawrence Livermore National Laboratory report UCRL-LR-105821-94-3 (To obtain a copy of this document, request Document No. DE 95011970 from the National Technical Information Service, Springfield, VA 22161).

[18] R. E. Chrien, D. F. Simmons, and D. L. Holmberg, "Neutron Time-Of-Flight Ion Temperature Diagnostic for Inertial-Confinement-Fusion Experiments," *Review of Scientific Instruments* 63, 4886 (1992).

[19] M. B. Nelson and M. D. Cable, "LaNSA: A Large Neutron Scintillator Array for Neutron Spectroscopy at Nova," *Review of Scientific Instruments* 63, 4874 (1992).

[20] H. Brysk, "Fusion Neutron Energies and Spectra," *Plasma Physics* 15, 611 (1973).

[21] T. J. Murphy, R. E. Chrien, and K. A. Klare, "Neutron Time-of-Flight Signals from Expanding or Contracting Spherical Sources," *Review of Scientific Instruments* 68, 614 (1997).

[22] N. M. Hoffman, D. C. Wilson, W. S. Varnum, W. J. Krauser, and B. H. Wilde, "Multimode Hydrodynamic Stability Calculations for National Ignition Facility Capsules," 12th International Conference on Laser Interactions and Related Plasma Phenomena (Osaka, Japan, April 1995), *Laser Interations and Related Plasma Phenomena*, S. Nakai and G. H. Miley, Eds. (American Institute of Physics Press, Woodbury, New York, 1996).

[23] W. J. Krauser, N. M. Hoffman, D. C. Wilson, B. H. Wilde, W. S. Varnum, D. B. Harris, F. J. Swenson, P. A. Bradley, S. W. Haan, S. M. Pollaine, A. S. Wan, J. C. Moreno, and P. A. Amendt, "Ignition Target Design and Robustness Studies for the National Ignition Facility," *Physics of Plasmas* 3, 2084 (1996).

[24] G. Zimmerman and W. Kruer, "Numerical Simulation of Laser-Initiated Fusion," *Comments on Plasma Physics and Controlled Fusion* 11, 51 (1975).

[25] S. W. Haan, S. M. Pollaine, J. D. Lindl, L. J. Suter, R. L. Berger, L. V. Powers, W. E. Alley, P. A. Amendt, J. A. Futterman, W. K. Levedahl, M. D. Rosen, D. P. Rowley, R. A. Sacks, A. I. Shestakov, G. L. Strobel, M. Tabak, S. V. Weber, G. B. Zimmerman, W. J. Krauser, D. C. Wilson, S. V. Coggelshall, D. B. Harris, N. M. Hoffman, and B. H. Wilde, "Design and Modeling of Ignition Targets for the National Ignition Facility," *Physics of Plasmas* 2, 2480 (1995).

[26] S. W. Haan, "Onset of Nonlinear Saturation for Rayleigh-Taylor Growth in the Presence of a Full Spectrum of Modes," *Physical Review A* 39, 5812 (1989).

Trident Research Campaigns

D. S. Montgomery, R. P. Johnson,
J. A. Cobble, J. C. Fernandez,
A. A. Hauer, and G. A. Kyrala
(P-24);
E. L. Lindman (XTA);
H. A. Rose (T-13); and
K. G. Estabrook (Lawrence
Livermore National Laboratory)
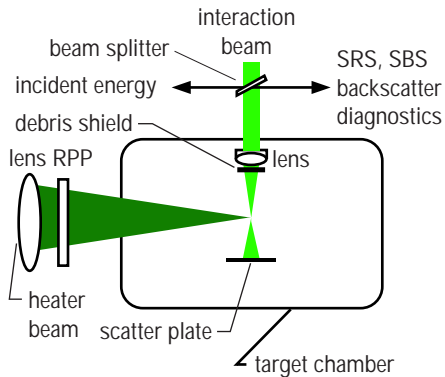
Fig. 1 Schematic top-view of the laser beam and diagnostic configurations used in the single hot-spot interaction experiments.

Introduction

During the past two years, the Trident laser facility has provided over 2,200 laser shots for 25 different experimental campaigns involving experimentalists from Los Alamos National Laboratory, Sandia National Laboratory, Lawrence Livermore National Laboratory, and colleges and universities around the country and the world, including Imperial College and Oxford University in the United Kingdom, Ecole Polytechnique in France, the University of Maryland, the University of Michigan, and the University of California at San Diego. Roughly one-quarter of the Trident experimental campaigns have been fielded by personnel from the Los Alamos Plasma Physics Group (P-24) for diagnostic development or testing of diagnostics in preparation for experiments at Trident or Livermore's Nova or the University of Rochester's Omega laser systems. The remaining experimental campaigns have been independent experimental campaigns fielded to address the individual goals of various universities or to support the goals of the local Inertial Confinement Fusion (ICF) Program. Most of the laser time was devoted to two major experimental programs, one to study laser plasma instabilities and the other to study dynamic properties of materials. University users were also involved as collaborators in these two very important areas.

Most campaigns were carried out on the main Trident target chamber, but a number of campaigns were accomplished on two auxiliary target chambers using Trident's short-pulse capability. Some of these involved diagnostic development, testing, and calibration while others addressed the nature of the interaction of a very high-intensity laser pulse with a plasma. These latter campaigns were conducted to test aspects of the fast-ignitor concept for ICF ignition at the National Ignition Facility (NIF).

This research highlight will focus on the two experimental campaigns that used most of the laser time. The first is sponsored by the Laboratory Directed Research and Development (LDRD) Program to study laser plasma instabilities. Its focus is to study the interaction of a single laser hot spot with a pre-formed plasma with a view to understanding, in more realistic laser beams, the parametric scattering instabilities that pose a threat to ICF ignition. The second campaign, part of the dynamic properties of materials program, focussed on developing experimental techniques to study shock-induced melt and other phase transformations in materials under the extreme conditions of interest to ICF and weapons physics. These campaigns are discussed individually below.

Characterizing Plasma and Laser Conditions for Single Hot-Spot Interaction Experiments

Laser beams are scattered by density fluctuations (waves) in a plasma because these fluctuations alter the index of refraction that the laser encounters. With low amplitude waves, this process (called collective Thomson scattering) is benign, and it provides a powerful tool for diagnosing plasma conditions. On the other hand, stimulated scattering involves the unstable growth of waves in the

plasma fed by the laser energy. These waves can scatter a significant fraction of the laser energy in undesirable directions. Stimulated scattering by electron plasma waves (Raman scattering) and ion-acoustic waves (Brillouin scattering) poses a significant threat to ICF.

The Trident laser system was used for fundamental experiments addressing the interaction of laser self-focusing, stimulated Raman scattering (SRS), and stimulated Brillouin scattering (SBS) in a near-diffraction-limited (single) laser hot spot under ICF-relevant plasma conditions. Our aim was to gain a better understanding of the coupling between these plasma instabilities. This laser-plasma system is sufficiently small for direct modeling by an emerging suite of computer codes incorporating new theoretical models. If we succeed in understanding this system, we hope to develop simpler models suitable for quantitative predictions in much larger ignition plasmas. The first step in this process is to create an ignition-relevant plasma and to characterize it thoroughly and accurately.

In our investigation, one of Trident's three 527-nm laser beams was used to create and heat a long-scale-length plasma (~1 mm, ~0.6 keV). A second, lower-energy Trident beam was then used to produce a nearly diffraction-limited interaction laser beam with minimal wave-front distortion incident in the target plasma. Figure 1 shows a schematic of the laser and diagnostic configuration used in our experiments.

The plasma heater beam was focused with an f/6 aspheric lens and a "stripline" random phase plate (RPP), which produces a line focus with dimensions of ~100-µm high × 1,000-µm long.[1] The laser energy is 160 ± 10 J in a 1.3-ns pulse at constant power with 100-ps rise and fall times. It illuminates a 1-mm-diameter plastic or aluminum target at normal (perpendicular) incidence with the line focus in the horizontal plane. The interaction beam was focussed on the target using an air-spaced achromat lens with a 250-mm focal length (f) positioned at f/7. This lens was mounted inside the vacuum chamber where the plasma is generated, so a high-quality debris shield was placed between the lens and target to protect the lens. The interaction beam was incident 90° to the heater beam and was offset parallel to the target surface by between 100 and 400 µm to vary the sampled plasma density. The 200-ps interaction beam was delayed by 1.8 ± 0.05 ns with respect to the beginning of the heater beam so that the heater beam was off when the interaction pulse was on. This delay is important because it removes any influence of the heater beam on the experiment.

A beam splitter was placed in the interaction beam to sample the incident beam energy and the reflected light from the plasma scattering processes. The extensive diagnostics for the scattered light on Trident, used to study SRS and SBS, are beyond the scope of this article and will not be described.

To characterize the interaction laser, we measured the focal plane intensity distribution using a 40× microscope objective and a charge-coupled device (CCD) camera. Figure 2 shows an image of the interaction laser at best focus (a) and an azimuthally averaged
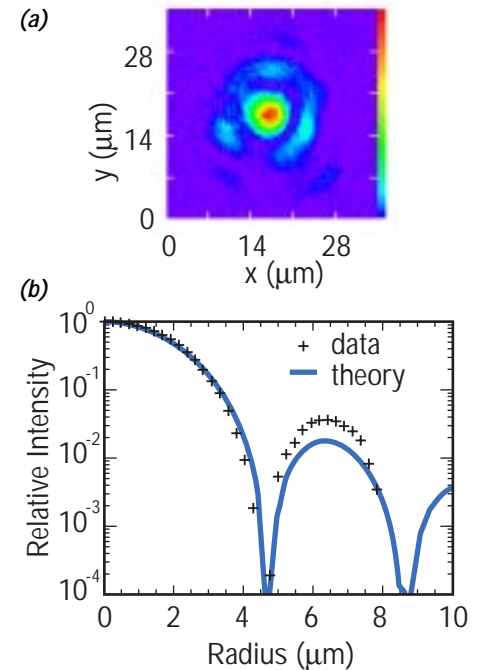
Fig. 2 (a) Far-field image of the single hot spot beam (the colors represent light intensity with red being the highest, blue being the lowest, and black being no intensity). (b) Azimuthally averaged radial profile of the far field data, with diffraction from an ideal f/7 beam superimposed.
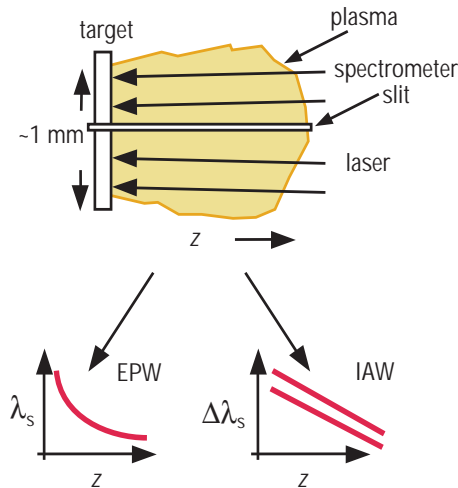
Fig. 3 *Schematic bottom-view of the target and the imaging spectrometer orientation with respect to the target and heater beam for Thomson scattering measurements. The graphs show a cartoon of the expected scattering from EPWs and IAWs for this configuration.*
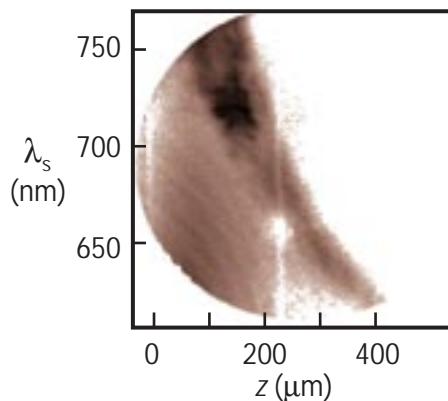

Fig. 4 *Scattering from EPWs as a function of distance from the target surface at* t *= 1.0 ± 0.1 ns for a plastic plasma. The vertical features at* z *= 0 and* z *= 200 μm are artifacts due to dead spots on the detector.*

radial profile (b). Superposed is the theoretical radial profile for diffraction from a plane wave incident on a circular aperture at *f*/7 (the theoretical ideal performance), which is in excellent agreement with the measured results.

The interaction laser beam has a full-width at half maximum (FWHM) of 3.8 ± 0.15 μm, and it produces a peak intensity of 1×10^{16} W/cm^2 for a nominal energy of 0.8 J (maximum) in a 200-ps FWHM Gaussian pulse. The peak intensity can be adjusted between 10^{14} and 10^{16} W/cm^2 using polished, calibrated neutral density filters.

We measured the angular distribution of the transmitted interaction laser by having the transmitted beam illuminate a diffuser, which was then imaged onto a CCD camera filtered for 527 ± 5 nm. The camera system was absolutely calibrated so that transmitted energy measurements were obtained. This measurement, which is important to diagnose the laser-plasma instabilities, will not be discussed further.

To characterize the plasma, we used a 5-cm focal length, *f*/6 achromat to collect Thomson scattered light at 90° from the heater beam. The target was imaged onto the slit of a 0.5-m imaging spectrometer with the image oriented along the direction of the plasma expansion, perpendicular to the target surface. The output of the spectrometer was coupled to a gated optical camera with ~120-ps frame time and the image was recorded using a CCD camera. The spectrometer was operated in either low or high dispersion to measure Thomson-scattered signals from electron plasma waves (EPWs) or ion acoustic waves (IAWs).

A schematic of the Thomson scattering measurement is given in Fig. 3, which also shows the slit orientation with respect to the target image. The sampled scattering volume at the target plane was ~10 μm wide (slit width) with ~100-μm line-of-sight depth through the plasma. The imaging direction of the spectrometer is oriented along the plasma-expansion direction, allowing reconstruction of the scattered-light profile with a 25-μm resolution.

Scattering from EPWs was examined to obtain measurements of the plasma density profile. Using the dispersion relations for the EPWs and scattered light, the scattered light should go from long wavelength near the target surface to shorter wavelength farther away as the density goes from high to low, as indicated in the graph in Fig. 3. Figure 4 shows a corresponding measurement of scattering from EPWs versus distance from the target near the end of the heater pulse (*t* = 1.0 ± 0.1 ns) for a 6.5-μm-thick plastic target. The spectrum at a given distance from the target surface shows a cutoff at a maximum wavelength, which corresponds to the peak density at that position. A density profile is obtained from the data by finding the edge of the maximum wavelength cutoff versus position, and assuming an electron temperature, T_e, equal to 0.5 ± 0.1 keV in the dispersion relations. A plot of the inferred electron density, n_e/n_{cr}, where n_{cr} is the critical density ($n_{cr} = 4 \times 10^{21}$ cm^{-3}, above which 527-nm light does not propagate), *vs.* position from the target surface is shown in Fig. 5.

Collective Thomson scattering from IAWs is used to measure profiles of electron temperature (T_e), ion temperature (T_i), and flow velocity (v_z). The scattering geometry determines the wave-number of the IAWs being probed and is given by $k_{IAW} = 2k_0 \sin(\Theta/2)$, where $k_0 = 2\pi/\lambda_0$ is the laser wave-number, and Θ is the angle between the incident and scattered light. The dispersion relations indicate that the separation between the upshifted and downshifted IAWs is a function of T_e, and the flow velocity produces a Doppler shift of the entire spectrum, as indicated in the graph in Fig. 3 for an isothermal plasma, which turns out to be a good assumption. A corresponding measurement of Thomson-scattered light from IAWs *vs.* distance is shown in Fig. 6 near the end of the heater pulse ($t = 1.0 \pm 0.1$ ns) for a 6.5-μm thick plastic target. The separation between the upshifted and downshifted waves is clearly resolved, and the entire spectrum becomes more Doppler shifted further from the target surface, indicating an increased flow speed at increased separation from the target surface.

A spectral lineout taken at the location $z = 300 \pm 25$ μm is shown in Fig. 7. The spectrum is asymmetric, indicating a relative drift between electrons and ions, and is due either to transport effects or
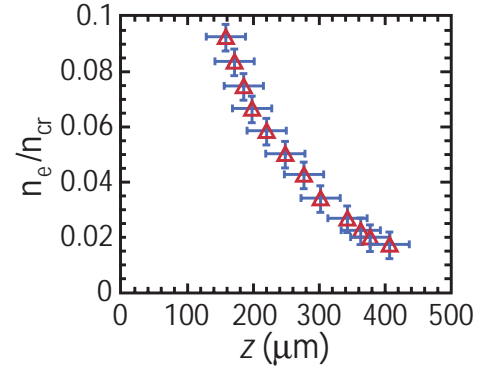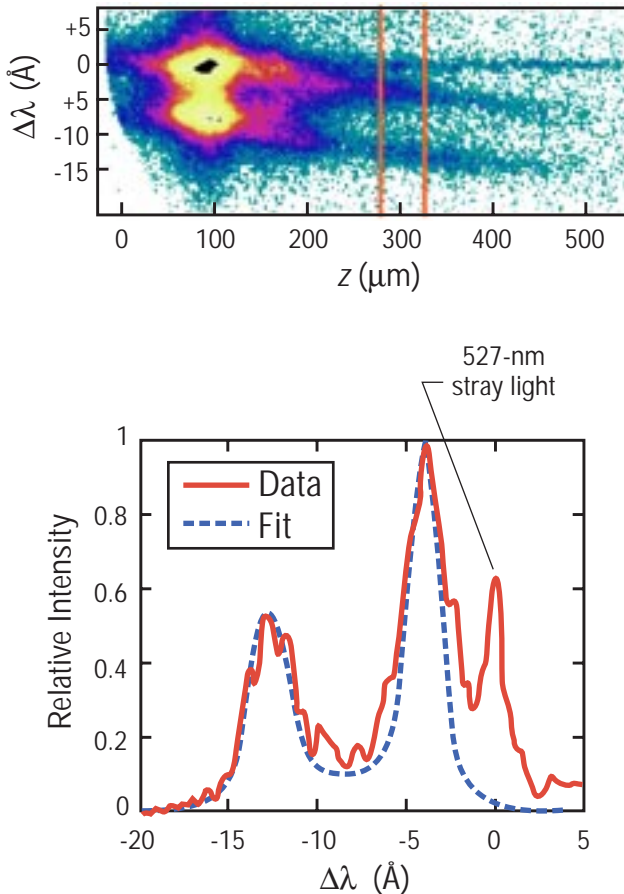

Fig. 5 *The electron density profile* vs. *distance from the target surface obtained from the EPW data shown in Fig. 4.*

Fig. 6 *Scattering from IAWs as a function of distance from the target surface at t = 1.0 ± 0.1 ns for a plasma plasma.*

Fig. 7 *Spectral profile taken from the IAW data shown in Fig. 6 at z = 300 ± 25 μm. Superimposed is a fit for the Thomson scattering form factor for a fully ionized plastic plasma, with fit parameters T_e = 0.7 ± 0.1 keV, T_i = 0.14 ± 0.05 keV, and v_z = 4.8 ± 0.4 x 10^7 cm/s. The spectral line at Δλ = 0 is due to stray 527-nm light, which provides a convenient wavelength fiducial.*
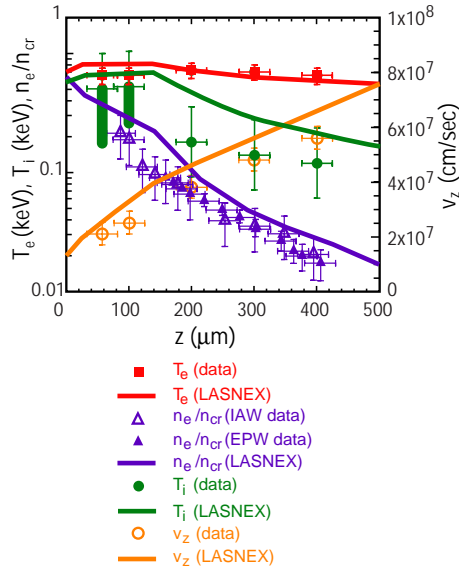
Fig. 8   Plot of electron density (n_e/n_{cr}), electron temperature (T_e), ion temperature (T_i), and flow velocity (v_z) profiles at t = 1.0 ± 0.1 ns measured by Thomson scattering from the EPW and IAW data shown in Figs. 4 and 6. Simulated plasma profiles from 2-D LASNEX calculations are also shown.

to stimulated processes. The separation between peaks is mostly dependent on electron temperature, T_e, and weakly dependent on ion temperature, T_i. The width of each peak and the contrast between the center of the spectrum and the peak heights are dependent on T_i, and the overall Doppler shift from λ_0 depends on flow velocity. The entire spectrum is fitted using the Thomson scattering form factor for multi-ion species plasmas[2], and is used to determine T_e, T_i at that position. The flow velocity, v_z, is determined assuming that the dominant flow component is mostly parallel to the heater beam. Figure 8 shows the experimentally measured profiles of n_e/n_{cr}, T_e, T_i, and v_z at $t = 1.0 \pm 0.1$ ns for a plastic target derived from the Thomson scatter data shown in Figs. 4 and 6. Calculations of the plasma profiles using the 2-D hydrodynamics code LASNEX[3] are also shown as lines in Fig. 8 and are in rough agreement with the measurements. These data can be used to further refine the simulations for the experimental design.

In summary, we have produced ignition-relevant long-scale plasmas on Trident. The plasma conditions have been characterized with unprecedented detail using Thomson scattering. A nearly diffraction-limited laser beam suitable for interaction experiments has been produced and thoroughly characterized. Given these measurements, theoretical simulations of laser-plasma instability processes will be performed, and detailed comparisons to measurements will be made. We expect to gain sufficient understanding of these processes to allow the development of models suitable for quantitative predictions on ignition-scale plasmas.

## Shock Wave Physics and High Pressure Materials Science Research

P-24, in collaboration with Los Alamos National Laboratory's Materials Science and Technology (MST), Dynamic Experimentation (DX), Applied Theoretical and Computational Physics (X), and Theoretical (T) Divisions, as well as Oxford University, Livermore, Sandia, the University of California at San Diego, and the University of Edinburgh, pursues an active research program in shock-wave physics and related materials science. The Trident laser system is used to drive moderate to high-pressure shock waves into condensed-state materials, and the response of the materials is diagnosed with an array of advanced diagnostics. These measurements are used to determine dynamic properties of materials that are of importance to the inertial fusion and the weapons programs. A modest-size laser system like Trident is well suited to certain areas of high-pressure materials science, providing accurate and flexible control over the temporal profile of shock generation, a wide range of achievable pressures (~0.05–30 Mbar), and very bright x-ray sources accurately synchronized to the shock generation. In addition, many shots can be fielded rapidly for accurate studies of various parameters. This section gives a brief review of some of the recent high-pressure materials work on the Trident laser.

A typical configuration for Trident materials science experiments is shown in Fig. 9. In this particular case the principal diagnostic method was transient x-ray diffraction[4], a method to which Trident experiments have made significant contributions. One beam of the laser system is used to drive a shock wave into the sample. Another beam is used to generate an intense x-ray source, in this case a point source of 6.1-keV radiation. In this example the x-rays diffract off planes roughly parallel to the entrance surface. This mode of diffraction is referred to as Bragg diffraction. As the shock wave reaches the rear surface of the crystal, the lattice planes are compressed and the Bragg angle of diffraction is changed. The angular deflection of the diffracted x-ray beam is thus directly proportional (through Bragg's law) to the real time-strain induced in the crystal by the shock wave. An example of typical data obtained using such a configuration is given in Fig. 10.

The x-ray streak record shown in Fig. 10 illustrates several important aspects of the shock propagation and its effect on the diffraction of x-rays. The lower portion of the streak represents diffraction from unshocked material before the shock wave has reached the rear surface of the crystal. As the shock comes within the probe distance of the x-rays, a portion of the diffracted x-rays are deflected to a higher angle and thus strike the streak camera slit at a different position. The separation of this streak from the uncompressed portion is directly proportional through Bragg's law to the strain induced in the crystal by the shock wave. The strains induced are typically large, on the order of a few percent. The strain rates are also quite large, ranging from 10^7 to 10^9 s^{-1}. The dynamics of solid-solid phase changes is one important phenomenon that can be studied by such methods.
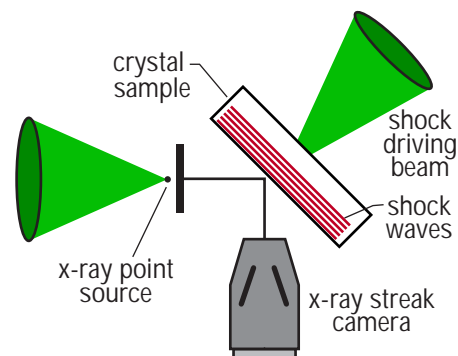

Fig. 9 A typical experimental configuration used on the Trident laser for shock wave and materials science studies.
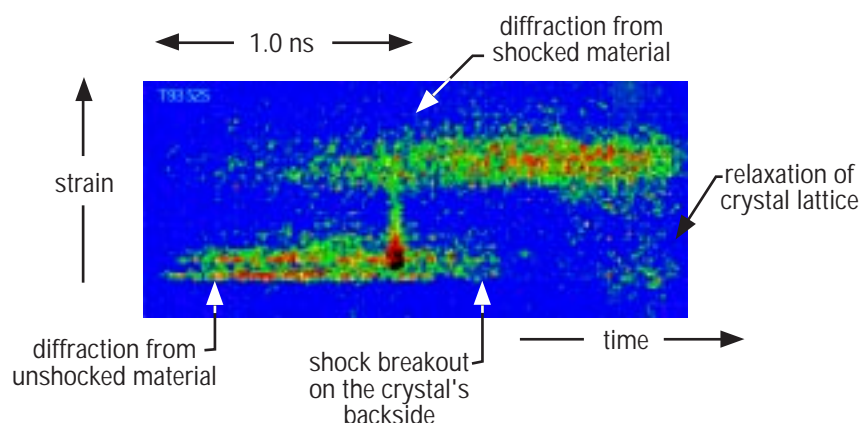
Fig. 10 Typical example of transient diffraction data obtained in shock wave materials research on the Trident laser. The peak shock pressure was about 150 kbar.

Figure 11 illustrates typical data from phase change studies. The several shots displayed represent a progression of increasingly higher shock pressure (generated by higher laser irradiances). In this case the diffraction is occurring from the <400> planes of a silicon crystal. At a particular threshold in pressure, the crystal goes through a phase change from the normal diamond cubic configuration to another configuration, most likely a body-centered tetragonal configuration. In the highest-pressure streak, the diffraction from compressed material is seen to split into two components indicative of the phase change. Through records of this sort, the dynamic properties of the phase change can be studied. These data are currently being compared with hydrodynamic simulations that include a new multiphase equation of state. This equation of state takes into account the observed phase change. Recent simulations using this multiphase equation of state have predicted that the dynamic threshold for this phase change should occur at about 200 kbar, which is quite close to the threshold that is observed experimentally. The next stage of this research will extend this work to another phase change: melt.

Fig. 11 Transient diffraction data from a material undergoing a shock-induced phase change.
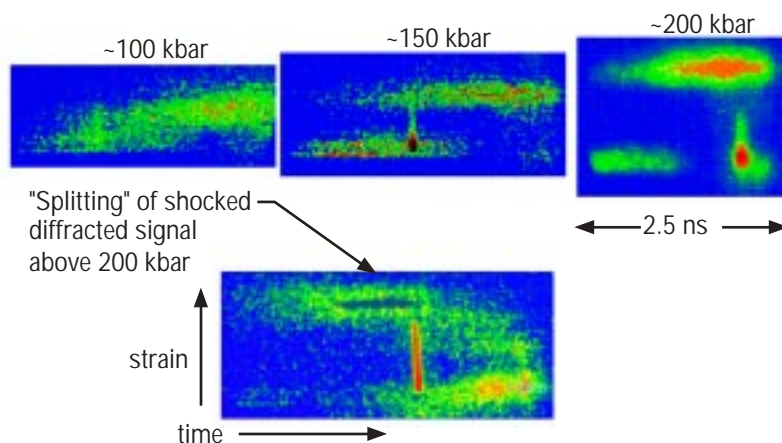
Other materials science work on Trident focuses on plastic wave generation. Plastic behavior of materials occurs when shock waves have pressures above the elastic limit. Typically, condensed matter subjected to pressures above the elastic limit yields through generation of dislocations and other faults in the crystalline structure. One method for diagnosis and analysis of these fault generation mechanisms is post-shot analysis of the materials. Special systems "catch" the fragments of material after the shock event. Thin slices of the material are then subjected to analyses such as transmission electron microscopy. An example of this analysis is given in Fig. 12. The characteristic dislocation signatures indicate where the material has yielded when subjected to the high-pressure shock wave. The next stage of this research will compare the dislocation generation with molecular dynamics modeling. Molecular dynamics modeling is the most basic, first-principles approach to predicting the response of condensed materials to high-pressure shock waves. (The comparisons will be made with molecular dynamics calculations performed by Brad Holian and his
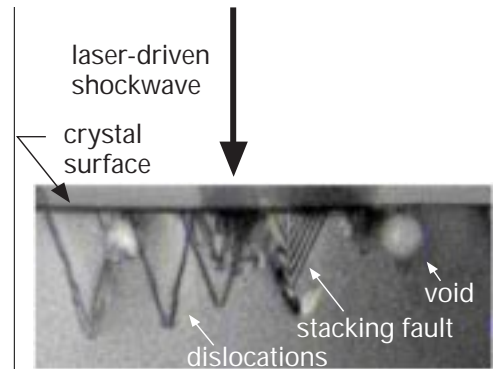
colleagues in T-11 and T-12.) It represents a first step in building a comprehensive picture of material behavior beginning at the atomic level and progressing to dislocation generation and finally macroscopic faults. The data obtained in experiments such as these can help to critique and benchmark this modeling.

Experiments on the Trident laser system have provided useful data on the dynamic properties of materials. In particular, we have developed new transient x-ray diffraction methods for studying the temporal structure of shock-induced solid phase changes, and methods for post-shot analysis of shock-induced dislocation generation. In addition, experimental data on phase changes have been compared with hydrodynamic modeling that uses the most advanced multiphase equations of state. The thresholds for the phase change predicted by the modeling agree well with experimentally observed values.

Trident experiments have also provided a useful test bed for developing new measurement methods and techniques that can be applied to larger-scale materials work on pulsed-power machines, gas guns, and explosive facilities. This review represents only a short summary of the broad range of materials research that we conduct using high-power radiation sources and pulsed-power radiation generators. We believe that this research will provide a useful supplement to traditional methods relying on explosives to generate the high pressures.

Fig. 12   Electron microscopy analysis of dislocations generated by a high-pressure laser-driven shock wave.

References

[1]B. S. Bauer, R. P. Drake, K. G. Estabrook, J. F. Camacho, R. G. Watt, M. D. Wilke, G. E. Busch, S. E. Caldwell, and S. A. Baker, "Meeting the Challenge of Detecting Ion-Plasma Waves," *Physics of Plasmas* 2, 2207 (1995).

[2]D. E. Evans, "The Effect of Impurities on the Spectrum of Laser Light Scattered by a Plasma," *Plasma Physics* 12, 537 (1970).

[3]G. Zimmerman and W. Kruer, "Numberical Simulation of Laser-Initiated Fusion," *Comments on Plasma Physics and Controlled Fusion* 2, 51 (1975).

[4] A. A. Hauer and G. A. Kyrala, "Laser-Plasma X-Ray Emission: Its Creation, Diagnosis and Application in Transient Diffraction," in *Time Resolved Diffraction*, J. R. Helliwell and P. M. Rentzepis, Eds. (Oxford Clarendon Press, Oxford, 1997), pp. 71–103.

Development of an Infrared Imaging Bolometer

G. A. Wurden and H. A. Alvestad (P-24)

Introduction

As magnetic fusion plasmas become larger, hotter, and therefore contain more energy, precise control of the plasma becomes even more critical. Today's fusion plasmas are generally "shaped" to allow for more efficient confinement of the plasma by magnetic fields. Shaping requires the plasma position to be both measured and controlled on timescales ranging from milliseconds to hours. This control requires a range of diagnostic tools that measure as many plasma parameters as possible. These plasma diagnostics must be able to survive for long periods in a harsh environment consisting of nuclear radiation (gamma rays and neutrons), vacuum conditions, exposure to plasma bombardment, and strong magnetic fields. In developing such diagnostics, the necessary access requirements, sensitivity, noise, and cost per channel (of a multichannel instrument) must also be considered. To meet these needs, we have developed and patented an imaging bolometer system (U.S. Patent 5,861,625) using infrared readout of a segmented metal foil. Our bolometer allows hundreds to thousands of channels of data, it requires no wiring harness, and it is intrinsically radiation-hard.

Infrared Imaging Bolometer

A bolometer is an instrument that measures the total radiation incident upon it, preferably with an appropriate time resolution. Bolometers are used to study the radiation emission profiles of fusion plasmas, which provide valuable information about the locations and amounts of plasma impurities. Often, the radiation emitted by a fusion-grade plasma is "hollow," that is, it is localized in the outer regions of the plasma. The magnitude of the radiation emitted by the plasma will usually be in the range of 10–100% of the heating power (from 10 kW up to tens of Megawatts), which sustains the plasma. Most bolometers use a material, such as gold, platinum, or tantalum, to absorb the radiation and convert it into heat. The resulting temperature increase is detected by monitoring some physical characteristic of the material. This characteristic could be the change in resistance, a piezo-electric effect, or (in our case) the amount of infrared radiation emitted by the absorbing material. In all present-day, large-scale plasma devices, large arrays of single-element bolometers have been used to measure the plasma's radiation profile. The systems are hampered by the fact that each detector requires at least two wires carrying low-level signals through the vacuum vessel to the outside world. The wiring is difficult to install and maintain (insulators degrade in radiation fields), and it is a source of background noise.

Bolometers are not a new diagnostic. Our work, however, offers new capabilities for plasma diagnostics by combining the latest digital state-of-the-art infrared video technologies (developed originally for missile interceptor programs and the Clementine spacecraft that flew to the moon). These infrared video cameras operate in the 3- to 12-µm wavelength band with

12-bit dynamic range, sensitivity limits of $\Delta T = 0.01°C$, arrays of 256×256 elements, and read-out rates of up to 1 kHz, and are now commercially available. We use such a camera to view a customized segmented-foil that we developed, generating a time-resolved image of the radiation emitted from a plasma.

Radiation damage on conventional bolometers, which need insulators for wiring and usually have multilayered thin film materials that might blister under intense radiation exposure, is a serious concern for the next generation of fusion experiments and reactors. Our bolometer offers an elegantly simple solution. It uses no wires and no insulators, it uses only metal components near the plasma, and it relies on the bulk property (thermal heat capacity) of a metal. These characteristics make this instrument very robust, relatively radiation-resistant, and more stable over the long term. Given these characteristics, it is possible that our instrument might be used on an International Thermonuclear Experimental Reactor (ITER) class (1 GW level) fusion reactor for long periods of time before requiring replacement.

In years past, infrared readout of the back side of a single, thin-foil "detector" has been used to measure the radiation power incident on the front side of the foil. Such detectors were typically used to eliminate particularly difficult electromagnetic interference problems that arise due to pick-up in the leads of traditional resistive readout bolometers. Similarly, infrared cameras have been used to take "snapshots" of the distribution of heat on a foil exposed to a pulsed ion or neutral beam. Such snapshots can be used to diagnose the beam profile, but they do not provide any time resolution. The initial heat distribution is "frozen in" on the foil for a few video frames. To measure a subsequent beam pulse, the researcher had to wait until the heat either diffused or radiated away and then "reinitialize" the foil to avoid confusion. This technology has many limitations. For example, to simultaneously use hundreds or thousands of detectors (bolometer "pixels"), the researcher must have a way to keep the heat deposited on one pixel from flowing into the adjacent pixel, or risk confusing the measurements. In addition, if the expected temperature rise on the foil is around 10°C per second, as it would be in long-pulse plasma applications, then the foil material would melt without active cooling.

Our goal was to develop a multi-element imaging bolometer that is actively cooled, but with thermally isolated pixels. Our first idea was to use a "back-cooled, front-viewed" configuration. The concept was tested with a bed of roofing nails, as shown in Fig. 1. Each nail (pixel) is thermally isolated from its neighbor and cooled by an "infinite heat sink" in which the nail is anchored. In this design, the decay time of the heat on the nails was much too long for plasma applications, but it provides a good graphical illustration of the concept of a segmented sensor matrix.
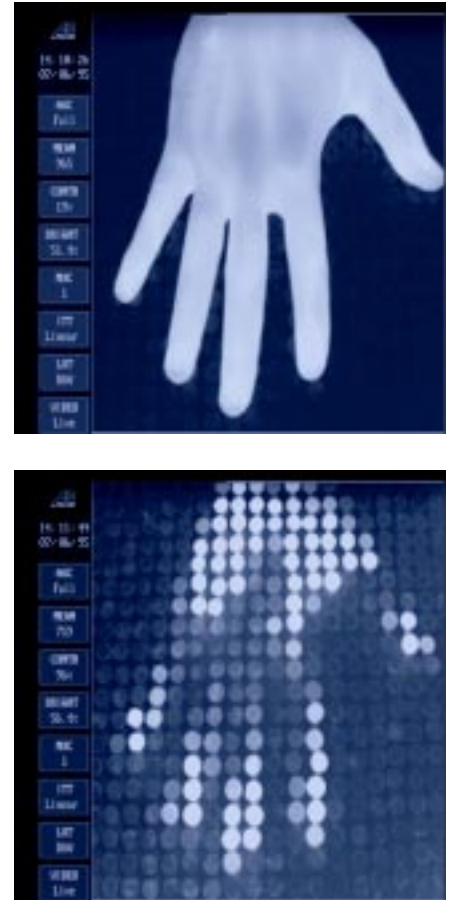

Fig. 1   An array of 20 × 20 roofing nails was used to test the concept of a "back-cooled, front-viewed" bolometer configuration. The heads of the nails are thermally isolated from each other, as shown in these two infrared pictures. The top image is a hand, and the bottom image is the thermal image of the hand remaining on the heads of the nails.

Subsequently, we changed to a "back-viewed, side-cooled" design, recognizing that stray thermal radiation from hot armor tiles in the plasma vacuum vessel might contaminate the measurement. This modified design is shown in an artist's conception in Fig. 2. To maximize the sensitivity (minimize the heat capacity), the foil must be as thin as is mechanically possible; however, to ensure that the desired range of plasma radiation (up to ~1–10 keV photons) is absorbed in the foil, the foil must be thick enough to stop soft x-ray photons.

Fig. 2 Artist's sketch of the infrared imaging bolometer, which employs a pinhole camera design with a mask/foil combination viewed by a digital infrared video camera.
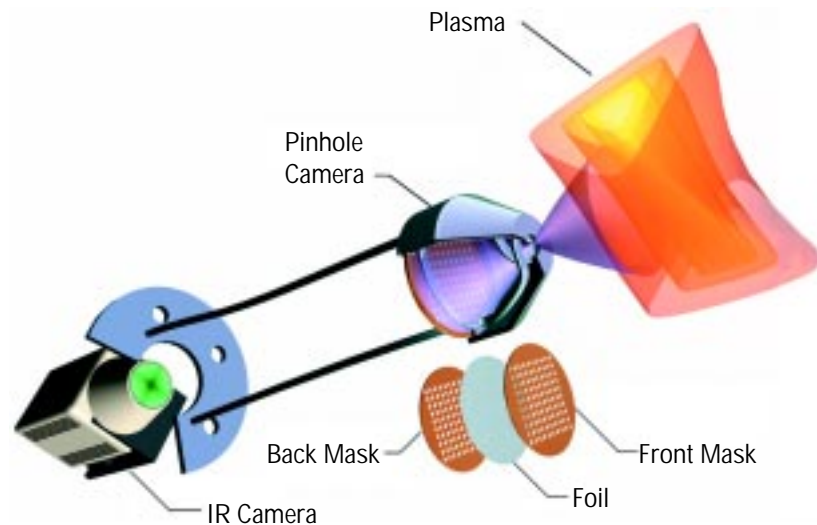
International Collaboration

In the absence of a Los Alamos-based, large-scale fusion plasma research facility, Los Alamos scientists pursue international collaborations to field new diagnostic tools. In the Plasma Physics Group (P-24), we are involved in ongoing collaborations with researchers at the Japanese Atomic Energy Research Institute (JAERI) using the JT-60U machine, which is the world's largest operating tokamak. We are also collaborating with researchers at the National Institute for Fusion Science (NIFS) in Toki, Japan, where the Large Helical Device (LHD), a $1B-class superconducting stellarator, will soon be in operation (see Fig. 3). As part of the U.S. Department of Energy Japan Fusion Exchange Agreement, we began collaborating with NIFS scientists to develop a plasma diagnostic that would meet the needs of the future LHD.

The LHD plasma will have a complex, helical shape. To understand the behavior of this plasma, multiple sight-lines and preferably even multiple imaging diagnostics will be required. In addition, because the LHD is a superconducting machine, long

pulse operations will be used. These pulse operations might range from 10 minutes to one hour, limited only by heating in the sources and the available electric power grid. Such long-pulse operation will require a diagnostic that is able to gather enormous quantities of data with real-time data-handling capabilities.

In the summer of 1997, we performed the first plasma tests on a prototype diagnostic system using the Compact Helical Stellarator (CHS) plasma at Nagoya University. Using an Amber Radiance 1 digital infrared camera (3- to 5-μm band) with 25-millidegree sensitivity and both 0.5- and 1.0-μm thick gold foils, we obtained signals from a short-pulse (~100-ms duration) plasma heated by electron cyclotron and neutral beam sources. We blackened the backside of the gold foils with a carbon spray to obtain a thermal emissivity of nearly 1, which means that each foil's infrared emission represents its temperature. In addition to the expected signals, we found unwanted heating from stray microwave radiation used to create and heat the plasma. Typically, 10 mW of energy produces a signal of 4°C on the foil.

We performed a second series of tests in spring of 1998 using an Agema Thermovision camera (8- to 12-μm band) with a fast linescan (2.5 kHz) mode of operation, which allowed better time resolution, more in accordance with the short duration
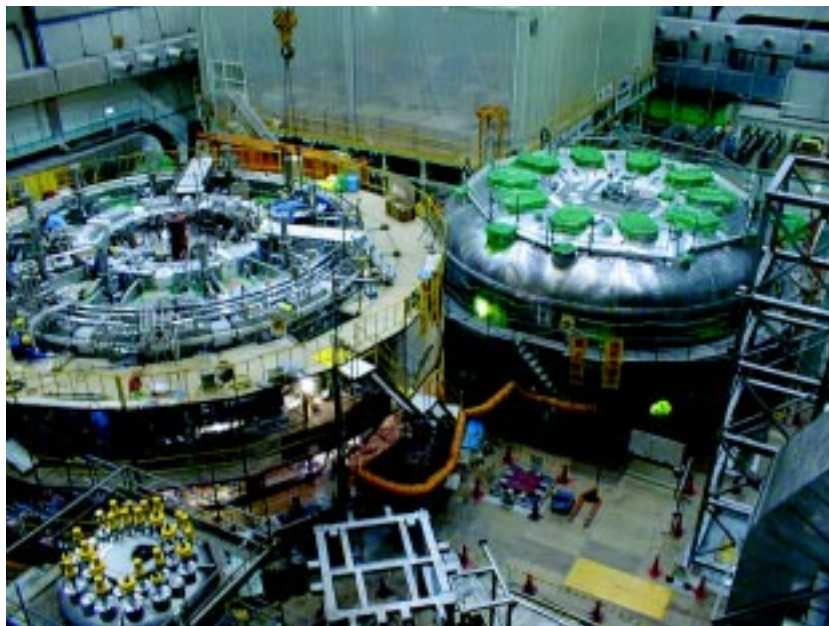

Fig. 3 *The superconducting LHD device under construction in October 1997 at the NIFS site in Toki, Japan. The stainless steel cyrostat is visible on the right, while the stellarator is largely hidden by scaffolding on the left.*

(~100 ms) test plasma. These tests fully qualified the instrument and our models, and will allow us to proceed with the real diagnostic on the LHD plasma.

Upcoming Work

In the coming year, we hope to install a second-generation prototype of our imaging bolometer on a shared port with a tangential view in the superconducting, long-pulse LHD. This will give us a view of the full plasma cross section, and it should allow us to obtain time-resolved images of the total plasma radiation similar to the visible light image in Fig. 4 (but with less spatial resolution). Based on the tests to date, our imaging bolometer already shows great promise in becoming a key diagnostic for the LHD, the world's largest superconducting experimental fusion device. We anticipate that the success of this collaboration will lead us to apply our diagnostic and pulsed-power skills to other major fusion experiments around the country and the world.

Fig. 4   The complex shape of today's plasmas, as seen in this visible light tangential view of the LHD stellarator in Toki, Japan, requires diagnostics with imaging capabilities.
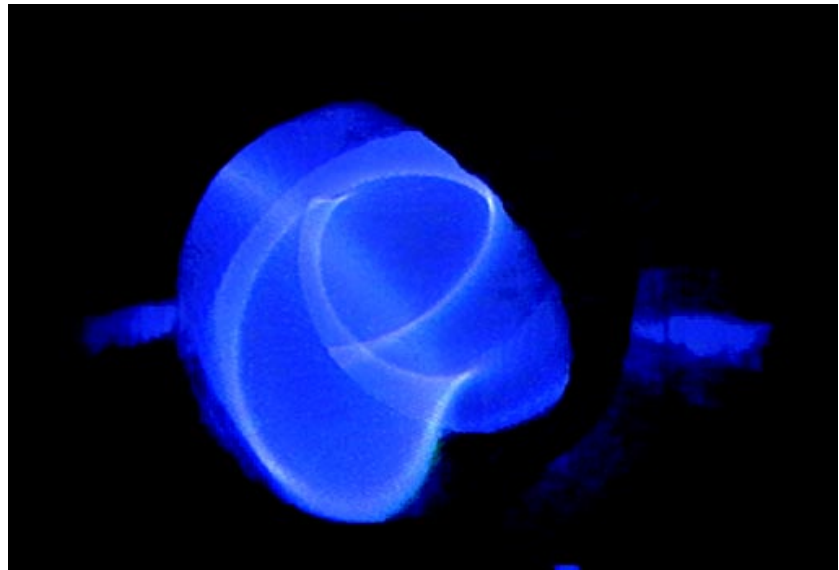
Further Reading

G. A. Wurden, " A Rad-Hard, Steady-State, Digital Imaging Bolometer System for ITER," in *Diagnostics for Experimental Thermonuclear Fusion Reactors*, P. E. Stott, *et. al.*, Eds. (Plenum Press, New York, 1996), pp. 603–606.

G. A. Wurden and B. J. Peterson, "Imaging Bolometer Development for Large Fusion Devices," ITER Diagnostics Workshop (Varenna, Italy, September 1997), in *Diagnostics for Experimental Thermonuclear Fusion Reactors*, P. E. Stott, *et. al.*, Eds. (Plenum Press, New York, 1998), pp. 399–408.

G. A. Wurden, B. J. Peterson, and S. Sudo, "Design of an Imaging Bolometer System for the Large Helical Device," *Review of Scientific Instruments* 68, 766 (1997).

Proton Radiography

J. B. McClelland for the Proton Radiography Team: Physics Division (PDO); Neutron Science and Technology (P-23); Subatomic Physics (P-25); Nuclear and Hydrodynamic Applications (XNH); Computational Science Methods (X-CM); Code Integration (X-CI); Detonation Science and Technology (DX-1); Hydrodynamic Applications (DX-3); Field Operations and Experiment Support (DX-4); Experiment and Diagnostic Design (DX-5); Machine Science Technology (DX-6); Accelerator Physics and Engineering (LANSCE-1); Accelerator Maintenance and Development (LANSCE-2); Neutron and Nuclear Science (LANSCE-3); Accelerator Operations and Technical Support (LANSCE-6); High Intensity Beam Lines, Accelerator Experimental Areas, and Remote Handling (LANSCE-7); Nuclear Theory and Applications (T-2); Weapon Engineering (ESA-WE); Lawrence Livermore National Laboratory; Bechtel Nevada; and the Indiana University Cyclotron Facility

Introduction

Los Alamos National Laboratory is leading a multilaboratory effort to demonstrate protons as a viable new radiographic probe to image imploding or exploding objects with high spatial and temporal resolution. Proton radiography represents a sharp departure from flash x-ray radiography techniques, which have been used to image dynamic processes for over 40 years. In the past, protons were used for imaging only thin objects, but the technique was limited because the proton's charge caused multiple scattering of the proton in the object, leading to a blurred image. However, we have recently demonstrated a magnetic lens system that removes the majority of the blur—even for thick objects. This technique can be extended to gain information on the material composition of an object in addition to its density by cascading two lenses with different angular apertures—a feature that conventional x-ray radiography cannot match.

An advanced radiographic capability is an essential component of the Laboratory's Science-Based Stockpile Stewardship (SBSS) program because it provides the ability to measure the integral performance of stockpiled primaries using inert materials and thereby derive nuclear performance information that previously could be obtained only from nuclear testing. Detailed data from hydrodynamic experiments are the necessary starting points for modeling the explosion phase of the primary and thus for assessing the performance and safety of stockpiled primaries.

In the interest of expanding our hydrotest capabilities to include experimental validation of calculated nuclear performance, the Advanced Hydrotest Facility (AHF) has been proposed (Fig. 1). The AHF will provide improved understanding of three-dimensional (3-D) effects associated with aging and weapons features, as well as time-dependent, high-resolution measurements of pit density and gas-cavity configurations. The AHF will require an advanced radiographic capability that provides accurate information about densities and material positions, from which we can infer the degree of supercriticality, the shape of the boost cavity, and the mix that would be present in an actual imploding primary. Allowed manufacturing tolerances can cause an implosion to be 3-D (deviating from two-dimensional symmetry) even in normal operation, and accidental detonations are almost always 3-D. As a result, radiographs are needed from a number of directions (at least four and preferably 12) so that material densities can be reconstructed with accuracies sufficient to derive nuclear parameters. Also, since the implosion progresses with time, a temporal series of radiographs (5–10) is needed over a time period relevant to the processes being recorded. This time window may need to cover a period as long as the full implosion.

Currently, two radiography options are being considered for the AHF, one using multi-GeV protons and one using multi-MeV x-rays. Ultimately, the results for both options will be compared to determine an optimal technology mix for the AHF. Because an actual hydrotest at 50 GeV was not feasible at existing high-energy

accelerator facilities, the Tri-Laboratory External Advisory Committee for Advanced Hydrotesting Research, which oversees AHF development, deemed that a combination of dynamic experiments at the Los Alamos Neutron Science Center (LANSCE) using 800-MeV protons and a suitable static demonstration at 25 GeV at Brookhaven National Laboratory's Alternating-Gradient Synchrotron (AGS) would provide enough data to evaluate proton radiography as a viable candidate for the AHF.

In collaboration with scientists, engineers, and technicians from Lawrence Livermore National Laboratory, Lawrence Berkeley National Laboratory, Brookhaven National Laboratory, Indiana University, and Bechtel Nevada, we have been collecting the data necessary to make that assessment. This research highlight provides an overview of proton radiography and a summary of the work that has been (or will be) done at LANSCE and the AGS.

Overview of Proton Radiography

Hydrodynamic radiography refers to a technology used to view inside thick material objects (specifically the primaries of nuclear weapon assemblies) as they are undergoing implosion and compression because of the detonation of surrounding high

*Fig. 1 Artist's concept of the proposed 12-axis AHF.*

explosives. The principal tool of hydrotesting is thick-object-penetrating radiography. The images obtained must be formed very quickly (in ~50 ns or less) to freeze the motion of the moving components and features and to avoid motion blur. The images are negatives, in that the information depicting the primary assembly's internal structure is obtained from the attenuation of the penetrating radiation.

Such radiographs were traditionally created using x-rays, but recent experiments have demonstrated that proton radiography is a more robust solution. In proton radiography, a high-energy beam of protons impinges directly on the object to be radiographed. Unlike x-rays, protons undergo a large number of very forward-angle scatterings as they pass through the object and the exit window of the containment vessel. This introduces a blur to the image that is then removed, for the most part, by a magnetic lens system between the object and the detectors. The residual blurring can be further reduced by increasing the energy of the proton beam. For typical weapon-primary assemblies and containment-window thicknesses, submillimeter resolutions can be obtained with proton beam energies near 50 GeV, which can be produced in conventional accelerator architectures.

Protons have a number of advantages over x-rays in producing radiographic images. Protons have long, mean-free paths that are well matched for imaging thick, dense objects, and the proton results are sensitive to both material density and composition. The final images produced with protons also have a significantly higher

Fig. 2 Proton radiographic facilities on Lines B and C at LANSCE.
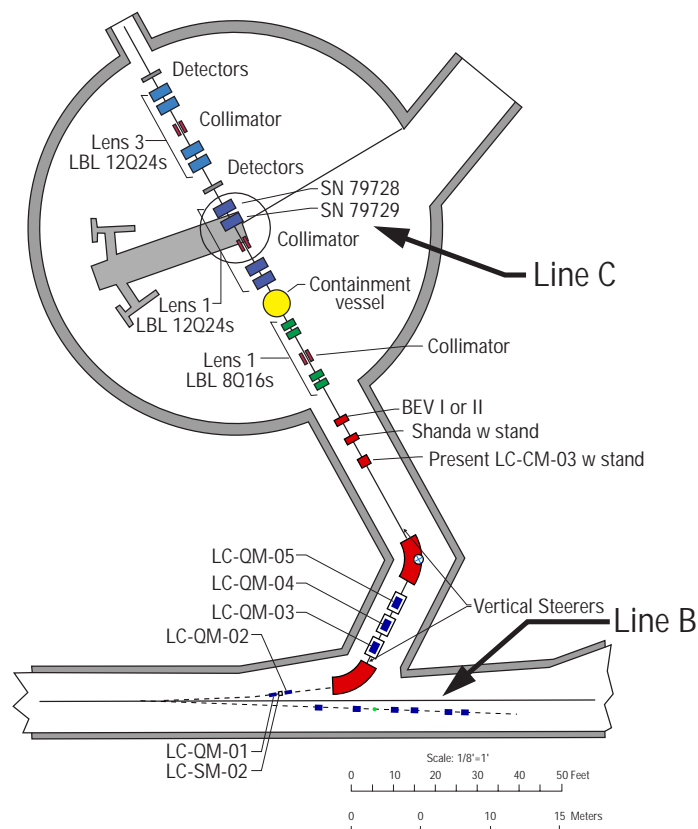
signal-to-noise ratio than x-ray images. In addition, protons provide a high detection efficiency that can generate many frames and simultaneous view directions of the explosion, producing a kind of "motion picture." Proton radiography is also easier to execute. There is no need for a bremsstrahlung converter (which is needed to produce x-rays by converting high-intensity electron beams) because the proton beam directly illuminates the object. Furthermore, proton accelerator technology already exists to provide the required beam energies, intensities, and time structures, making this technique a viable alternative for immediate application.

Proton Radiography at LANSCE

Our experiments at LANSCE addressed specific problems involving detonation-wave propagation inside a high-explosive assembly as a function of temperature and other high-explosive properties. LANSCE is capable of providing 800-MeV protons, which are well-suited for examining shock-wave propagation in small-scale, high-explosive systems. This lower energy limits the sample candidates to relatively thin, low-Z systems. These limitations arise primarily from multiple scattering and energy loss within the object and aberrations in the lens system—effects that become less important as the beam energy increases.

In preparation for our experiments, we installed new beam line diagnostics, a containment vessel, and a lens system in LANSCE's Line B area. Figure 2 shows a schematic of the Line B area used for the FY97 shots. Figure 2 also shows a schematic of a facility upgrade recently commissioned in Line C. The new Line C facility has a three-lens system, permitting beam, density, and material identification measurements. It is also capable of handling larger explosive charges because it can accommodate a larger containment vessel.

We conducted 25 dynamic shots on Line B from April to August 1997 to investigate the characteristics of shock propagation in different lots of high explosives over a range of temperatures. Typically, four to six frames were taken of each explosion. Figure 3 shows a detonation wave at four different times in a high-explosive assembly. The detonation wave is clearly evident in the radiographs as it propagates from the detonator to the outer surface of the explosive materials. The images were recorded on a phosphor image plate that allows one image per shot. An active camera system has now been installed and used to capture up to 12 frames in the time of a single high-explosive detonation. Future detector development is expected to provide the ability to take thousands of frames during the explosion to produce a more detailed motion picture of the event.

Many modern nuclear weapons incorporate insensitive high explosives (IHEs) to greatly reduce the chance of an accidental detonation during transportation or handling. Because of the reduced sensitivity of the IHE, its initiation and detonation is much more difficult to accurately model in computer codes, making
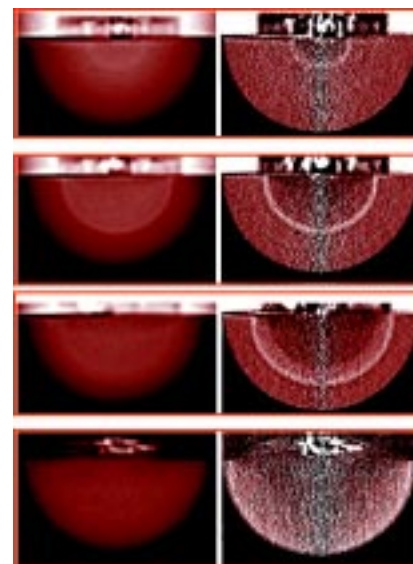
Fig. 3 Analysis results from proton radiographs of the detonation wave in a high-explosive assembly at four different times. Areal densities (left) and reconstructed volume densities (right), extracted under the assumption of axial symmetry, are shown.

reliable weapons detonation more difficult to guarantee under a wide range of conditions. The LANSCE proton radiographs provided an extensive set of data for IHE detonation for various initial conditions and temperatures. Such data show that our present calculational models have shortcomings and will help us develop and validate better models. This better understanding will help us maintain our confidence in these weapons into the future.

The dynamic experimental program at LANSCE has been an unqualified success, demonstrating our ability to perform dynamic experiments at high resolution, incorporate a containment system, eliminate blur with magnetic lenses, extract material composition using multiple lens techniques, and utilize the multiple pulse capability of the accelerator with a multiframing detection system. Upcoming experiments will include extensions of the IHE studies and high-explosives experiments in collaboration with the Atomic Weapons Establishment, Livermore, and Sandia National Laboratory.

High-Energy Proton Radiography at the AGS

In addition to our work at LANSCE, we are preparing to conduct static demonstrations using high-energy protons (up to 25 GeV) at Brookhaven's AGS. This is a major milestone because it demonstrates performance at parameters near those proposed for the AHF.

In preparation for the 25-GeV experiments, we collected data using a secondary beam from the AGS that provided only 7–10 GeV protons at low intensity. The lower intensity prevented us from performing true flash radiography, but the resulting data were able to demonstrate the low background level at the detector, confirm calculations of system performance, and prove the utility of the magnetic lens system at high energies.

To achieve a true flash radiograph of a static object, we have begun construction of a new beam line at the AGS to deliver the full energy of the accelerator (25 GeV) at full AHF intensities (10^{11} protons per pulse). We are installing two sets of lenses to allow for determination of material composition as well. The goal of the experiment is to demonstrate a few percent density measurement on a 1-mm^2 pixel size for thick objects (several hundred grams/cm^3) in the presence of a containment system. A suite of classified and unclassified static objects will be radiographed as part of this program. In addition, we will characterize the experimental backgrounds seen by the detection system. Other information on tomographic reconstruction, detector performance, and novel lens concepts will be gathered if time permits. We expect to complete the new AGS beam line and conduct a two week run in August 1999. The need for further runs will be evaluated based on the results of the August run.

Plans for a Proton Radiography Interim-Step Machine

We are currently assessing the feasibility of building a machine dedicated to testing proton radiography that would serve as an

intermediate step to the AHF. Researchers from Los Alamos and Livermore have developed a concept for constructing a one- to two-axis, high-energy (25–50 GeV) ring using existing magnets from a decommissioned accelerator at Fermi National Laboratory. This proton radiography interim-step machine (PRISM) is estimated to cost approximately 10–20% of the proposed AHF and would provide a valuable testing ground to perform contained hydrotests with protons. Although limited by a minimal number of viewing axes (upgradable in the future), it would be capable of achieving full AHF resolutions, have the ability to perform material identification through a multiple lens system, and deliver the stored pulses (~20) over a long time-window using an extraction kicker system. This would provide both a technology development capability, as well as a unique tool for providing data to the SBSS program. PRISM could be constructed at either the Nevada Test Site or at Los Alamos. Advantages of a Los Alamos siting include use of LANSCE as an injector to the main ring to reduce cost, extensive accelerator infrastructure and expertise, and the existence of a vigorous hydrotesting program. Nevada Test Site offers an existing firing site. We are currently working with Livermore to evaluate these options, and we will submit a preconceptual design report within the year. An artist's concept of PRISM is shown in Fig. 4. PRISM would be a first step toward the AHF, and would include the linac (or comparable) injector, the main 50-GeV acceleration ring, a one- to two-axis extracted beam line, a firing point, and a lens/detector system.

Fig. 4   Artist's concept of PRISM.

Looking for Antiquarks in Nuclei

J. M. Moss (P-25);
D. M. Alde, H. W. Baer,
T. A. Carey, A. Klein, C. Lee,
M. J. Leitch, J. W. Lillberg,
P. L. McGaughey, C. S. Mishra,
and J.-C. Peng (Los Alamos
National Laboratory);
C. N. Brown, W. E. Cooper, and
Y. B. Hsiung (Fermilab);
M. R. Adams (University of Illinois,
Chicago);
R. Guo and D. M. Kaplan
(Northern Illinois University);
R. L. McCarthy (SUNY Stony
Brook);
G. Danner and M. J. Wang (Case
Western Reserve University); and
M. L. Barlett and G. W. Hoffmann
(University of Texas)

Introduction

Recent experiments carried out at Fermi National Accelerator Laboratory's 800-GeV proton synchrotron have stirred the nuclear physics community in recent years by revealing unexpected phenomena in the realm of antiquark behavior. Through these experiments, our team has taken a pioneering step into a new field that combines objectives of interest to nuclear physicists with the techniques and framework of high-energy physics.

This paper describes the work that lead to this experimental effort, and it highlights the main results from Experiment 772 (E772), which began our search for antiquarks. This experiment was the beginning of a very successful collaboration that lead the same core personnel to participate in two additional experiments. The success of this collaboration is evidenced in the impact of the data on the nuclear physics community. In 1998, this work was awarded the prestigious Tom W. Bonner Prize, which recognizes outstanding experimental research in nuclear physics.

Nuclear Physics and Quarks

We all know that the aspects of nuclear physics that touch most people's lives—bombs and nuclear reactors—were invented in the 1940s and 1950s long before anyone knew about quarks and gluons. Similarly, the nuclear physics known prior to the first quark model (1964) was sufficient to understand the mechanisms for energy generation in the sun and stars. Through the development of a combination of phenomenological models, including the Nobel-Prize winning nuclear shell model, the beautiful and varied properties of nuclei could be understood at a quantitative level—all before quarks were sparkles in the eyes of their theoretical creators, Murray Gell-Mann and George Zweig, and long before the experimental discovery of quarks in 1970.

In spite of the successes of quarkless nuclear physics, in the late 1970s and early 1980s quarks, gluons, and the underlying theory of their interactions, known as quantum chromodynamics (QCD), had become so well established in particle physics that nuclear physicists were asking, "What's in it for us?"

Nucleons Under the Microscope

The mystery of quarks is still that one doesn't "see" them one at a time. They always come in threes, or baryons, of which protons and neutrons are the best known examples, or in pairs of quarks and antiquarks, or mesons, the particles whose exchange between neutrons and protons binds them into nuclei. Collectively baryons and mesons are known as hadrons. An excellent expression of this dichotomy is found in the words of the famous Russian theorist Y. L. Dokshitzer, "Quarks and gluons are the truth, but hadrons are the reality." Figure 1 illustrates the "reality" of the proton in low and high resolution pictures.
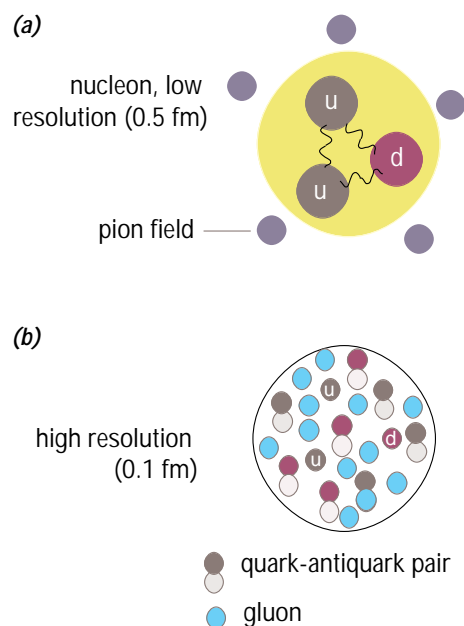
Looking for Quarks Inside Nuclei

In the early 1980s physicists were looking for an experiment that would definitively demonstrate that nuclei were more than systems of neutrons and protons bound by meson exchange— nuclei, too, would exhibit effects explainable only in terms of the truly elementary particles, quarks. The dilemma was concisely stated in an unpublished talk at the International Nuclear Physics Conference in Florence, Italy in 1983. "They [quarks] are like the Mafia in Sicily. They may be hard to spot, but you just know that they are there somewhere."

The answer to this dilemma arrived in 1983 with the publication of the now famous European Muon Collaboration (EMC) effect[1]. The EMC used 200-GeV muon beams at the European Laboratory for Particle Physics (formerly the *Centre Européenne pour la Recherche Nucléaire*, or CERN) Super Proton Synchrotron to carry out a higher-energy version of the same experiment that had led to the Nobel-Prize winning discovery of quarks at the Stanford Linear Accelerator Center (SLAC) electron accelerator. It takes an average of 8 MeV to remove a nucleon from a nucleus, and the CERN experiment used beams some 25,000 times greater in energy. A rough analogy might be a bowling ball running headlong into a bowling pin: Surely it doesn't matter whether or not the pin has been taped to the floor! Similarly, or so the experimenters presumed, it couldn't matter whether the CERN experiment used a hydrogen (deuterium) target, where the quarks are in free nucleons, or a more convenient target such as iron, where the quarks are bound in nuclei. Fortunately, the EMC group took data for both kinds of targets. The results were surprising. When the EMC compared the data, the ratio of scattering probabilities from iron and deuterium was very significantly different from unity. It mattered whether quarks were in free nucleons or bound in nuclei! This result electrified the nuclear and high-energy physics communities. Within two years of the EMC publication there were more that 300 theoretical papers written about how the data might be understood.

Antiquarks Inside Nuclei

The problem, of course, was that there was only one EMC effect, a relatively small data set that could be reproduced theoretically by many different mechanisms. What was needed was a different experiment. Many of the theorists working in this area hit upon the Drell-Yan (DY) process as the answer. In simplest terms, the DY process is quark-antiquark annihilation—the quark and antiquark are contained in two different hadrons which collide. This annihilation results in the production of a pair of leptons with

(a)

nucleon, low resolution (0.5 fm)

pion field

(b)

high resolution (0.1 fm)

● quark-antiquark pair
○

🔵 gluon

Fig. 1 Low (a) and high (b) resolution illustrations of the proton. The basic properties of the proton, such as electric charge, are determined by two "up" quarks of charge +2/3 and one "down" quark of charge -1/3. The pion field, which provides the longest-range part of the two-nucleon interaction, consists of pairs of quarks and antiquarks. For example, the π^+ is composed of an up quark (+2/3) and an antidown quark (+1/3).

Deep-inelastic muon scattering

(a)

Drell-Yan process

(b)
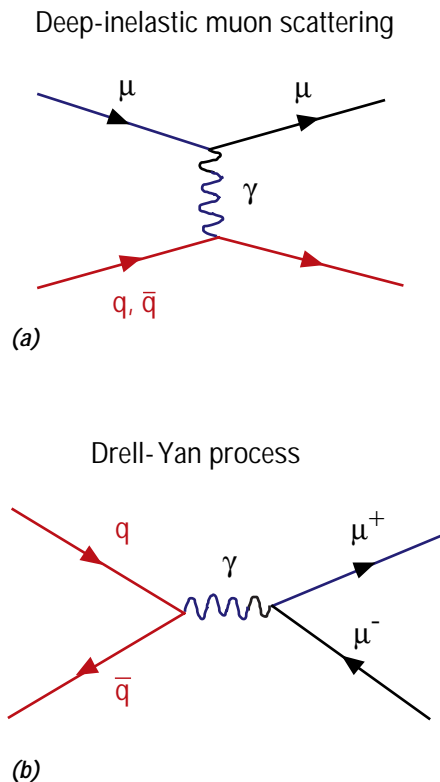
Fig. 2   Feynman graphs for two related high-energy electromagnetic processes. In (a), a high-energy muon (top left) collides with a quark or antiquark in the target. As the reaction proceeds to the right in time, the momentum of the muon scattered to the upper right is measured in a spectrometer. From the initial and final muon momenta, the energy transferred to the quark can be inferred. In the DY process, (b), a quark from one hadron annihilates with an antiquark from a second hadron, producing a virtual photon which subsequently decays into a pair of muons. Here, by energy conservation, a measurement of the final muon momenta is sufficient to reconstruct the original colliding quark and antiquark momenta.

very large mass. The Los Alamos Subatomic Physics Group (P-25) was introduced to this process in the early 1980s in a seminar given by theorist Gerry Miller of the University of Washington.

Figure 2 shows the relation between deeply inelastic lepton scattering (DIS), the original quark-discovery reaction, and its close cousin, the DY process. The DY process was "discovered" theoretically in 1970, near the time of the first DIS experiments at SLAC. It was verified experimentally at Fermilab and CERN in the late 1970s only after the experimental techniques were developed for measuring this process, which has a very small cross section in the presence of huge backgrounds.

Our contributions began around 1985–86. We discovered that a measurement of the nuclear dependence of the DY process at the level of precision of the EMC effect had never been made. We also discovered that the theoretical issues connected with a quantitative understanding the DY process had largely been resolved in the early 1980s. Thus, it was time for a new experiment. But not just any DY experiment would do. The experimental conditions had to be arranged for maximum sensitivity to antiquarks in the target. In brief, this required a beam of high-energy protons—not pions or antiprotons—and a spectrometer to detect the highest-energy, most forward-going dimuons. Fortunately, these conditions could be met using an existing spectrometer and beamline at Fermilab. In 1986 a bare-bones group consisting of Jen-Chieh Peng, Gerry Garvey, and Joel Moss from Los Alamos National Laboratory and Chuck Brown and Bob McCarthy from a previous Fermilab collaboration concocted a proposal, which eventually became the now famous E772. Its title was, "Study of the nuclear antiquark sea via proton-induced dimuon production." These collaborators managed to rebuild, reconfigure, and successfully operate the relic Fermilab spectrometer to accomplish the required precision measurement—a significant achievement that, from proposal to publication, took only three years.

Where are the Nuclear Pions?

The E772 collaboration made a precision comparison of DY muon-pair production on targets of deuterium, carbon, calcium, iron, and tungsten. The surprising result was that there is almost no difference in the antiquark density in the heaviest targets compared to deuterium, quite unlike what was found for quarks in the EMC experiment. From almost any conventional view of nuclei, in which nucleons are bound by the exchanges of mesons, this is an enigma. After all, in quark-model terms, mesons are quark-antiquark states. So what happens to the antiquarks in nuclei? There are many ways to quantify this dilemma. Suffice it to say here that conventional meson exchange naturally leads to excesses of antiquarks in heavy targets in the range of 5–20%. The E772 data, on the other hand, are inconsistent with more than 2–4% enhancement.

Publication of the E772 results lead to considerable theoretical hand wringing. In 1993, George Bertsch, Leonid Frankfurt, and Mark Strikman addressed the issue in an article entitled "Where are the Nuclear Pions?" To illustrate the level of debate, a few months later the eminent nuclear theorist Gerry Brown and his collaborators published a rebuttal of sorts, entitled provocatively, "Where the Nuclear Pions Are!" Their explanation, based on a scale change associated with partial restoration of chiral symmetry, has not gained a large following. It is fair to say that much of the nuclear physics community is still mystified over the E772 data.

The Pion Field of the Proton

The newest contribution to our understanding of the E772 data has occurred only recently as a result of experiments performed in the 1990s. The most significant of these experiments was Fermilab E866, an effort lead by P-25 scientists Gerry Garvey, Pat McGaughey, and Mike Leitch in collaboration with scientists from other Los Alamos National Laboratory groups, Abilene Christian University, Argonne National Laboratory, Fermilab, Georgia State University, the Illinois Institute of Technology, Louisiana State University, New Mexico State University, Oak Ridge National Laboratory, Texas A&M, and Valparaiso University. The major results from this experiment were discussed in detail in a previous research highlight.[2]

In summary, the E866 collaboration employed the same reaction as performed eight years earlier by E772, the venerable DY process. This time, the goal was to find a telltale signature of the proton's pion field. In simplest terms, that signature is the presence of an excess of antidown quark caused by the virtual emission of a pion in the process $p \rightarrow n + \pi^+$. The DY process easily picks out the extra antidown quark. The experiment was carried out by making a precision comparison of DY production from both proton and neutron targets. Of course neutrons are not stable, so one uses the best substitute, deuterium, which contains a neutron and a proton. The experiment made use of two 20-cm-long liquid targets containing hydrogen and deuterium, and a significantly upgraded version of the E772 spectrometer.

The result of the E866 measurement (consistent with two previous but less precise experiments) is that the excess of antidown quarks with respect to antiup quarks in the proton is very nicely accounted for by the proton's pion field. This is an important milestone in the study of the quark structure of nucleons as it is the most compelling evidence to date of a strong link between the low resolution (meson-nucleon) and high resolution (quark) pictures of the nucleus (Fig. 1).

Where Do We Go from Here?

Since the characteristic signature of the pion field has been so clearly seen at the quark level, the lack of excess antiquarks in nuclei seems even more perplexing. Where do we go from here? The standard answer for an experimentalist is, of course, "more experiments." In fact, an experiment is already being prepared at Thomas Jefferson National Laboratory. There, experimenters will try to detect the pions responsible for nuclear binding by knocking them out of light nuclei using 4-GeV electrons. Will the pions be there in the substantial numbers indicated by the very sophisticated nuclear models developed in recent years? The nuclear physics community will surely speculate, but only time—and experimental data—will tell.

References

[1] J. J. Aubert, G. Bassompierre, S. K. H. Beck, C. Best, E. Bohm, X. Debouard, F. W. Brasse, C. Broll, S. Brown, J. Carr, R. W. Clifft, J. H. Cobb, G. Coignet, F. Combley, G. R. Court, G. Dagostini, W. D. Dau, J. K. Davies, Y. DeClais, R. W. Dobinson, U. Dosselli, J. Drees, A. W. Edwards, M. Edwards, J. Favier, M. I. Ferrero, W. Flauger, E. Gabathuler, R. Gamet, J. Gayler, V. Gerhardt, C. Gossling, J. Haas, K. Hamacher, P. L. Hayman, M. Henckes, V. Korbel, U. Landgraf, M. Leenen, M. Maire, H. Minssieux, W. Mohr, H. E. Montgomery, K. Moser, R. P. Mount, P. R. Norton, J. McNicholas, A. M. Osborne, P. Payre, C. Peroni, H. Pessard, U. Pietrzyk, K. Rith, M. Schneegans, T. Sloan, H. E. Stier, W. Stockhausen, J. M. Thenard, J. C. Thompson, L. Urban, M. Villers, H. Wahlen, M. Whalley, D. Williams, W. S. C. Williams, J. Williamson, and S. J. Wimpenny, "The Ratio of the Nucleon Structure Functions F2N for Iron and Deuterium," *Physics Letters B* 123, 275 (1983).

[2] M. J. Leitch, M. Brooks, T. Carey, G. Garvey, D. Lee, P. McGaughey, J. Moss, B. Park, J.-C Peng, P. Reimer, W. Sondheim, N. Thompson, D. Isenhower, M. Sadler, R. Towell, D. Geesaman, S. Kaufman, M. Makins, B. Zeidman, C. Brown, B. Cooper, G. Petit, X. He, B. Lee, D. Kaplan, P. Kirk, Y. Wang, Z. Wang, M. Beddo, T. Chang, G. Kyle, V. Papavassiliou, J. Webb, T. Awes, P. Stankus, G. Young, C. Gagliardi, B. Tribble, E. Hawker, D. Koetke, and P. Nord, "NUSEA—Measurement of the Asymmetry in the Light-Antiquark Nucleonic Sea," *Physics Division Progress Report, January 1, 1995–December 31, 1996*, Los Alamos National Laboratory Report LA-13355-PR (1997), pp. 96–99.